2018

Bottom and charm separation through semileptonic decays in p+p collisions at 200 GeV at RHIC

Timothy Rinn
Iowa State University

Bottom and charm separation through semileptonic decays in p+p collisions at 200 GeV at RHIC

by

Timothy Rinn

A dissertation submitted to the graduate faculty

in partial fulfillment of the requirements for the degree of

DOCTOR OF PHILOSOPHY

Major: Nuclear Physics

Program of Study Committee:
Marzia Rosati, Major Professor
Kris De Brabanter
John Lajoie
Soeren Prell
Kirill Tuchin

The student author, whose presentation of the scholarship herein was approved by the program of study committee, is solely responsible for the content of this dissertation. The Graduate College will ensure this dissertation is globally accessible and will not permit alterations after a degree is conferred.

Iowa State University

Ames, Iowa

2018

ABSTRACT

Details of the measurement of the production of open heavy flavor hadrons with bottom and charm quark content in p + p collisions at $\sqrt{s}$ = 200 GeV are presented. The measurement proceeds through the use of a distanced of closest approach analysis of electron tracks from the semileptonic decay of bottom and charm hadrons using the PHENIX detector. The relative contribution of electrons from bottom decays to inclusive heavy flavor electron production is found to be consistent with perturbative QCD calculations at fixed-order-plus-next-to-leading-log within experimental and theoretical uncertainties over the transverse momentum range of 1 GeV/c to 9 GeV/c.

TABLE OF CONTENTS

ABSTRACT ii

LIST OF TABLES vi

LIST OF FIGURES vii

CHAPTER 1. INTRODUCTION 1

CHAPTER 2. STUDYING THE BUILDING BLOCKS OF MATTER 4

2.1 Historical Perspective 4

2.2 Standard Model 6

2.3 The Strong Force 9

2.4 QCD at Short Distances 11

2.4.1 Fixed Order Next to Leading Log 13

2.5 QCD at Long Distances 14

2.6 Studying the Quark Gluon Plasma 16

2.6.1 Relativistic Ion Collisions 16

2.6.2 Heavy Flavor as a Probe of the Quark Gluon Plasma 18

CHAPTER 3. THE EXPERIMENT 20
3.1 The Relativistic Heavy Ion Collider 20
3.2 The PHENIX Detector 22
3.2.1 Central Arms 23
3.3 Data Acquisition/Triggering 30
3.3.1 Minimum Bias Trigger 31
3.3.2 ERT Trigger 31
3.4 Monte Carlo 33
3.4.1 PYTHIA 33
3.4.2 PHParticleGen 33
3.4.3 Event Description 34

CHAPTER 4. HEAVY FLAVOR SEPARATION ANALYSIS OVERVIEW 36
4.1 Measuring Electrons in PHENIX 36
4.2 Distance of Closest Approach 37
4.3 Unfolding Procedure 39
4.3.1 Bayesian Unfolding 39
4.3.2 Parameter Space 40
4.3.3 Evaluating Likelihood 41
4.3.4 Decay Model 42
4.3.5 Prior and Regularization 44

CHAPTER 5. 2015 p+p ANALYSIS 46
5.1 Reference Vertex 46
5.2 Run QA 49
5.2.1 Parameters for Quality Assurance 49
5.2.2 Run-By-Run Quality Assurance 51

5.3 Analysis Cuts . . . 55
5.3.1 List of Electron Identification Cuts . . . 55
5.3.2 List of Track Selection Cuts . . . 56
5.4 dca_T Resolution . . . 63
5.5 Understanding Background Contributions . . . 66
5.5.1 Hadron Contamination . . . 67
5.5.2 Electron Background . . . 72
5.5.3 dca_T Templates . . . 84
5.5.4 Normalized dca_T Templates . . . 86
5.6 Inclusive Heavy Flavor Differential Cross-section . . . 88
5.7 Unfolding Measurement . . . 89
5.7.1 Regularization Parameter . . . 90
5.7.2 Evaluating the Unfolding . . . 90
5.7.3 Unfolding results . . . 94
5.8 Systematic Uncertainties . . . 97
5.8.1 Background Normalization Uncertainty . . . 98
5.8.2 Systematic Uncertainty From Regularization . . . 100
5.8.3 Total Uncertainty . . . 101

CHAPTER 6. RESULTS AND DISCUSSION . . . 104
6.1 Hadron Yields . . . 104
6.2 b-fraction . . . 106
6.3 Conclusions and Outlook . . . 110

REFERENCES 110

LIST OF TABLES

Table 5.1 Cuts defining the variables used for quality assurance and run selection. *Note: n0 refers to the number of photo-tubes fired in the RICH.* 51

Table 5.2 Simulated decay modes for each primary particle species in the electron cocktail. Branching Ratios (B.R.) extracted from PYTHIA decay table 77

LIST OF FIGURES

Figure 1.1 The Nuclear Modification Factor R_{AA} (comparing Au+Au to p+p) is shown as a function of transverse momentum of the decay electrons. A suppression ($R_{AA} < 1$) of heavy flavor quarks is observed in Au+Au relative to p+p for p_T above 2 GeV/c. Adare et al. (2011b) 2

Figure 2.1 Figure of the standard blocks of matter within the framework of the standard model. This consists of 6 quarks, 6 leptons and 4 force carriers. cer () 6

Figure 2.2 A Feynman diagram of the base interaction of QED, showing the interaction between a photon, a particle and its antiparticle 7

Figure 2.3 A sample of the semileptonic decay of a charm quark to a strange quark through the release of an electron and anti electron neutrino. 8

Figure 2.4 Shown are Feynman diagrams for the color based interactions of QCD. This describes both interactions between quarks and gluons, as well as gluon gluon interactions. 9

Figure 2.5 A collection of measurements of the QCD coupling constant α_s as a function of Q. Patrignani et al. (2016) 11

Figure 2.6 A schematic of a hadron-hadron collision production a heavy flavor quark of momentum k. Nason et al. (1989) 12

Figure 2.7 Feynman diagrams corresponding to the 5 interactions which contribute to leading order heavy flavor production. Nason et al. (1989) 13

Figure 2.8 Shown are the QCD energy densities over temperature to the fourth, representing the entropy, calculated using lattice QCD, the arrows on the top right represent the Stefan-Boltzman limit which is also understood as the non-interacting limit Karsch (2002) 15

Figure 2.9 Shown is a cartoon of the evolution of a hard scattering heavy ion collision at RHIC highlighting a few specific stages. 16

Figure 3.1 Shown is a schematic drawing of the Relativistic Heavy Ion Collider complex 21

Figure 3.2 Shown is a schematic drawing of the PHENIX detector as of 2015. 22

Figure 3.3 A drawing of the VTX detector, from the perspective of the beam pipe (z-direction), the different colors corresponding to the different "layers" B0 through B3. 25

Figure 3.4 Schematic Drawings of the PHENIX drift chambers, panel (b) shows a schematic of the wire planes within the drift chamber. Adcox et al. (2003a) 26

Figure 3.5 Shown is a schematic of one of the lead scintillator modules (left) and lead glass (right) taken from Aphecetche et al. (2003) 28

Figure 3.6 Shown is the ERT efficiency as a function of transverse momentum for the run15 p+p data set. One can see the turn on points for the various triggers. 32

Figure 3.7 Shown are comparisons of the ϕ distributions of clusters between two particle generators and data for each VTX layer. The gap between 1 and 2 radians is due to the incomplete azimuthal coverage of the VTX 35

Figure 4.1 Shown is how parameters L and R are determined as used in the calculation of the dca_T according to equation 4.1 38

Figure 4.2 Shown is the truth dca_T of bottom and charm electrons as determined using PYTHIA p+p at $\sqrt{s} = 200$ simulations. 39

Figure 4.3 From the decay matrix shown are the probabilities of a charm hadron of a given p_T to decay to an electron of given p_T (a) and for a sample electron p_T bin the dca_T (b) 43

Figure 4.4 Second-order finite-difference matrix used in the calculation of the likelihood due to the regularization, which acts as a penalty on large deviations in the 2nd derivative. 44

Figure 5.1 When all tracks come from the primary vertex (a) the VTX can reconstruct the correct vertex. When there is a track from a displaced vertex in a p+p event (b) it can bias the reconstructed vertex. . . . 47

Figure 5.2 Shown on the left is the vertex resolution as a function of the number of good vertex tracks. Shown on the right are the dca_T resolutions for hadrons in heavy flavor events both without the recalibrator (precise) and with the recalibrator (weighted average) applied 48

Figure 5.3 Shown are the mean number of VTX stand alone tracks as a function of run number (left) and a sample VTX cluster distribution from a run identified as bad due to this check (right). 52

Figure 5.4 Shown are the mean number of VTX clusters in each layer as a function of run number, excluding runs where the number of clusters in a layer are 0 53

Figure 5.5 Shown are the mean number of PHCentralTrack electrons as a function of run number (Left) and a sample PHCentralTrack distribution from a run identified as bad due to this check (right). 54

Figure 5.6 Shown dca resolution [cm] of hadrons in data as a function of run for runs not flagged by other QA checks 55

Figure 5.7 Distribution of prob (probability of EM-calorimeter shower being electromagnetic), for tracks which pass all other analysis and EID cuts 58

Figure 5.8 Distribution of n0, for tracks which pass all other analysis and EID cuts, with an additional $n0 > 0$ requirement to exclude the dominant hadron peak 59

Figure 5.9 Distribution of normalized E/p (dep), for tracks which pass all other analysis and EID cuts 60

Figure 5.10 Distribution of chisq/ndf, for tracks which pass all other analysis and EID cuts 61

Figure 5.11 Distribution of the number of VTX layers with hits, for tracks which pass all other analysis and EID cuts 62

Figure 5.12 dca_T distribution of hadrons for run 423844 fit with a Gaussian for $1 < p_T < 1.5$ GeV/c, on the right panel the ratio of the fit to the data was taken, and good representation consistent with the hadron dca_T being well described by a single Gaussian in the peak region is observed. 64

Figure 5.13 dca_{T_σ} extracted from hadrons in data as a function of p_T for the entire data taking run 65

Figure 5.14 dca_{T_σ} measured run by run, for tracks with $p_T > 1.5GeV$, observe a Gaussian distribution 66

Figure 5.15 Fits to the hadron `dep` distribution to construct a template for the shape of the hadron contamination used to fit the electron candidate *dep* distribution. 68

Figure 5.16 Distribution of the `dep` variable for electron candidate tracks in various p_T selections fit by a Gaussian + hadron template. 69

Figure 5.17 The survival rates of the n0 cut for both single electron simulations, and hadrons in data 70

Figure 5.18 The ratio of electrons with $n0 > 3$ to $n0 > 1$ was compared between data and simulations. In data electrons were identified using a $|dep| < 1$ cut 71

Figure 5.19 Hadron contamination extracted using two independent methods. The nominal hadron contamination is the weighted average of the two results shown in the left panel. 72

Figure 5.20 The isolation cut window size in $charge \times \Delta\phi$ as a function of p_T for each layer in the VTX. This shape was selected to account for the decreasing opening angles of conversion electrons as the p_T increases. 74

Figure 5.21 The survival rate of photonic electrons of the isolation cut due to correlated effects as determined using simulations 75

Figure 5.22 The survival rate of the isolation cut of hadrons in data, used to determine the effect of random association on the isolation cut. . . 76

Figure 5.23 Modified Hagedorn fit to the published pi0 cross section from Adare et al. (2007). Left is the nominal fit, and on the right are 1000 variations used to extract systematic uncertainty 78

Figure 5.24 Shown is the electron cocktail determined using the hadron weight functions applied to the electron simulations 79

Figure 5.25 F_{np} calculated using the isolation cuts over the analysis region using Equation 5.9 80

Figure 5.26 F_p calculated using the isolation cuts over the analysis region. . . . 81

Figure 5.27 The fraction of decay electrons from non-photonic sources to electrons from π^0 decays in the electron cocktail. 83

Figure 5.28 Fraction of measured electron candidates attributed to each background source, as calculated using the electron cocktail and F_{np}. . . 84

Figure 5.29 dca_T resolution comparison between data hadrons (predominately charged pions), simulated pions and simulated pions with a smearing factor to correct for the resolution difference between data and simulations. 86

Figure 5.30 dca_T distribution of electron candidates in data (black), as well as normalized templates for each source of background electrons, for each p_T bin. 88

Figure 5.31 Inclusive electron differential cross-section measurement for various centralities of Au+Au (red and blue points) as well as p+p (green) which is used in the unfolding from Adare et al. (2011b). 89

Figure 5.32 Shown is the Log Likelihood as a function of the regularization parameter α, with the red dashed line representing a 1/2 drop in LL. 90

Figure 5.33 Shown is the $Ln(L)$ versus step number in the 3rd iteration of the unfolding. There are no observable long range trends, consistent with the unfolding having converged. 91

Figure 5.34 Refold of the DCA_T distribution for each p_T bin in which the unfolding uses DCA_T constraints. The various curves on the plots refer to the unfolded $c \rightarrow$e, $b \rightarrow$e, background, refold, and measured electrons. 92

Figure 5.35 Top: Refolded inclusive heavy flavor electron differential cross section compared to the previously published inclusive yield, which is one of the inputs to the unfolding procedure. Also shown are the unfolded contributions from charm and bottom decays separately. Uncertainties are purely statistical. Bottom: Ratio of the previously published inclusive yield to the re-summed unfolding output. 93

Figure 5.36 The red line represents the total LL of the unfolding result, with the yellow distribution representing a statistical sampling. 94

Figure 5.37 Diagonal elements of panel (a) contain information on the bottom and charm hadron yields, a blow up of the yield distributions can be seen in (b) and (d) which includes the 1σ unfold uncertainty. The off diagonal elements contain the correlation information between various hadron p_T bins, a sample distribution can be seen in panel (c) 95

Figure 5.38 Unfolded hadrons yields as a function of transverse momentum for separated bottom and charm hadrons integrated over all rapidity. . 96

Figure 5.39 Unfolded fraction of electrons from bottom decays to inclusive heavy flavor electrons, as a function of p_T. The uncertainties shown are statistical only from the unfolding procedure. The three gray curves represent the central, upper, and lower FONLL predictions. 97

Figure 5.40 Unfolding results for 729 variations of the background normalization factors based on systematic uncertainties. 99

Figure 5.41 The RMS of the difference between the nominal unfold b-fraction result and the variations in the background normalizations. This is taken as the 1σ uncertainty on the b-fraction result due to the background normalizations. 99

Figure 5.42 Deviation from the nominal unfolding result when individual sources are fluctuated, while preserving all others as nominal. 100

Figure 5.43 Shown are the 1σ systematic uncertainty band to the b-fraction result from background normalization, regularization, as well as the inclusive HF yield. 101

Figure 5.44 Shown are the numerical 1σ uncertainties due to each source of considered backgrounds. 102

Figure 5.45 Shown are the fractional 1 σ uncertainty contributions to the b-fraction for each source. 103

Figure 6.1 Shown are the rapidity integrated hadron differential cross-sections for p_T between 1 and 20 GeV/c 105

Figure 6.2 Shown is a comparison of the unfolded D^0 differential cross-section to that measured by the STAR experiment at mid rapidity. The ratio of a fit to the unfolded results is seen in panel b. 106

Figure 6.3 Shown is an overlay of the unfolded b-fraction result with previously published PHENIX and STAR measurements, as well as PQCD predictions from FONLL. 108

Figure 6.4 Shown is the R_{AA} calculated using the 2011 Au+Au in combination with a p+p baseline measurement from STAR, using electron-hadron correlations. Adare et al. (2016) 109

CHAPTER 1. INTRODUCTION

Nuclear matter under extreme conditions, high temperature or density, undergoes a phase transition into state of matter called the Quark Gluon Plasma (QGP) where the normal nuclear matter constituents, protons and neutrons, are deconfined into quarks and gluons.

Heavy ion collisions at the Relativistic Heavy Ion Collider (RHIC) produce matter hot enough to form the QGP, as a short lived, extremely hot and dense medium of nuclear matter which can be used to study the properties of the strong force.

One of the main goals of the PHENIX experiment at RHIC is to study the Quark Gluon Plasma and it is particularly advantageous to use heavy flavor quarks as one of the probes, charm and bottom, since they are produced early in the collision.

PHENIX measurements have indicated that heavy flavor quarks experience an energy loss while propagating through the QGP similar to light quarks Adare et al. (2011b). This effect was observed through modifications to the transverse momentum distribution in Au+Au compared to p+p by looking at the nuclear modification factor (R_{AA}) seen in Figure 1.1. It is thought that this energy loss comes from color-based interaction of the color-charged quarks within the plasma as they traverse it.

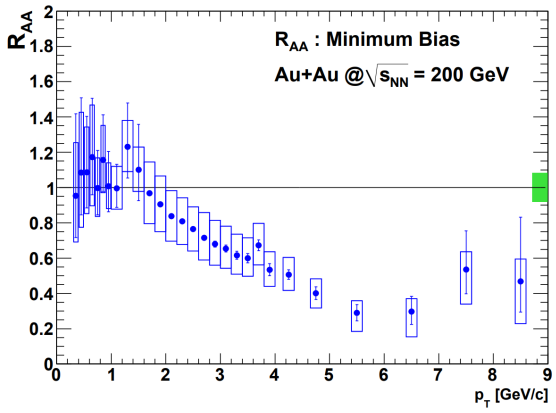

Figure 1.1: The Nuclear Modification Factor R_{AA} (comparing Au+Au to p+p) is shown as a function of transverse momentum of the decay electrons. A suppression ($R_{AA} < 1$) of heavy flavor quarks is observed in Au+Au relative to p+p for p_T above 2 GeV/c. Adare et al. (2011b)

To study the energy loss experienced by heavy flavor quarks propagating through the QGP, the electrons/positrons from semileptonic decays of charm and bottom mesons are studied using the PHENIX detector. Throughout this dissertation when I refer to *electrons* I will be referring to both electrons and positrons. While previously we couldn't distinguish between electrons from charm or bottom decays, the recent addition of the Silicon Vertex Tracker provides the capability in PHENIX to measure the production of long-lived bottom and charm quarks.

This dissertation describes the first measurement of separated charm and bottom production in p+p collisions at $\sqrt{s} = 200GeV$, using a Bayesian unfolding analysis, which takes into account both the inclusive heavy flavor electron differential cross-section and the heavy flavor electron distance of closest approach. This p+p measurement will be used as a baseline for studying the properties of the QGP (when compared to Au+Au collisions) but also to check the validity/accuracy of theoretical calculations in the framework of perturbative Quantum ChromoDynamics.

This dissertation will begin in Section 2.1 by discussing a historical perspective of the evolution of the field of nuclear physics. After which in Sections 2.2 through 2.6 it will introduce some of the theoretical background behind this measurement, including a discussion of the Quark Gluon Plasma, as well as various models which attempt to explain both production and interactions of heavy flavor quarks. A description of the PHENIX experimental setup is presented in Chapter 3. Details of the analysis technique are discussed in Chapters 4 and 5. Chapter 6 describes the extracted bottom and charm yields with a comparison to theory and previous measurements.

CHAPTER 2. STUDYING THE BUILDING BLOCKS OF MATTER

2.1 Historical Perspective

In history, across nearly all cultures and time periods, people have been pursuing the question of how we, and the world we live in, came to be. Since the late 19th century there has been an effort to develop a new way to answer this question, and that is through the study of the smallest and highest energy matter. Some might say that the field of elementary physics was really born with the discovery of electron in the late 1890's by J. J. Thomson Griffiths (2008), the first discovered building block of matter.

In the early 1900's Earnest Rutherford was able to add to the understanding of the universe through the Rutherford Scattering Experiment. Proving that the vast majority of mass (and charge density) of an atom was actually located at the center, in what later became known as the nucleus. The experiment aimed a beam of α particles at a thin gold foil and measured the angle of deflection of the outgoing α particles. The angle of deflection in combination with the width of the gold foil was inconsistent with a series of small deflections and instead indicated a single large interaction with a central mass/charge. From this, the understanding of an atom being made up of a positively charged nucleus (containing protons) with surrounding electrons was developed. Over time, through studying the mass and charge of various atoms the existence of the neutron was discovered, completing the picture for the direct building blocks of atoms.

This understanding of the nucleus as a combination of protons and neutrons left an unresolved question. Since protons have equal electric charge and repel each other, why do they stay together in the nucleus? This question was first reasonably addressed in

the mid 1930's by Yukawa Griffiths (2008) who speculated that the protons and neutrons were attracted to one another through a new force, the strong force, which counteracted the electromagnetic repulsion. He additionally postulated that this was mediated by a force carrier, the pion. The pion was later discovered experimentally through cosmic ray experiments.

Until the mid 1960's particle physics was essentially an endless pursuit of discovering new particles, from neutrinos to new mesons and baryons. Many of these were initially believed to be "elementary particles" however, this all changed in 1964 when Gell-Mann and Zweig independently theorized that mesons and baryons were in fact made up of truly elementary particles which Gell-Mann called quarks Gell-Mann (1964). These particles were expected to be easy to observe, similar to electrons, and identifiable using a Millikan oil drop style experiment, as they were light particles with a fractional charge. However, as we now know, due to confinement it is impossible to observe a quark in isolation so the existence of quarks was verified using a less direct method Griffiths (2008). Using deep inelastic scattering scientists were able to identify that the proton's charge was concentrated into 3 lumps rather than just one, proving that a proton was not a fundamental particle and providing the first strong evidence to support the quark model.

This set off the equivalent of a gold rush in High-Energy physics, with many laboratories and experiments starting up to attempt to identify and learn more about these elementary particles. Scientists have been able to detect and identify 6 different quarks of varying masses, 6 leptons and 4 force carriers, these particles and corresponding forces appear to be well defined by the prevailing model, "the standard model". In the field of High Energy Nuclear Physics (HENP) we study high energy collisions of entire nuclei with the goal of characterizing the properties of the strong force through the formation of a state of matter referred to as the Quark Gluon Plasma (QGP).

2.2 Standard Model

Currently the best understood and accepted model for describing elementary particles and their interactions is called the Standard Model (SM). The standard model describes matter by breaking elementary particles into three categories: leptons, quarks, and force carriers. As shown in Figure 2.1, there are six unique quarks, and six unique leptons, however for each of these particles there exists a corresponding antiparticle which has opposite charge doubling the number of quarks and leptons to 12 each.

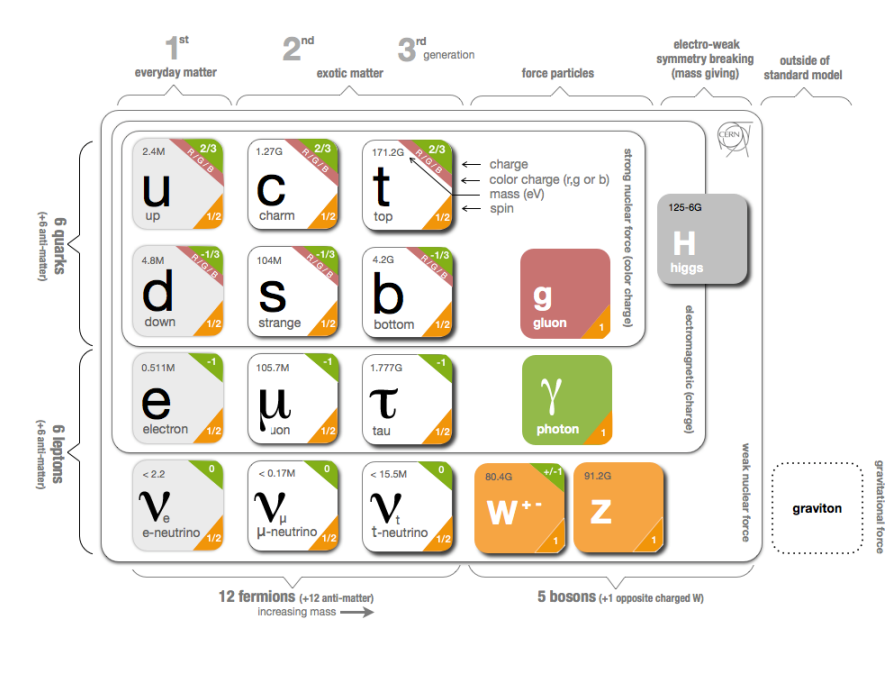

Figure 2.1: Figure of the standard blocks of matter within the framework of the standard model. This consists of 6 quarks, 6 leptons and 4 force carriers. cer ()

The standard model also describes the interactions between elementary particles through the use of the force carrier particles. Within the framework of the standard model there are 3 forces; the weak force, the electromagnetic force, and the strong force. It is important to note that in the world around us there is an additional force, Gravitation, which is

not currently described by the standard model and is much weaker than the three forces described in the standard model and the effects of which will be ignored within the context of this dissertation as it is well outside the scope.

The Electromagnetic Force is currently best described by the theory of Quantum Electrodynamics (QED), handles the interactions between charged particles using photons as the force carrier. QED is a very complex theory that can be used to describe elaborate interactions. The strength of interactions in QED depend on the fine structure constant α_{QED}, which is described by Equation 2.1. Due to the fact that α_{QED} is $\ll 1$ it is possible to use perturbative techniques around powers of α_{QED} to calculate interactions in QED. When doing these PQCD expansions all processes are broken down to the summation of individual interactions. QED consists of only one of these basic interactions; the Feynman diagram corresponding to this interaction is shown in Figure 2.2, where 'a' represent a charged particle.

$$\alpha_{QED} = \frac{e^2}{4\pi\epsilon_0\hbar c} \approx \frac{1}{137} \tag{2.1}$$

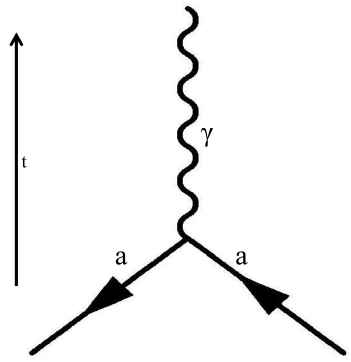

Figure 2.2: A Feynman diagram of the base interaction of QED, showing the interaction between a photon, a particle and its antiparticle

Of the forces described through the standard model the weakest force, though one of the most consequential, is known simply as the weak force. This force is mediated by the

W and Z bosons and effects both quarks and leptons. Through the weak force quarks can change flavors. This can happen naturally as part of a decay, dropping a heavy quark to a lower mass one. A sample of one of these decays is an anti-charm quark decaying into an anti-strange quark and an electron as well as an anti-electron neutrino is shown in Figure 2.3.

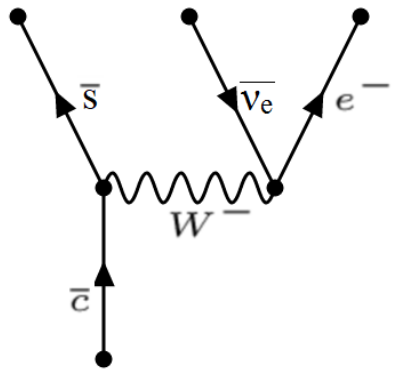

Figure 2.3: A sample of the semileptonic decay of a charm quark to a strange quark through the release of an electron and anti electron neutrino.

A very advantageous feature of the weak force, from the perspective of this dissertation, is the fact that compared to the other standard model forces it is exceptionally weak. Due to this fact, quarks and by extension hadrons which decay through the weak force have long life times and can therefore travel measurable distances before decaying. This fact is one of the main pillars of the analysis discussed later on in this dissertation, without which the technique used would not be possible. In particular bottom and charm hadrons can decay semi-leptonically through the weak force, producing an electron, as shown in Figure 2.3, which can be measured experimentally using the PHENIX detector.

2.3 The Strong Force

Of the elementary forces existing within the framework of the standard model, the Strong Force acts only on quarks and gluons with the gluon acting as the force carrier, and is well described by Quantum Chromodynamics (QCD) Fritzsch et al. (1973). Similarly to the electromagnetic force which acts on charged particles, interactions in QCD are based on the *color charge* of a particle. In QCD there are 3 *color charges*, called red, blue, and green, along with their corresponding anti-colors. The force carrier in QCD, the gluon, is color charged, with 8 color states, and responsible for the strong force field. In QCD there are 3 principle color based interactions between quarks and gluons as well as gluon and gluon interactions, the corresponding diagrams are seen in Figure 2.4.

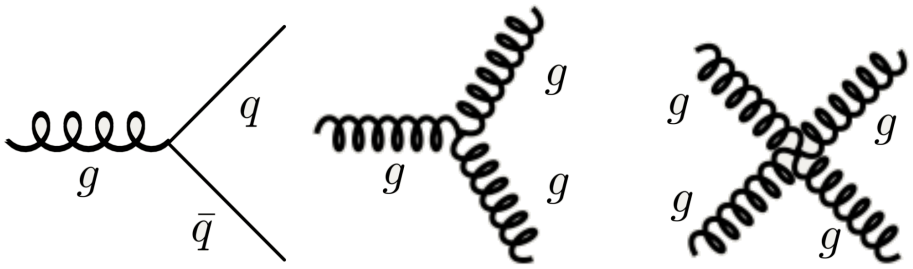

Figure 2.4: Shown are Feynman diagrams for the color based interactions of QCD. This describes both interactions between quarks and gluons, as well as gluon gluon interactions.

Interactions in QCD are described by a coupling constant α_s which is analogous to the fine structure constant α_{QED}. Due to quantum corrections the effective value of α_s depends on the distance at which the interaction is probed, or equally the momentum transfer of the interaction (Q^2) as shown in Figure 2.5. At long distances, corresponding to small momentum transfer Q^2 the parameter α_s is large. This can be understood through the idea of color anti-screening since polarization of vacuum fluctuations can result in an increasing effective color charge as the distance increases. This net anti-screening stems from a combination of screening arising from vacuum quark production, and anti-screening

from gluon self interactions which dominates. Therefore the strength of the coupling grows. An interesting phenomenon which arises from this is the property of confinement, which is responsible for the fact that quarks and gluons are not observed in isolation. As the distance between two quarks grows it can become energetically favorable for one of the exchanged gluons to generate a quark anti-quark pair which will in turn bind to the initial quarks thereby reducing the separation distance.

At close distance scales corresponding to large Q^2, the color anti-screening contribution is negligible and coupling constant becomes small. In these cases it is possible to calculate interactions using perturbation methods as is often done for QED. The explicit dependence of α_s on the momentum transfer Q^2 can be seen in Equation 2.2, one can see that in the case where Q^2 (energy scale) is significantly larger than Λ (QCD Scale) α_s becomes $\ll 1$, this is referred to asymptotic freedom.

$$\alpha_s(Q^2) \propto \frac{1}{ln(Q^2/\Lambda^2)} \tag{2.2}$$

Interactions which characteristically have a large Q^2 and therefore are able to be calculated using Perturbative QCD are often referred to as hard scattering interactions. In PHENIX heavy flavor quarks are produced primarily through hard scattering events, therefore heavy flavor production in p+p collisions production can be modeled and calculated using perturbative techniques.

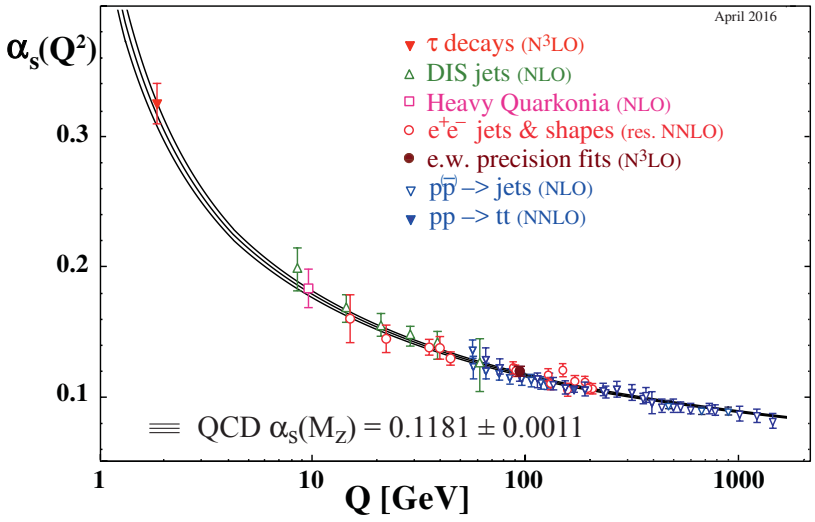

Figure 2.5: A collection of measurements of the QCD coupling constant α_s as a function of Q. Patrignani et al. (2016)

2.4 QCD at Short Distances

Since at short distances the effects of color anti-screening becomes negligible and the coupling constant α_s is small it is possible to use perturbative techniques in order calculate interactions. In high energy hard scattering collisions this allows for the calculation of the production of various quarks and/or hadrons.

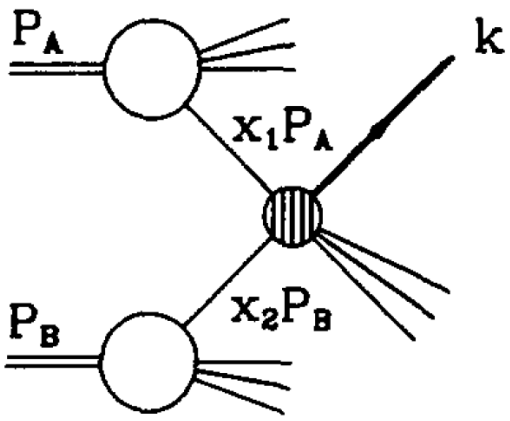

Figure 2.6: A schematic of a hadron-hadron collision production a heavy flavor quark of momentum k. Nason et al. (1989)

For heavy flavor production in hadron-hadron interactions, as visualized in Figure 2.6, the differential cross-section as a function of the momentum can be calculated using Equation 2.3: Nason et al. (1989)

$$\frac{Ed^3\sigma}{d^3k} = \sum_{i,j} \int dx_A dx_B \Big(\frac{Ed^3\hat{\sigma_{ij}}(x_A P_A, x_B P_B, k, m, \mu)}{d^3k} \Big) F_i^A(x_A, \mu) F_j^B(x_B, \mu) \tag{2.3}$$

In which F_i^A and F_i^B represent the number densities for the i^{th} parton in the incoming hadrons A and B, with incoming hadron momenta P_A and P_B respectively. The mass of the produced heavy quark is given by m while μ is the scale for ultraviolet and collinear divergences. The short distance cross-section ($\hat{\sigma}$) can be calculated using perturbative QCD.

Early QCD calculations focused on leading order contributions to $\hat{\sigma}$, in which only 5 specific interactions contributed. The diagrams corresponding to these interactions, which contribute to the order of α_s^2, can be seen in Figure 2.7. As calculations expand to higher orders in α_s the number of diagrams increase exponentially, and due to computational limitations most PQCD calculations are done using only the first few orders in α_s.

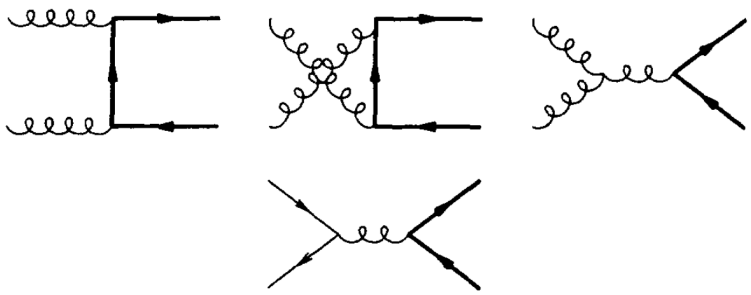

Figure 2.7: Feynman diagrams corresponding to the 5 interactions which contribute to leading order heavy flavor production. Nason et al. (1989)

2.4.1 Fixed Order Next to Leading Log

One model that is used to estimate heavy flavor production in hard scattering p+p collisions is Fixed Order Next to Leading Log (FONLL). This model combines Fixed order calculations up to order α_s^3, as well as both leading and next to leading logarithmic terms Cacciari et al. (1998). This results in a differential cross-section expression as seen in expression 2.4.

$$\frac{d\sigma}{dp_T^2} = A(m_q)\alpha_s^2 + B(m_q)\alpha_s^3 + \left(\alpha_s^2 \sum_{i=2}^{\infty} a_i \Big(\alpha_s log(\mu/m_q)\Big)^i + \alpha_s^3 \sum_{i=1}^{\infty} b_i \Big(\alpha_s log(\mu/m_q)\Big)^i\right) G(m_q, p_T) \tag{2.4}$$

Where m_q corresponds to the heavy quark mass, and $G(m_q, p_T)$ is treated as relatively arbitrary within the model due to the lack of information on power suppressed terms in the NLL contribution, and is therefore a large source of uncertainty on FONLL calculations. However one important constraint on $G(m_q, p_T)$ is that in the limit when $m_q/p_T \to 0$ the G function must approach 1 Cacciari et al. (1998). This model expands upon previously used Leading Order and Next to Leading Order calculations which contained the first two terms of equation 2.4. Through measurements of heavy flavor quark production it would be possible to provide constraints to FONLL calculations notably reducing the scale uncertainty.

This model can be used to calculate and make predictions of heavy flavor quark production in p+p collisions. It is however limited in its scope, as it does not model interactions with nuclear matter. This is due to the fact that it is a QCD calculation using perturbative techniques and interactions with nuclear mediums at RHIC are not of large enough Q^2 for perturbation theory to work.

2.5 QCD at Long Distances

In order to make calculations in the case where perturbative QCD no longer works well, a tool was developed called Lattice QCDWilson (1974) Bazavov et al. (2014). This method uses a discrete approximation to the Feynman path integrals in quantum field theory and can therefore be used to calculate QCD interactions when α_s is large where PQCD fails. This methodology is a fundamental, mathematically rigorous approach to QCD calculations, however it is strongly limited due to computational requirements. Many calculations are done in the 2, 2+1 or 3 quark flavor approximations, rather than considering all six quarks. Yet, even with these limitations it is possible for calculations to be done to understand QCD at large distances.

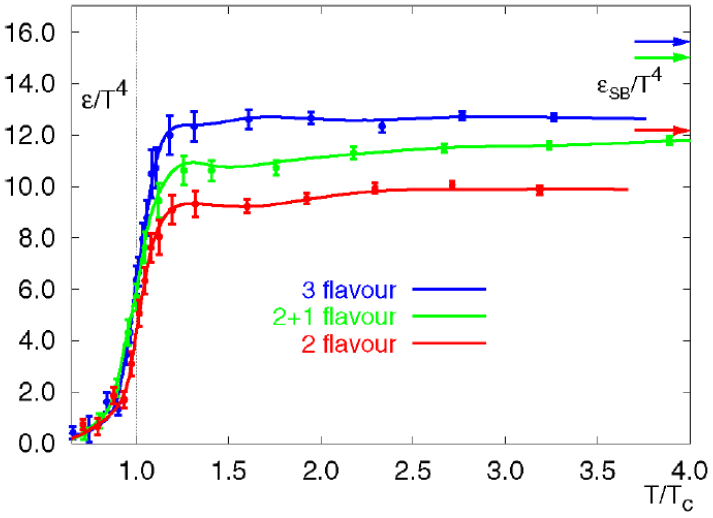

Figure 2.8: Shown are the QCD energy densities over temperature to the fourth, representing the entropy, calculated using lattice QCD, the arrows on the top right represent the Stefan-Boltzman limit which is also understood as the non-interacting limit Karsch (2002)

One prominent calculation which was done using lattice QCD is the calculation of the entropy as a function of temperature. From this calculation a particularly interesting behavior was found, and that is at a temperature of about 170 MeV (T_C) a phase transition appears. This can be seen in Figure 2.8 at the point of inflection when $T/T_c = 1$. This calculation supported the idea that if the temperature of a system gets large enough, the system deconfines. This results in a hadron gas melting into a system of quarks and gluons, which have a much larger number of degrees of freedom, therefore we observe a large increase in the entropy of the system. This state of matter is referred to as the Quark Gluon Plasma (QGP)Shuryak (1978). One interesting aspect of this calculation, which went against initial predictions is that the entropy does not actually reach the Stefan Boltzman free gas limit. This implies that the QGP is still an interacting plasma.

2.6 Studying the Quark Gluon Plasma

Understanding the interactions within the QGP allows for probing of the strong force in a statistical way averaging over many quark-quark, quark-gluon, and gluon-gluon interactions. As the QGP is produced in high energy collisions within particle accelerators and interactions with it are primarily through color charge, quarks end up being one of the best probes of interactions within the QGP. In order to understand the effects of the interactions what is typically done is a comparison between a system where no QGP is expected, namely p+p collisions, and that of a heavier system where the QGP might be created. A key metric is the modification of the transverse momentum spectrum for hadrons produced in Au+Au collisions relative to the hadron spectrum measured in p+p collisions, referred to as Nuclear Modification Factor (R_{AA}).

2.6.1 Relativistic Ion Collisions

One might naively think that QGP is produced instantaneously in heavy ion collisions, however in reality there is an evolution of phases as highlighted in Figure 2.9. The four main phases are the initial hard scattering event, the thermalization of the quarks and gluons, the QGP formation and hadronization.

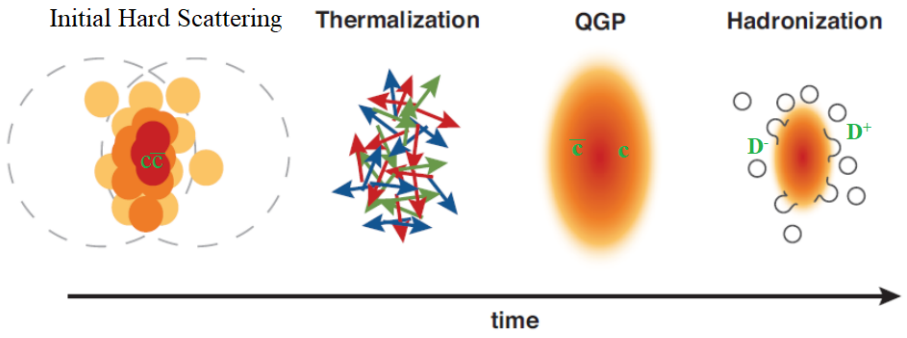

Figure 2.9: Shown is a cartoon of the evolution of a hard scattering heavy ion collision at RHIC highlighting a few specific stages.

The initial hard scattering collision is as one might expect the initial collision and hard QCD interaction between the two colliding ions. At RHIC energies in particular this stage is the only time in the evolution of the collision that heavy flavor quarks can be produced. This means that heavy flavor quarks will experience the full evolution of the nuclear medium. Due to the large Q^2 and by extension small α_s this interaction can typically be calculated using perturbative QCD.

During the initial hard scattering event it is not the entire ion that is interacting but rather an individual pair of partons. This means that the energy deposited into the system is extremely localized. The stage during which this energy becomes thermal in nature and equalizes within the nuclear matter is called Thermalization. There are predictions for how the thermalization is achieved, one of which called 'bottom-up' is based on the perturbative QCD framework Baier et al. (2001). This model works on the thought that in the initial collision high energy gluons, which are referred to as hard gluons, contain most of the collision energy. Then as the system evolves a large number of soft gluons are emitted which form a sort of thermal bath. This bath initially carries only a small portion of the total energy, however it then draws from the energy of the initial hard gluons. Thermalization is then achieved when the hard gluons have lost all of their energy and are no longer distinguishable from the thermal gluons. An alternative model for the thermalization process is based upon a hydrodynamic description, which predicts a short thermalization time of approximately 0.6 fm/c and is in good agreement with many heavy ion measurements. Additionally it contains collective processes which are not included as part of the 'bottom-up' model. Another mechanism which has been suggested, which could potentially accelerate the thermalization process is plasma instabilities Arnold et al. (2005). These instabilities would result from rapid growth of particular spatial regions, and result in collective behavior similar to what is seen within the hydrodynamic calculations.

Once thermalization is achieved it is possible, depending on the temperature, for a phase transition to occur and the QGP to be formed. As the system continues to evolve

the QGP cools down, largely due to the physical expansion of the system and due to the emission of thermal photons. Once the temperature of the system gets low enough the effects of confinement begin to come into play again. This means that quarks are no longer 'free' to move within the QGP and resort to bound colorless states, i.e. hadrons. This process of hadronization in heavy ion collisions is believed to happen through two main mechanisms, namely fragmentation and recombination Fries et al. (2003). Which describe the probabilities of a quark binding with another parton and forming a hadron.

2.6.2 Heavy Flavor as a Probe of the Quark Gluon Plasma

Although the quark gluon plasma is a short lived system which is not easy to directly observe. There are many ways to study the properties of the QGP. One of the most powerful probes, and the most relevant probe in the scope of this dissertation, of the quark gluon plasma are heavy flavor quarks. As discussed earlier, at RHIC energies these quarks are produced primarily during the initial hard scattering event rather than during thermalization. This fact has several key consequences, the first being that it is possible to use PQCD to calculate production of heavy flavor quarks, often using models like FONLL. Additionally it means that heavy flavor quarks experience the full evolution of the system and can therefore probe effects at each stage. Finally, due to the fact that the production mechanisms are the same in p+p as heavy ion systems, it is expected that the production of heavy flavor quarks in heavy ion systems (such as Au+Au) to be a direct scale of the yield in p+p correcting for the difference in the number of binary collisions. This means that any modification to the transverse momentum, p_T, dependent yield of heavy flavor quarks in heavy ion collisions compared to p+p scaled by the number of binary collisions can be attributed to interactions with the nuclear medium.

One key parameter used in this comparison is the Nuclear Modification Factor (R_{AA}) which is defined in equation 2.5.

$$R_{AA}(p_T) = \frac{dn_{AA}/dp_T}{\langle n_{coll} \rangle \, dn_{pp}/dp_T} \tag{2.5}$$

Where the dn_{AA}/dp_T and dn_{pp}/dp_T are the p_T dependent yields in heavy ion and p+p collisions respectively. The $\langle n_{coll} \rangle$ is the mean number of binary collisions expected in the heavy ion collision system, typically calculated using the Glauber Model simulating multiple-scattering of nucleons within nuclei Miller et al. (2007). When measuring the R_{AA} as a function of the p_T one gets quantitative information on the parton energy loss due to interactions with the deconfined nuclear medium. This energy loss typically manifests itself in the R_{AA} distribution by a $R_{AA} < 1$ at higher p_T and an $R_{AA} > 1$ at low p_T, as due to energy loss higher momentum particles are pushed lower in p_T.

CHAPTER 3. THE EXPERIMENT

3.1 The Relativistic Heavy Ion Collider

The Relativistic Heavy Ion Collider (RHIC)Harrison et al. (2003), located at Brookhaven National Lab, is the only heavy ion collider facility in the United States. The only other major one in the world is the Large Hadron Collider located at CERN. At RHIC there are two main experiments studying heavy ion collisions PHENIX and STAR, as well as historically two smaller experiments PHOBOS and BRAHMS.

RHIC is a remarkably versatile accelerator, able to provide both symmetric and asymmetric collisions systems of charged ions ranging from p+p all the way to Au+Au. In addition it is also able to cover a wide range in collision energies from as low as $\sqrt{s} = 7.7$ GeV up to 510 GeV. One of the most unique capabilities of RHIC, compared to every other collider currently in operation, is its ability to provide spin-polarized protons for collision systems. This capability has allowed for a large amount of spin physics to be done at both PHENIX and STAR, however this is beyond the scope of this dissertation.

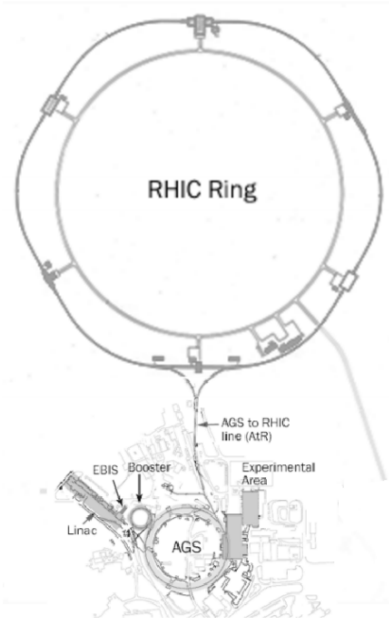

Figure 3.1: Shown is a schematic drawing of the Relativistic Heavy Ion Collider complex

As one can see in Figure 3.1, the RHIC accelerator is a multi stage system. For protons the process starts at the beginning of the Linear Accelerator (Linac). The protons get accelerated down the Linac and into the Booster where they get accelerated further. For heavy ions, instead of the Linac they go from the Electron Beam Ion Source (EBIS) to the Booster. From the Booster, they are injected into the AGS for further acceleration, where a fair number of lower energy experiments are done including some NASA radiation studies. At this stage, the ions are then put into the RHIC ring, at which point they are accelerated to their final collision energy. Once they reach the desired collision energy they circulate the RHIC ring experiencing collisions at the two interaction regions (PHENIX and STAR) in what is referred to as a *store*. A store will typically run for about 6-8 hours until the collision rate drops below a nominal value, at which point the beams are diverted into an absorber and the process begins again.

3.2 The PHENIX Detector

One of the two primary experiments on the RHIC Ring is PHENIX, with the other being STAR. Both PHENIX and STAR were built with, among others, the stated goal of observing and studying the QGP. PHENIX, which stands for Pioneering High Energy Nuclear Interaction eXperiment Adcox et al. (2003b), was designed with two specific goals in mind; the previously stated goal of investigating the QGP, as well as to study the spin structure of the proton through polarized p+p collisions.

Throughout the 16 years of data taking at PHENIX, the detector has been upgraded many times to continually push the bounds of its capabilities. Due to this fact, some in the field like to joke that PHENIX is a detector research and development experiment more so than a physics experiment. However, due to these constant upgrades PHENIX has been able to make measurements that are unparalleled. One of these upgrades which is particularly relevant to my dissertation, was the installation of the Silicon Vertex Tracker (VTX), which provided PHENIX with accurate vertexing capabilities and track projections down to the collision vertex.

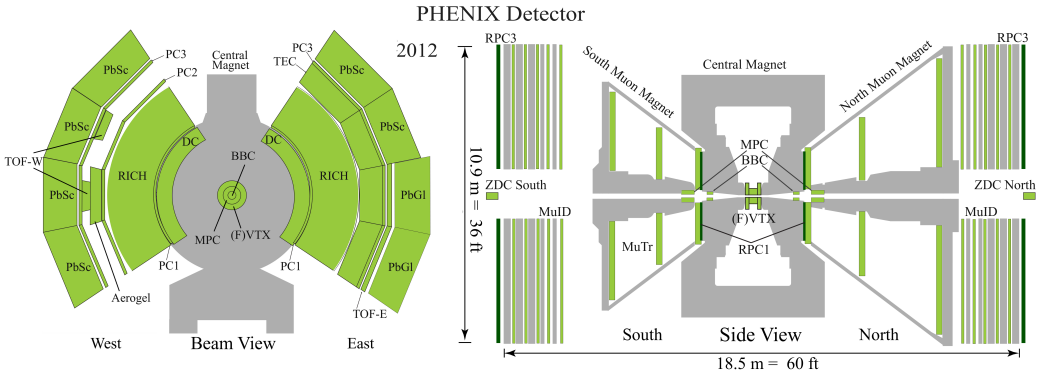

Figure 3.2: Shown is a schematic drawing of the PHENIX detector as of 2015.

As shown in Figure 3.2, the PHENIX detector consisted of two main components: the Central arms, the Muon arms, and some global detectors. The Central arms cover a rapidity range of $|\eta| < 0.35$, and have π radians in azimuthal coverage. The muon arms were

specifically designed for the detection and measurement of muons, and cover an approximate rapidity range of $1.15 < |\eta| < 2.2$.

In addition to the systems shown, there are two relevant global detectors, these are the Beam-Beam Counters (BBCs) and the Zero-Degree Calorimeters (ZDCs) Allen et al. (2003). By measuring the time of flight of particles produced in the collision to the north and south BBC we can determine the z position of the collision vertex, with a resolution of about 3 centimeters. Additionally, the BBC vertex is used as part of event triggering, selecting events with the BBC-z vertex within 10 cm of the center of the detector. The ZDCs are used to study the most peripheral of collisions. Located approximately 18 m away from the collision region, they are designed to measure the products of peripheral collisions that are neutrons traveling very close to the beam path.

3.2.1 Central Arms

The Central arm of PHENIX contains several detectors which are relevant to the heavy flavor measurement described in this dissertation. Working from the inner radius outwards the relevant systems are a silicon vertex detector (VTX), which will be described in some detail in the following sub-section, a drift chamber which provides an accurate measurement of the particle momentum, a ring imaging Cerenkov detector which is used as part of the electron identification procedure, as well as a series of electromagnetic calorimeters. This section will provide a brief introduction to the various detector systems.

3.2.1.1 Silicon Vertex Detector

The Silicon Vertex Detector (VTX) is a silicon tracking detector which provides accurate projection information towards the collision vertex. It was installed in PHENIX between the 2010 and 2011 data taking runs. The VTX can be used to determine the location of the event vertex with about 80 μm precision in Au+Au collisions, as well as to measure the transverse component of the track distance of closest approach (dca_T) to either the event

vertex or to the calibrated beam center. For the sake of this analysis, the dca_T is measured relative to the beam center in order to avoid potential self bias due to the displaced electron being used to determine the event vertex. This topic will be discussed in further detail in section 5.1.

The VTX, described in Kurosawa (2013)Nouicer (2013)Nouicer et al. (2009), is made up of 4 layers, the inner two being pixel detectors which are made up of pixels with an azimuthal position resolution of $\sigma_\phi = 14.4\mu m$, and the outer two being strip pixel detectors with an azimuthal position resolution of $\sigma_\phi = 23\mu m$. A schematic of the VTX is shown in Figure 3.3. The VTX has a ϕ coverage of approximately 1.6π and an η acceptance of $|\eta| < 1.2$ for collisions happening at the center of the interaction region ($z = 0$).

The inner two layers are referred to as B0 and B1 and are made up of 10 and 20 pixel ladders respectively as seen in Figure 3.3. B0 is nominally located at a radial distance from the collision vertex of 2.6 cm, and B1 is at 5.1 cm and provide coverage over the region of $|z| < 10$ cm. While the outer two layers, referred to as B2 and B3, are made up of 16 and 24 silicon stripixel ladders. Unlike the inner two layers which are tightly packed radially B2 and B3 are much more spread out in r. However, for B2 and B3 the mean distances from the interaction region are at 11.8 cm and 16.7 cm respectively.

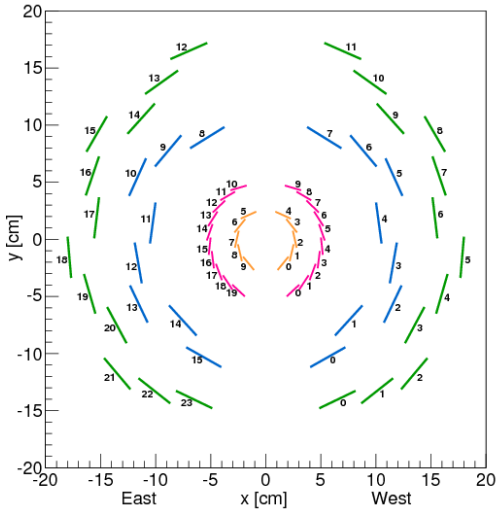

Figure 3.3: A drawing of the VTX detector, from the perspective of the beam pipe (z-direction), the different colors corresponding to the different "layers" B0 through B3.

The VTX can be used in two ways: the first is as a stand alone detector, and the second being combined with the rest of the central arm detector. In PHENIX the VTX stand alone tracks are predominately used to calculate the event vertex with better than $100\mu m$ resolution and could be used to make measurements of inclusive tracks. However, in this analysis, the VTX information is combined with the drift chamber to reconstruct central arm tracks, over the more limited rapidity range of the central arms, providing precise projections to the event vertex. Furthermore these tracks are characterized by precise momentum resolution and excellent electron identification since they use the full set of detector systems in the Central Arms.

3.2.1.2 The Drift Chambers

The next subsystem farther out from the VTX in r are two gas wire chambers called the Drift Chambers (DC), one in each arm. The drift chambers covers a radial distance of 44 cm, between 2.02 and 2.46 m away from the nominal collision point. The drift chambers

only provides coverage in the region of $|\eta| < 0.35$ and therefore have a smaller acceptance than the VTX. A diagram of the drift chamber in one arm is seen in Figure 3.4.

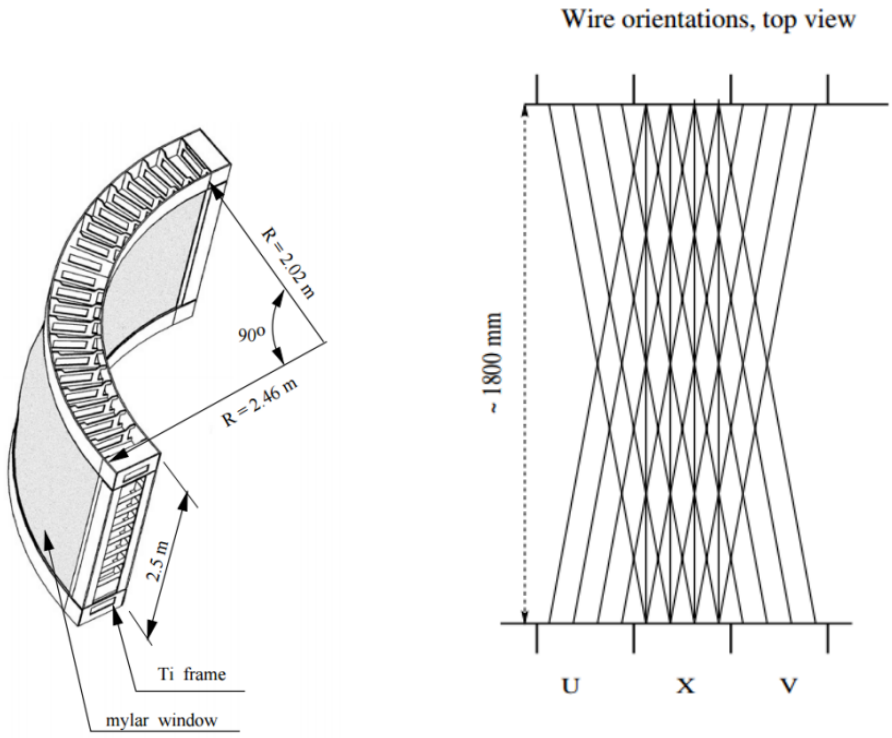

(a) (b)

Figure 3.4: Schematic Drawings of the PHENIX drift chambers, panel (b) shows a schematic of the wire planes within the drift chamber. Adcox et al. (2003a)

The PHENIX drift chambers are filled with a gas mixture which is an approximate 50% ethane and 50% argon, which is ionized by the energy deposited by charged particles traversing the gas. The charged electrons are then attracted to the various anode wires within the drift chamber. The drift chamber is able to provide accurate tracking information through the overlap of these wires which create a sort of grid, as seen in panel b of Figure 3.4. Within the drift chamber there are differently oriented U, X, and V wires, the combination of the three is able to accurately constrain the path a charged particle takes through the

drift chamber. The position in the drift chamber is known with a resolution of $165\mu m$ in $r\phi$ and $2mm$ in z. The drift chamber provides accurate trajectory information and in combination with a magnetic field is used to measure the transverse momentum up to 10 GeV/c with accuracy better than 1%.

3.2.1.3 Ring Imaging Cherenkov Detector

The Ring Imaging Cherenkov (RICH) detector is positioned 20 cm outside the outer radius of the drift chambers Aizawa et al. (2003). It covers a region in radial distance between 2.6 m and 4.1 m, and it is used primarily for the identification of electrons and the rejection of hadrons. The RICH in PHENIX operates on the same principles as any other Cherenkov detector, a particle passing through it at a velocity greater than that at which light can travel through the material will emit light. Since the mass of the electron is very small, electrons emit Cherenkov light over a wide momentum range while heavier particles will not. This light is emitted at a fixed angle relative to the charged track momentum in a azimuthally symmetric distribution. This light is then collected using a series of photo multiplier tubes (PMTs), The number of PMTs which fire within a ring around the track projection are counted and used to identify electron tracks.

The RICH in PHENIX in particular is designed for electron identification below 5 GeV/c. In order to accomplish this, the RICH is filled with CO_2 gas at 1 atm of pressure. This will cause electrons to radiate Cherenkov light beginning at 18 MeV/c while pions will not begin radiating until about 4.65 GeV/c. This means that pion contamination in the identified electron sample begins to appear above 4.65 GeV, and becomes significant above 5. Of course, even in the region that pions begin to fire the RICH, an electron of the same momentum will on average emit more light, therefore it is possible that by requiring a larger number of PMTs fired within a ring shape to use the RICH at high p_T to accurately distinguish between electrons and pions.

3.2.1.4 Electromagnetic-Calorimeters

The EM-calorimeters Aphecetche et al. (2003) are located 5 m from the interaction point and are broken into 8 segments, 6 of which use lead scintillators, and two use lead glass. Each of these systems have their own respective advantages, for example the lead-glass has a better energy resolution, while the lead scintillator has better linearity along with a well understood hadron response.

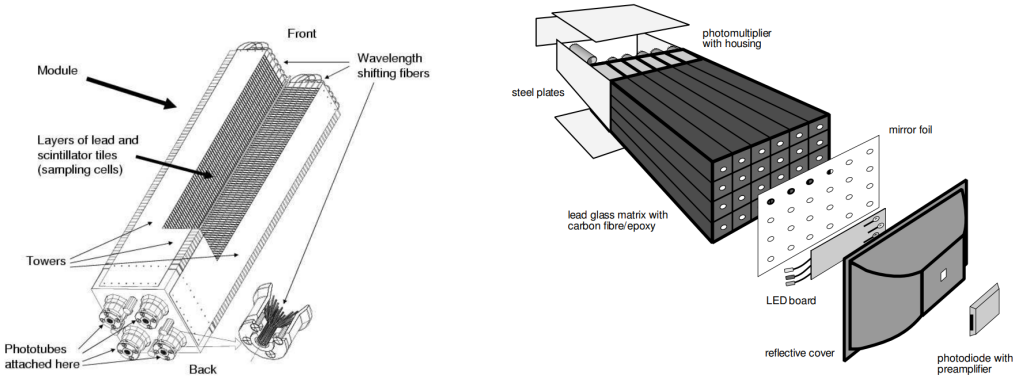

(a) (b)

Figure 3.5: Shown is a schematic of one of the lead scintillator modules (left) and lead glass (right) taken from Aphecetche et al. (2003)

Each lead scintillator module is made up of 66 alternating layers of tiles of lead and scintillators. In each module there are 4 optically isolated towers which are read out individually. This gives the lead scintillators an approximate $5.5cm \times 5.5cm$ spatial resolution. The lead glass towers on the other hand are made up of a continuous 40 cm long lead glass crystal. The individual towers are $4cm \times 4cm$ which provides slightly better spatial resolution than the lead scintillators.

When a particle interacts with either of the calorimeters they tend to produce a electromagnetic shower as they deposit their energy. For electrons and photons in particular, this shower can often spread through into neighboring towers. Therefore, in order to properly

measure the energy of a particle the energy from multiple towers are combined to form clusters.

3.2.1.5 Charged Particle Reconstruction

Charged particles are reconstructed as tracks combining information from the drift chamber, RICH, EM-calorimeters, the VTX, as well as several other detector systems. These tracks are particularly valuable as they combine all of the available detector information in the Central Arms.

These tracks are constructed in two main phases, with each phase being broken down into multiple steps. The first phase is the construction of an object called PHCentralTrack. These are made by first identifying tracks within the drift chamber. The drift chamber tracks are then paired with the pad chamber, this pairing significantly constrains drift chamber track, improving the track resolution. Using the accurate position and momentum information the tracks are then projected to the back of the RICH, where they are matched to a RICH ring (if there are fired PMTs in the area). A parameter called "*disp*", which is the displacement between the center of the RICH ring and the track projection, can be used to remove false matches in higher multiplicity collision systems (such as Au+Au).

Tracks, containing DC, pad chamber and RICH information are then projected out to the outermost detector, the EM-calorimeters. Similar to the RICH, the tracks are matched to the nearest em-calorimeter cluster using two matching parameters *emcdphi* and *emcdz* which are simply the displacement in both ϕ and z between the track projection and the cluster position. For this analysis specific calibration software was developed to normalize these parameters for each EM-calorimeter sector in order to apply selection criteria despite the differences in performance. The energy information provided by the EM-calorimeters and the accurate momentum information from the drift chamber is combined to form an E/p distribution. A calibration procedure for this parameter was introduced which normalizes the mean and sigma of the E/p distribution for each EM-calorimeter sector resulting in a

quantity named *dep*. The *dep* is defined by equation 3.1 where μ and σ are the mean and sigma extracted from a Gaussian fit to the electron E/p distribution.

$$dep = \frac{E/p - \mu}{\sigma} \tag{3.1}$$

Tracks are then projected inwards into the VTX. Using a layer dependent window, the tracks are matched to clusters in the outer layer (B3) of the VTX. If a cluster is found, the projection is modified using the constraint of the VTX hit, if not the windows are widened and the projection is done in both cases to the next layer B2. This process is iterated upon until the track has reached the inner most layer, B0. At this point, the difference between the track projection at each layer and the location of the VTX cluster is combined to calculate a χ^2 in order to judge consistency between the drift chamber projections and the VTX cluster positions. These tracks, which contain all of the central arm information including the VTX are referred to as SvxCentralTracks. In general, tracks with a $\chi^2/ndf < 3$, where *ndf* is the number of degrees of freedom, which are defined by hits in layers B0, B1, and at least one hit in either B2 or B3 are considered to be good VTX tracks.

3.3 Data Acquisition/Triggering

When the RHIC accelerator is operating at its best performance at the beginning of a new store, the collision frequency is highest (up to 10 MHz), it is not possible for PHENIX to record every single event. This is due to the fact that PHENIX is only able to write events to disk at a rate of 6-7 kHz. Using a sophisticated set of triggers PHENIX is able to still record the majority of events of interest.

In order to properly identify the interesting collisions PHENIX uses a series of local and global triggers. The local triggers are designed to parse information from individual subsystems for use in the global on-line trigger. For example, a local level 1 trigger could flag cases where there is at least 1 PMT in each of the two BBCs. The information from various local level 1 triggers is then combined into what is called the Global level-1 trigger

(GL1). For the measurement described in this dissertation two sets of triggers are relevant; the Minimum Bias Trigger (MB) and the Electron-Rich Trigger (ERT).

3.3.1 Minimum Bias Trigger

The Minimum Bias Trigger triggers are solely defined by information provided by the BBCs, and contain no information on the type of particles in the event. This results in a fairly unbiased sampling of the data events, hence the name. Now within the minimum bias trigger pools there are in fact 3 sub-triggers which are recorded of which only one is pertinent to this dissertation.

- $BBCLL1(>0\,tubes)$: Requires at least 1 PMT in each of the two BBCs with a BBC determined vertex between ± 30 cm
- $BBCLL1(>0\,tubes)\,novertex$: Requires at least 1 PMT in each of the two BBCs, however with no vertex requirement.
- $BBCLL1(>0\,tubes)\,narrowvtx$: Requires at least 1 PMT in each of the two BBCs in combination with a BBC determined vertex between ± 10 cm. This trigger matches the acceptance of the VTX, and therefore is the only Minimum Bias trigger relevant to this dissertation.

3.3.2 ERT Trigger

The ERT triggers, contrary to the minimum bias, are design to select a high sampling of high-p_T electromagnetic probes. These triggers work by combining energy measurements from the EM-calorimeter, in which electrons and photons deposit the vast majority of their energy while hadrons typically will only deposit minimum ionizing energy, with information from the RICH. There are 4 different ERT triggers considered for the analysis discussed in this dissertation, although there are technical differences in the way they are defined the main distinction between them is the energy threshold above which they are fully efficient.

In this dissertation heavy flavor electrons are studied as a function of their transverse momentum. Therefore trigger efficiency for the various ERT triggers is understood as a function of the transverse momentum instead of energy, as seen in Figure 3.6.

In order to understand the behavior of the various ERT triggers the trigger efficiency was studied as a function of p_T. This study was done by looking at minimum bias triggered events which pass the BBC narrow vertex trigger and looking at the fraction of electron candidate tracks which pass the various ERT triggers as a function of p_T.

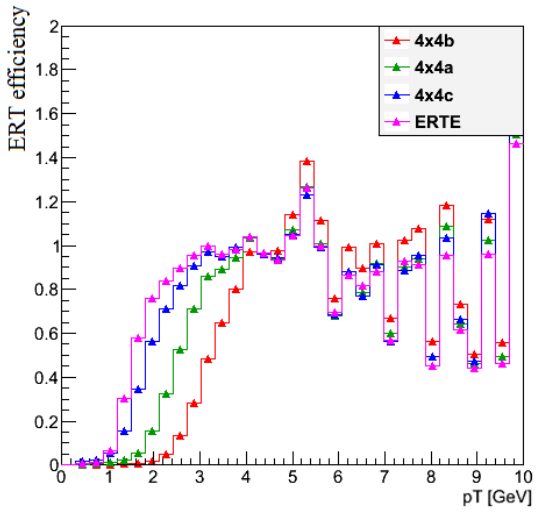

Figure 3.6: Shown is the ERT efficiency as a function of transverse momentum for the run15 p+p data set. One can see the turn on points for the various triggers.

Of the 4 triggers used the ERTE has the lowest energy threshold and actually has no requirement on RICH information. While the other 3 triggers: ERT 4x4C, ERT 4x4A, ERT 4x4B all require RICH photo tubes being fired and the only difference between the three are the different energy thresholds in the EM-calorimeters. For the analysis of the 2015 p+p dataset all 4 of these triggers are combined in order to provide a statistically significant electron sample out to 6 GeV/c in p_T.

3.4 Monte Carlo

In order to model p+p collisions in PHENIX a combination of the PYTHIA event generator with a GEANT Brun et al. (1987) representation of the detector (PISA) is used. GEANT is a powerful simulation package which models the propagation of particles through physical matter. Combining these tools with a set of simulation reconstruction software it is possible to produce simulated data that is a reasonable representation of PHENIX data. Additionally, this analysis used various particle generators to understand specific electron sources.

3.4.1 PYTHIA

As briefly mentioned in the Analysis Overview chapter PYTHIA Sjostrand et al. (2006) is a general purpose built p+p event generator. It is based on leading order QCD calculations and contains theories and models for many aspects of particle collisions, including but not limited to; parton distributions, initial and final state parton showers, decays, fragmentations, as well as hard and soft interactions. PHENIX produced a modified version of the PYTHIA software called PHPYTHIA which uses a Fortran based version of PYTHIA 6 adapted to operate within the Fun4All software framework used in PHENIX.

Within the frame-work of this analysis PYTHIA simulations were run in one of three main configurations, namely $msel = 1, 4, 5$. Where msel = 1 turns on all the hard scattering processes as a pseudo minimum bias, and msel = 4 or 5 forces the production of bottom and charm hadrons. The PHPYTHIA event generator is customized by requiring at least one electron or photon in the central arm of PHENIX to avoid simulating events where no electrons are present or can be produced through photon conversion.

3.4.2 PHParticleGen

Obtaining a large set of high p_T particles with PHPYTHIA would require significant CPU time and disk space, as it generates based on physical processes and following realistic

distributions. To generate particles with equal probability over a large p_T interval a software package called PHParticleGen is used.

PHParticleGen is a fairly simple software package that allows the user to specify the particle type to generate, the p_T range, rapidity (or pseudo-rapidity) interval. It will then generate the desired particles according to these specifications and provide an output that can be used to produce PHENIX simulated events. Unlike PYTHIA, PHParticleGen does inherently apply decays, in order to do so a package called TPythia6Decayer is used, which contains the same default decay table as used in PHPYTHIA. The decay table contains the decay probabilities for the various particles generated, i.e. it contains the probability of a π^0 to decay to $\gamma\gamma$ compared to γe^+e^-. One nice feature of TPythia6Decayer is that one can modify the decay table to force particles to decay only into relevant decay modes which is particularly useful when dealing with small branching ratios, such as the $J/\psi \rightarrow e^+e^-$ decay.

3.4.3 Event Description

When generating simulated events for the analysis there are several key aspects required to ensure that they reasonably represent the data. These include but are not limited to; modeling the detector dead area and having a realistic beam description.

Given that the dca_T is being calculated with regards to the beam center in data, it is very important to ensure that the simulations are generated following a realistic vertex distribution. In order to accomplish this the measured beam center and beam spot size from a representative run were used to describe the event generation in the simulations. To be specific, the simulations were generated with a beam center located at $(x, y) = (161.2\,\mu m, 72.3\,\mu m)$, and following a Gaussian distribution in x-y with $(\sigma_x, \sigma_y) = (129.8\,\mu m, 109.6\,\mu m)$.

In order to model the VTX performance of data in the simulations a representative dead map was used. This dead map is extracted from data and contains information on which areas of each layer were inactive. A comparison of the VTX cluster ϕ distribution between

data and simulation for each layer can be seen in Figure 3.7. Good agreement is observed in the cluster distribution in layers B0 and B1, however in B2 and B3 one can see various ϕ ranges which the data overproduces compared to the simulation. These differences in the ϕ distributions correlate with hot areas in the VTX for that run.

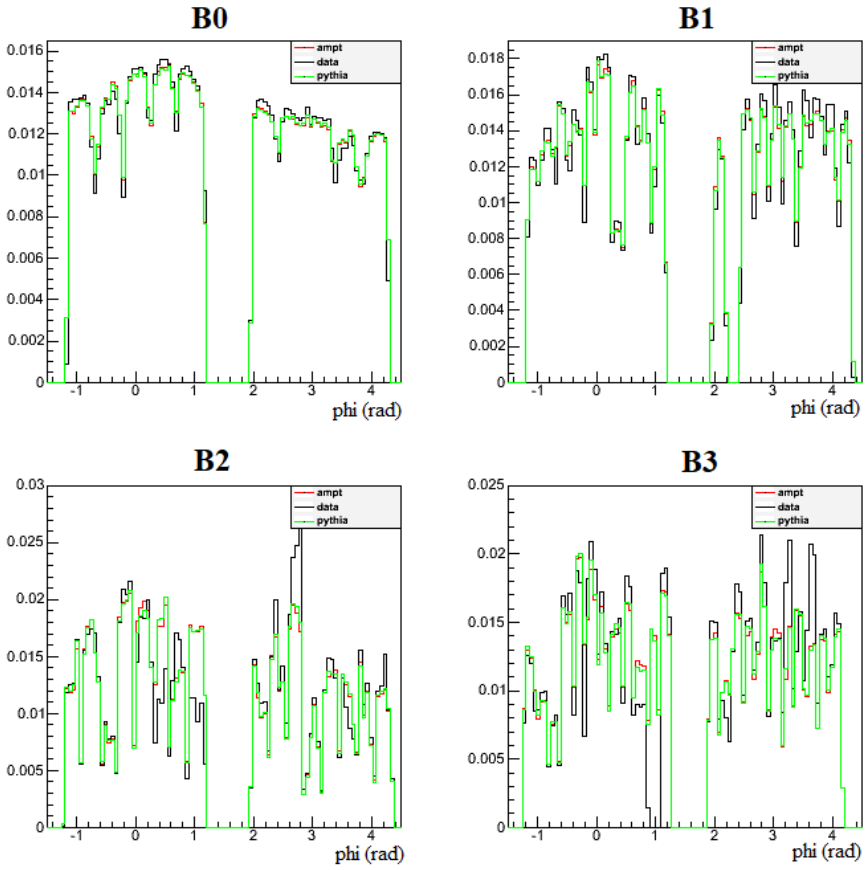

Figure 3.7: Shown are comparisons of the ϕ distributions of clusters between two particle generators and data for each VTX layer. The gap between 1 and 2 radians is due to the incomplete azimuthal coverage of the VTX

CHAPTER 4. HEAVY FLAVOR SEPARATION ANALYSIS OVERVIEW

Before discussing in detail the specific heavy flavor analysis it is useful to outline an overview of the process to provide a framework within which to understand the details of the analysis. This chapter will discuss the relevant measured quantities, basic principle behind the Monte Carlo, as well as a short introduction to the separation technique.

4.1 Measuring Electrons in PHENIX

As previously discussed, in PHENIX all of the central arm track information is put together in an object called SvxCentralTracks. As a reminder these objects include momentum, energy, RICH, as well as accurate tracking information projected down to the collision vertex (or beam center). Each of these quantities have their own particular role in identifying electrons from heavy flavor.

The first stage of measuring electrons in PHENIX is to select an electron candidate sample. This is done by taking advantage of several differences between electrons and hadrons and their interactions with the various detector systems. The first stage of electron identification is done through use of the RICH, by requiring at least 1 photomultiplier tube (PMT) firing for tracks below 5 GeV/c. Above 5 GeV/c, when pions begin to fire the RICH, it is possible to reject the vast majority of the hadron background by requiring 3 PMTs. In order to further reduce the hadron background the normalized energy/momentum (dep) cut is used, which takes advantage of the fact that electrons deposit the vast majority of their energy in the em-calorimeters while hadrons mostly deposit only 2-300 MeV of energy.

4.2 Distance of Closest Approach

Since electrons from heavy flavor decays stem from a weak decay, characterized by a long life time, heavy flavor semileptonic decays produce electrons at a larger distance from the primary vertex compared to QED or QCD processes. In addition, there is a difference between the mean lifetime of B and D mesons resulting in an average $\sim 200\,\mu m$ difference in the decay point for charm and bottom electrons.

While PHENIX cannot measure multiple vertexes within a single event, the VTX can measure the distance of closest approach of electrons. PHENIX measures the transverse component of the *dca*, perpendicular to the beam direction, with respect to the beamcenter in order to remove any bias effects from the vertex. Using the VTX the distance of closest approach in the transverse plane, dca_T, where the VTX has significantly better resolution, is measured.

$$dca_T = L - R \tag{4.1}$$

The parameters R and L represent the radius of the circular track projection in the plane orthogonal to the beam and the distance from the beam center (or determined vertex) and the center of the circular track projection respectively, as seen in Figure 4.1. The dca_T is a signed quantity in this definition. The distinction between positive and negative values of DCAT stem from whether the trajectory is bending towards or away from the beam center.

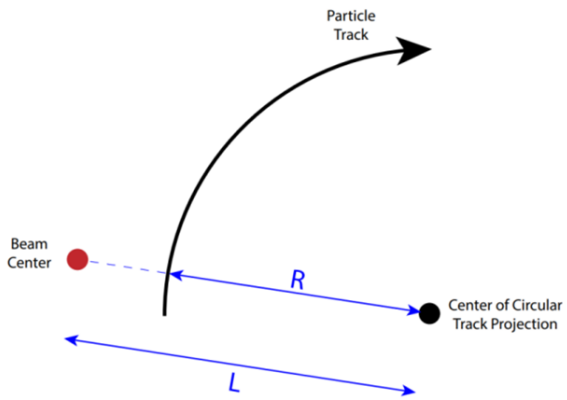

Figure 4.1: Shown is how parameters L and R are determined as used in the calculation of the dca_T according to equation 4.1

Although the dca_T is not a direct measurement of the displaced vertex, it can be used to distinguish between electrons from charm and bottom as seen in Figure 4.2. It is clear from PYTHIA simulations, the dca_T shape of electrons from bottom is noticeably broader than that of electrons from charm. This means that using a template fit to measured electron dca_T distributions it is possible to determine the relative contributions from bottom and charm.

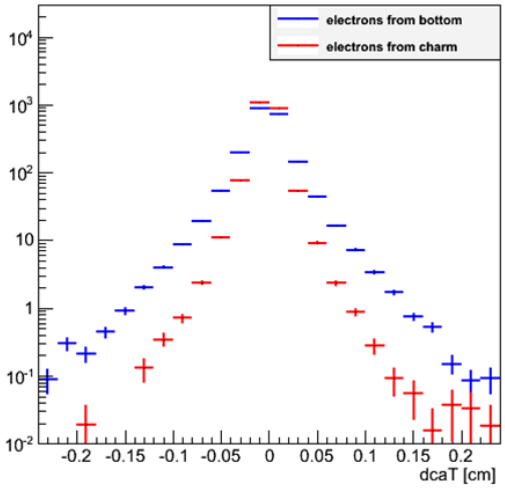

Figure 4.2: Shown is the truth dca_T of bottom and charm electrons as determined using PYTHIA p+p at $\sqrt{s} = 200$ simulations.

4.3 Unfolding Procedure

The fundamental component of the analysis outlined in this dissertation is the Bayesian unfolding procedure. The unfolding allows for extraction of the charm and bottom hadron yields from the measured electron dca_T distributions and previously published inclusive heavy flavor differential cross section measurements. This section will discuss the details of this procedure and some of the statistical principles used.

4.3.1 Bayesian Unfolding

The Bayesian unfolding procedure used in this analysis is based on Bayesian statistics. A detailed pedagogical description of Bayesian unfolding is available in Choudalakis (2012).

The principle question being asked of the unfolding is "Given the measured data (D) and the model, what is the truth level information (T)". This question can be addressed

by using Bayes' theorem.

$$\rho(\mathbf{T}|\mathbf{D}) = \frac{\mathbf{L}(\mathbf{D}|\mathbf{T})\pi(\mathbf{T})}{\mathbf{L}(\mathbf{D})} \tag{4.2}$$

This theorem allows for the calculation of the posterior probability density $\rho(\mathbf{T}|\mathbf{D})$ of the truth information from the likelihood ($L(\mathbf{D}|\mathbf{T})$) and the prior probability density $\pi(\mathbf{T})$. The likelihood function $L(\mathbf{D}|\mathbf{T})$ quantifies the probability of measuring the data D given a sampled truth vector T and a model relating the two. While the *a priori* knowledge is encoded in $\pi(\mathbf{T})$. While the parameter $L(\mathbf{D})$ acts as a normalization parameter so that the quantity ρ can be understood as a probability density.

In this analysis rather than using a simple uniform sampling method, a Markov Chain Monte Carlo (MCMC) algorithm which draws samples of T based on a probability distribution described by $\rho(\mathbf{T}|\mathbf{D})$ is used. Following such a sampling method allows for the unfolding to converge more efficiently than following a simple uniform sampling method. Details on the particular variant of MCMC sampling which is used in these analyses can be found in Goodman and Weare (2010).

4.3.2 Parameter Space

In this analysis the vector space T used in the unfolding is a vector of truth charm and bottom hadron yields integrated over all rapidity.

$$\mathbf{T} = (\mathbf{T_c}, \mathbf{T_b}) \tag{4.3}$$

While the information encoded in the vector D includes measured electron dca_T information for various p_T regions as well as inclusive heavy flavor electron invariant yields ($\mathbf{Y_{hf}}$).

$$\mathbf{D} = (\mathbf{Y_{hf}}, \mathbf{dca_T}) \tag{4.4}$$

In the unfolding procedure the truth information T is propagated through decay and response matrices so it can be compared to the measured electrons through the calculation

of the likelihood $L(\mathbf{D}|\mathbf{T})$. The details of the generation of the decay and response matrices will be described in later sections and chapters.

4.3.3 Evaluating Likelihood

As mentioned previously, the goal of this analysis technique is to extract the parent hadron yields (T) by looking at measured heavy flavor electrons (D) through the window of the unfolding. As the MCMC samples the potential hadron yields each step has to be evaluated using the measured electrons, namely calculating the quantity $L(\mathbf{D}|\mathbf{T})$. In order to formalize this comparison two quantities Y and A are defined as the heavy flavor electron yields and dca_T distributions respectively. Therefore for each step a test Y(T) and A(T) are calculated:

$$\mathbf{Y(T)} = \mathbf{M^{(Y)}T_c} + \mathbf{M^{(Y)}T_b} \tag{4.5}$$

$$\mathbf{A(T)} = \mathbf{M_j^{(R)}}(\mathbf{M_j^{(A)}T_c} + \mathbf{M_j^{(A)}T_b}) \tag{4.6}$$

Where $M^{(Y)}$ and $M^{(A)}$ are decay matrices which contain the probability of a bottom or charm hadron to decay to an electron of a given p_T and dca_T, and $M^{(R)}$ are response matrices which account for reconstruction effects. Then the likelihood between the predicted and measured data set D is calculated. For computational convenience in practice the logarithm of the likelihood function is used rather than the direct likelihood:

$$ln\mathbf{L}(\mathbf{D}|\mathbf{T}) = ln\mathbf{L}(\mathbf{Y^{data}}|\mathbf{Y(T)} + \sum_{\mathbf{j=0}}^{\mathbf{n}} ln\mathbf{L}(\mathbf{A_j^{data}}|\mathbf{A(T)}) \tag{4.7}$$

In the comparison to the data the $\mathbf{Y^{data}}$ set is assigned statistical uncertainties which are assumed to follow a normal distribution. Therefore the contribution to the total likelihood due to the yield comparison is modeled as a multivariate Gaussian with a diagonal covariance. The systematic uncertainties on the yields are taken into account as part of the systematic uncertainty on the final physics results and will be discussed in a later chapter.

The comparisons to the dca_T distributions are handled differently. This is largely because for various p_T regions the distributions are histograms of integer-valued entries.

Therefore the likelihood $lnL(\mathbf{A_j^{data}}|\mathbf{A_j}(\mathbf{T}))$ is more appropriately described by a multivariate Poisson distribution rather than Gaussian as was seen for Y. The measured dca_T distribution is not a pure sample of electrons from bottom and charm and in fact contains various background contributions. The details of the modeling of the background contributions are discussed in a later chapter, and the uncertainties on the precise contributions to the background are taken into account as a source of systematic uncertainty. A potential challenge in the calculation of the likelihood is the fact that due to the highly exponential behavior of the dca_T distributions, the peak region around $dca_T = 0$ will dominate the likelihood calculation due to the small statistical uncertainty in this region. Since most of the information relevant to the separation of bottom and charm stems from larger dca_T and the peak region is strongly affected by the uncertainty on the yield of the various background distributions. In order to mitigate this effect, bins in the dca_T distribution with over 100 counts were assigned a 5% statistical uncertainty. For the 2015 p+p analysis it was verified that this de-weighting of the low dca_T region had no effect on the central unfold value however it slightly reduces the systematic uncertainty associated with the normalization of the background contributions.

4.3.4 Decay Model

This analysis uses the PYTHIA-6 Sjostrand et al. (2006) generator with heavy flavor production process included to model the relation between hadron and electrons. Using the parameter values MSEL = 4(5), which force charm (bottom) production, a decay model was established which contains the information on the relation between a parent charm (or bottom) p_T and its decay electron p_T and truth dca_T. Electrons within $|\eta| < 0.35$, the central arm acceptance of PHENIX, which decayed from the ground state charm hadrons ($D^{\pm}, D^0, D_s, \Lambda_c$) or bottom hadrons ($B^{\pm}, B^0, B_s, \Lambda_b$) were used to create the decay matrix (model) used in the unfolding to compare a sampled hadron yield with the measured electrons. One of the B mesons decay mode is to decay into D mesons, for the decay matrix

these are treated as bottom hadron decays and therefore contribute only to the bottom hadron decay model.

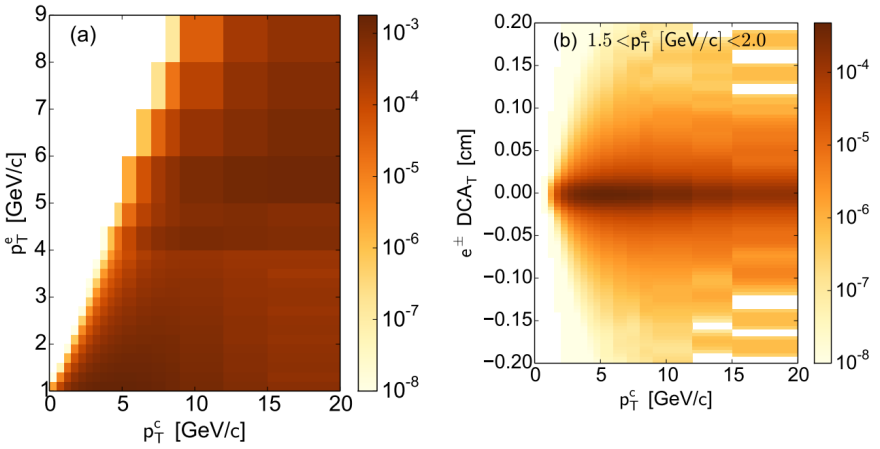

Figure 4.3: From the decay matrix shown are the probabilities of a charm hadron of a given p_T to decay to an electron of given p_T (a) and for a sample electron p_T bin the dca_T (b)

The information in the decay matrices, of which samples are shown in Figure 4.3, are encoded into the unfolding as terms $\mathbf{M^{(Y)}}$ and $\mathbf{M_j^{(A)}}$ of equations 4.5 and 4.6 respectively.

The normalization of the decay matrix is potentially not obvious at first glance. If one integrates the p_T curves in Figure 4.3, the integrals do not turn out to be 1. This is due to the fact that the decay matrix is normalized by the number of generated charm and bottom hadrons at all momenta and rapidity directions, rather than the number of hadrons which decay into electrons within the central arm acceptance.

In principle, this method for producing the decay matrix introduces a model dependence to the hadron yield results, as the unfolding works assuming a PYTHIA-6 decay model. This is not something fully probed in the scope of this dissertation, as no alternative models were used for generating the decay matrix. However, results can be shown for the decay electrons at which point the model dependence is significantly reduced, as it no longer depends on

the PYTHIA description for heavy flavor production and phase-space distributions. This will be discussed further when discussing the results of the 2015 p+p analysis.

4.3.5 Prior and Regularization

One assumption which is made in the unfolding process is that it is expected that the hadron yields are smooth functions. This is implemented in the unfolding as part of the $\pi(T)$ likelihood calculation as a regularization parameter α as seen in equation 4.8

$$ln\pi(\mathbf{T}) = -\alpha^{\mathbf{2}}(|\mathbf{KR_c}|^{\mathbf{2}} + |\mathbf{KR_b}|^{\mathbf{2}}) \tag{4.8}$$

In this expression $\mathbf{R_b}$ and $\mathbf{R_c}$ correspond to the ratio of the bottom and charm hadron yields to $\mathbf{T_{prior}}$. Additionally $\mathbf{K}$ is a 17-by-17 (number of charm and bottom hadron p_T bins) second-order finite-difference matrix of the form seen in Figure 4.4.

$$\mathbf{K} = \frac{17}{2}\begin{pmatrix} -1 & 1 & & & & & & & \\ 1 & -2 & 1 & & & & & & \\ & 1 & -2 & 1 & & & & & \\ & & \ddots & \ddots & \ddots & & & & \\ & & & \ddots & \ddots & \ddots & & & \\ & & & & 1 & -2 & 1 & & \\ & & & & & 1 & -2 & 1 & \\ & & & & & & 1 & -1 & \end{pmatrix}$$

Figure 4.4: Second-order finite-difference matrix used in the calculation of the likelihood due to the regularization, which acts as a penalty on large deviations in the 2nd derivative.

This results in the α parameter applying a penalty on un-smooth departures from $\mathbf{T_{prior}}$. α is a parameter which was tuned specifically for each of the analyses included in this dissertation, the method by which it is tuned will be discussed as part of the 2015 p+p analysis.

However, it is important to note that the uncertainty in the regularization parameter is included as a source of systematic uncertainty in the final results.

The selection of $\mathbf{T_{prior}}$ is potentially a significant one, as it selects the initial starting point of the unfolding procedure. Ideally the result of the technique would not be sensitive $\mathbf{T_{prior}}$ and would always converge to the same hadron yields. In the 2015 p+p analysis the unfolding result was found to be stable when the prior was PYTHIA hadron yields as well as when it was modified by a blast-wave function Adare et al. (2014) (used as the prior in Au+Au). This will be discussed in details as part of the systematic uncertainties of the 2015 p+p analysis.

CHAPTER 5. 2015 p+p ANALYSIS

Using the PHENIX p+p data set measured in 2015 the separated bottom and charm analysis was done. The principles of this analysis are outlined in the Analysis Overview chapter, in this chapter it will focus on the details of the analysis.

5.1 Reference Vertex

As this analysis uses a distance of closest approach measurement to separate bottom and charm hadrons one key aspect is to select a clean unbiased vertex to use. Ideally one would like to calculate the distance of closest approach to the primary collision vertex for that event. The VTX is able to determine the vertex with a high degree of accuracy as it is able to accurately project tracks back to the collision point. If all tracks come from the primary vertex, then it is very accurate in determining the vertex point, however some problems arise in low multiplicity events that contain tracks from a displaced vertex.

P+p events at RHIC energies ($\sqrt{s} = 200 - 510$ GeV) are relatively low multiplicity, resulting in the average event having about 3 good reconstructed tracks in the VTX. If all tracks come from the primary vertex this is sufficient for determining an event vertex, however the track multiplicity is not large enough to remove potential distortion of the vertex due to one or more tracks stemming from a displaced vertex. This implies a bias for the bottom and charm semi-leptonic decays where the measured electrons come from a displaced vertex. For these events, the determined vertex in p+p is pulled towards the heavy flavor decay point, as shown in Figure 5.1.

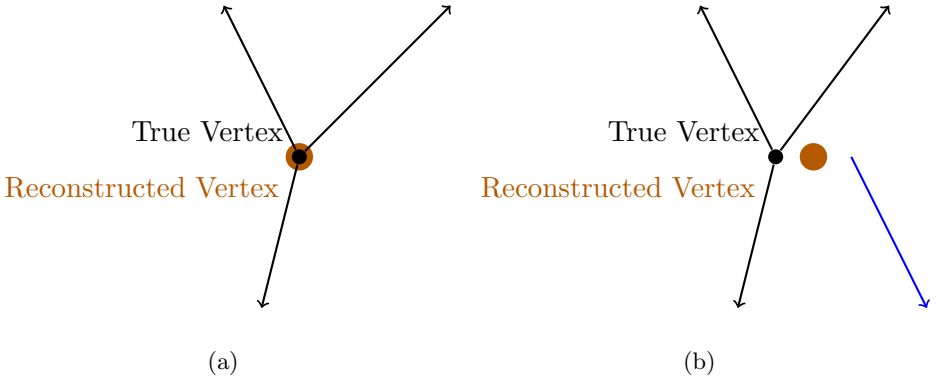

Figure 5.1: When all tracks come from the primary vertex (a) the VTX can reconstruct the correct vertex. When there is a track from a displaced vertex in a p+p event (b) it can bias the reconstructed vertex.

In an attempt to continue to use the reconstructed vertex event by event, the potential removing the displaced track from the vertexing algorithm was investigated. Since the vast majority of the produced charged hadrons came from the collision vertex while a large fraction of electrons are from heavy flavor decays and come from a displaced vertex. Therefore, the vertexing algorithm was modified in such a way as to exclude tracks associated with an electron candidate. Additionally, in an attempt to further improve the vertex resolution a weighted average of the determined x-y vertex and the beam center was introduced. This notably improved the low multiplicity vertex resolution. As one can see in Figure 5.2 the dca_T resolution follows a similar trend to that of the vertex resolution therefore removing the electron track in simulations which contained heavy flavor quarks successfully removes the bias in the vertex. However, removing electron tracks from the vertexing determination worsens the vertex resolution and decreases the number of events where it is possible to use the VTX to determine the event vertex.

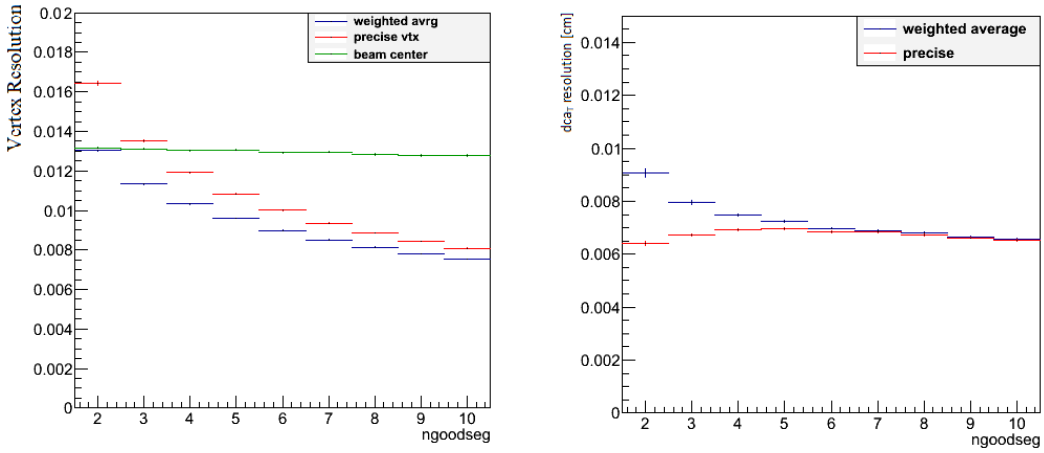

(a) (b)

Figure 5.2: Shown on the left is the vertex resolution as a function of the number of good vertex tracks. Shown on the right are the dca_T resolutions for hadrons in heavy flavor events both without the recalibrator (precise) and with the recalibrator (weighted average) applied

One nice aspect of the dca_T calculation is that it is independent of the z-vertex resolution. This means that all that is needed for an accurate calculation of the dca_T is a reasonable understanding of the x-y components of the vertex. For the 2015 p+p analysis it was determined that the best strategy was to use the beam center calculated run-by-run as the event vertex. Using the beam center the information on the event-by-event vertex is lost, but are instead guaranteed an unbiased vertex for the dca_T calculation and maximize the available electron statistics. In this case, the dominating effects on the dca_T resolution are the physical size of the beam spot at the collision point, as well as the intrinsic VTX tracking resolution.

5.2 Run QA

A key step for any physics analysis is to understand the detector performance throughout the full data taking run and to select a series of good runs in which the detector was working well. During the 2015 proton-proton collision data taking run, 884 physics runs were collected, where a physics run is defined as an individual data taking period which typically lasts up to 90 minutes. Using metrics for quality assurance (QA) as described below a set of good runs was selected, throughout which detector performance was reasonably consistent. The run QA is done using the minimum bias BBC-narrow trigger to avoid any run to run variation due to changes in trigger mixing.

5.2.1 Parameters for Quality Assurance

In order to identify runs as either 'good' or 'bad' several parameters were used as a metric. The full list of parameters used for selection is listed below. Both event level quantities as well as track level quantities as a function of run number were used to flag questionable runs. One thing to notice about the list below, not all quantities are independent, with the potential for significant redundancy amongst the parameters.

(a) Event Level Variables

- Number of minimum bias (MB) narrow vertex events
- Fraction of events with a vertex determined using the VTX detector: Provides information on the big picture performance of the VTX detector

(b) Cluster Variables

- Mean number of VTX clusters per event: Provides information on the performance of each layer of the VTX by looking at the mean number of hits.

(c) PHCentralTrack Variables

- Mean number of reconstructed hadron tracks per event: Provides information on the performance of the drift chamber
- Mean number of reconstructed electron tracks per event: Provides information on the combined performance of the drift chamber EM-calorimeters and RICH

(d) VTX Stand Alone Track Variables

- Mean number of standalone tracks per event: Provides isolated information on the VTX tracking performance

(e) SvxCentralTrack Variables

- Hadron tracks per event: Provides information on VTX tracking performance coupled with the drift chamber
- Hadron DCA mean: Provides information on the stability of the VTX
- Hadron DCA width: Provides information on the stability of the VTX as well as the beam spot size

In order to properly understand the effects from each catagory a set of quality and electron identification cuts were used. The full list of cuts which were used to identify each of these categories is listed below.

VARIABLE	CUTS
MinBias Events	• Trigger: `BBCLL1(>0 tubes) narrowvtx` • `pmtbbcs > 0 && pmtbbcn > 0` • |BBC-z vertex| < 10 cm
Electron PHCentralTrack	• `Good DCH track` • $p_T > 0.5$ GeV/c • $\chi^2/\text{ndf} < 6$ • `n0 >= 1` • `disp < 5`
Hadron PHCentralTrack	• `good DCH track` • $p_T > 0.5$ GeV/c • $\chi^2/\text{ndf} < 6$ • `n0 < 0`
Hadron SVXCentralTrack	• `good DCH track` • $p_T > 0.5$ GeV/c • $\chi^2/\text{ndf} < 6$ • `n0 < 0` • Require a hit in B0 and B1
VTX Stand Alone Track	• $p_T > 0.5$ GeV/c • $\chi^2/\text{ndf} < 6$

Table 5.1: Cuts defining the variables used for quality assurance and run selection. *Note: n0 refers to the number of photo-tubes fired in the RICH.*

5.2.2 Run-By-Run Quality Assurance

Since this measurement relies heavily on the dca_T measurement done using the VTX this section will highlight some of the run-by-run QA figures that were looked at in order to understand and identify runs with good performance. One of the metrics looked at was the rate of finding VTX stand alone tracks (SvxSegments) per event, as seen in Figure 5.3. For each run flagged as potentially bad a relevant base quantity was looked at in order to understand the source of the issue. As seen on the right panel, run 426443 which was flagged as potentially bad had one layer of the VTX (B2) offline during the run. This run, and

others like it, were excluded from the analysis as this would effect the tracking performance and therefore the dca_T resolution.

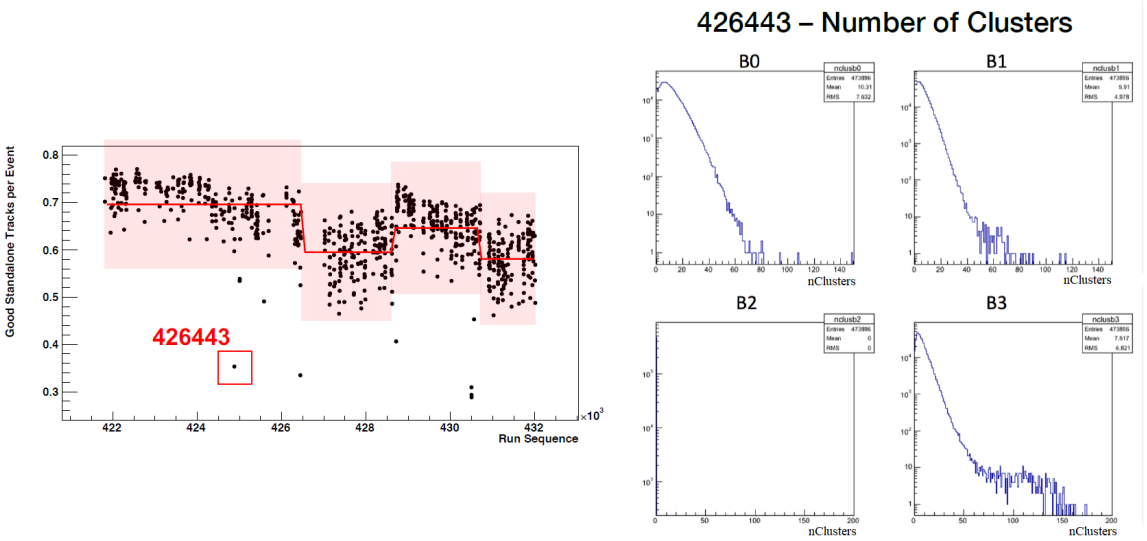

Figure 5.3: Shown are the mean number of VTX stand alone tracks as a function of run number (left) and a sample VTX cluster distribution from a run identified as bad due to this check (right).

A more direct metric for verifying the VTX detector performance is to look at the number of clusters in each layer per event. This allows for a more direct visualization of what is seen on the right panel of Figure 5.3, and can be seen in Figure 5.4. Do note, for the sake of this Figure runs where an entire layer of the VTX was dead are excluded. Looking in this figure, it is observed that there are some long range trends throughout the 2015 p+p data set in layers B1 and B2. These correlate to changes in the live area, as the electronics for the VTX either drop out or recover. Additionally the sharp changes in B0 correlate to individual ladders within B0 (or half-ladders) dropping in and out for individual runs which, although far from ideal, is common for the VTX.

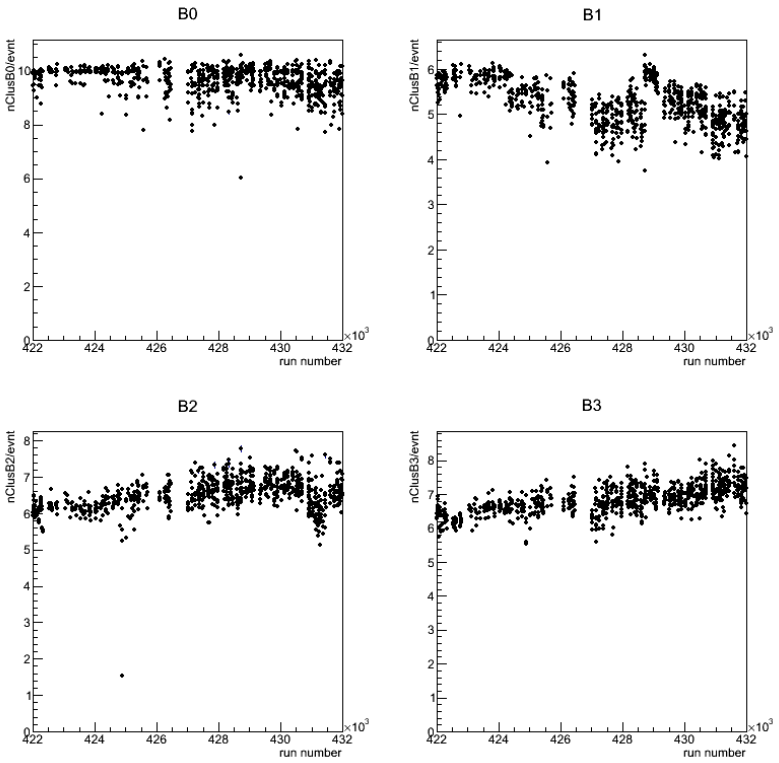

Figure 5.4: Shown are the mean number of VTX clusters in each layer as a function of run number, excluding runs where the number of clusters in a layer are 0

To ensure that each run sampled a comparable kinematic region and had similar acceptance, tracks reconstructed in the central arms independently of the VTX were looked at. This involved looking at the PHCentralTrack information, such as the number of good PHCentralTracks per event, or the number of PHCentralTrack electrons per event (as described in table 5.1). A sample of the PHCentralTrack electrons per event as a function of run number is seen in Figure 5.5. For each run flagged by this metric the $\phi - z$ distribution of PHCentralTracks were looked at (as seen on the right panel). Most of the issues observed were explained by areas of the drift chamber, RICH or EM-calorimeter dying during a run (as seen in run 422615).

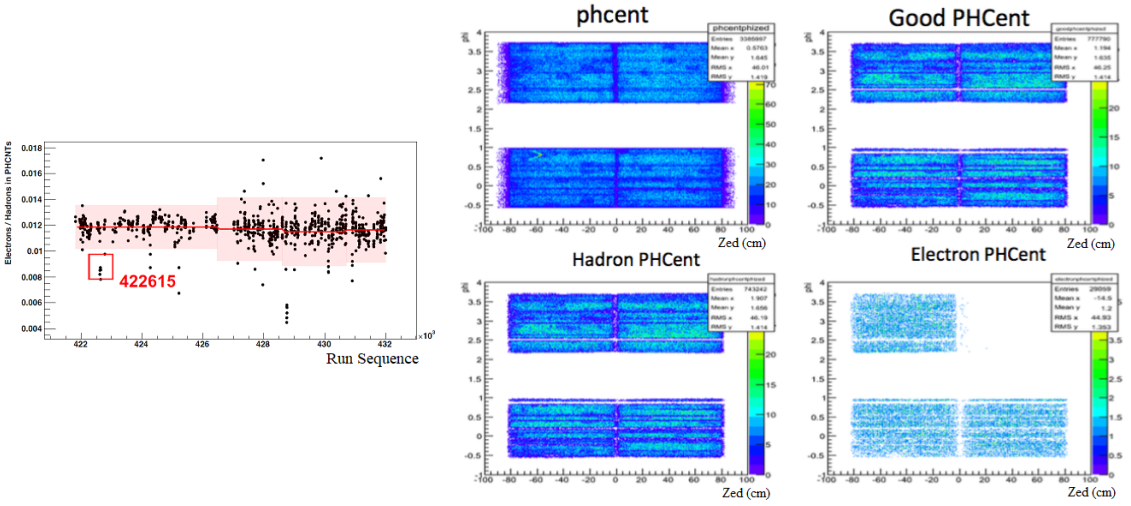

Figure 5.5: Shown are the mean number of PHCentralTrack electrons as a function of run number (Left) and a sample PHCentralTrack distribution from a run identified as bad due to this check (right).

Of the runs in which no noticeable issues were seen in the VTX or drift chamber parameters, the dca_T resolution was looked at as a function of run number. The resolution was determined by fitting the Gaussian portion of data hadron distributions for each run. After excluding bad runs a relatively tight, flat dca_T resolution is observed, as seen in Figure 5.6.

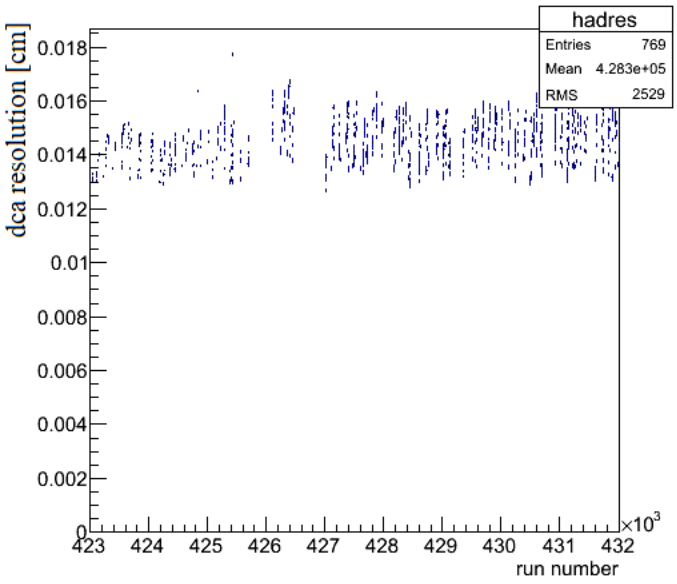

Figure 5.6: Shown dca resolution [cm] of hadrons in data as a function of run for runs not flagged by other QA checks

Throughout the Run-By-Run QA 115 runs were identified as having detector performance issues. This amounted to using approximately 85% of recorded events in the analysis.

5.3 Analysis Cuts

5.3.1 List of Electron Identification Cuts

A series of electron identification and track quality cuts were developed to select a pure electron sample. In order to improve the purity at high p_T and maximize statistics at low p_T the electron identification cuts were tightened for only p_T above 5 GeV/c. This is because, as discussed previously, charged pions begin firing the rich above about 4.5 GeV/c, as seen in figure5.8.

- If $p_T < 5$ GeV/c

  - $prob > 0.01$
  - $n0 > 1$
- If $p_T \geq 5$ GeV/c
  - $prob > 0.2$
  - $n0 > 3$
- $|dep| < 2$
- $|emcdphi| < 3\sigma$
- $|emcdz| < 3\sigma$
- $disp < 5$cm
- Conversion veto cut applied

Where $n0$ corresponds to the number of photo multiplier tubes in the RICH, *dep* is the normalized energy to momentum ratio, and *prob* is the probability of the shower in the EM-calorimeter being electromagnetic. Additionally emcdphi and emcdz are matching parameters for the projection of the central arm track to the EM-calorimeter clusters.

5.3.2 List of Track Selection Cuts

The following cuts are used on VTX-level variables to ensure high quality SvxCentralTracks.

- $\chi^2/ndf < 3$
- quality = 31||quality = 63 (encoded drift chamber track quality information)
- $hitpattern\&3 = 3$ (requires at least one hit in each of the inner two layers of the VTX)
- $nhit > 2$ (requires hits in at least 3 layers of the VTX)

- $|zed| < 75$ cm

The quality = 31||quality = 63 ensures that the drift chamber track is of high quality. The χ^2/ndf cut ensures that the drift chamber track is well matched to the VTX clusters.

For several of the listed track quality and electron identification cuts the distributions of the parameters in data is shown below. In the creation of these figures, the full set of analysis cuts except the shown quantity was applied. These distributions are broken up for each p_T bin, so that any p_T trend, if present, can be observed.

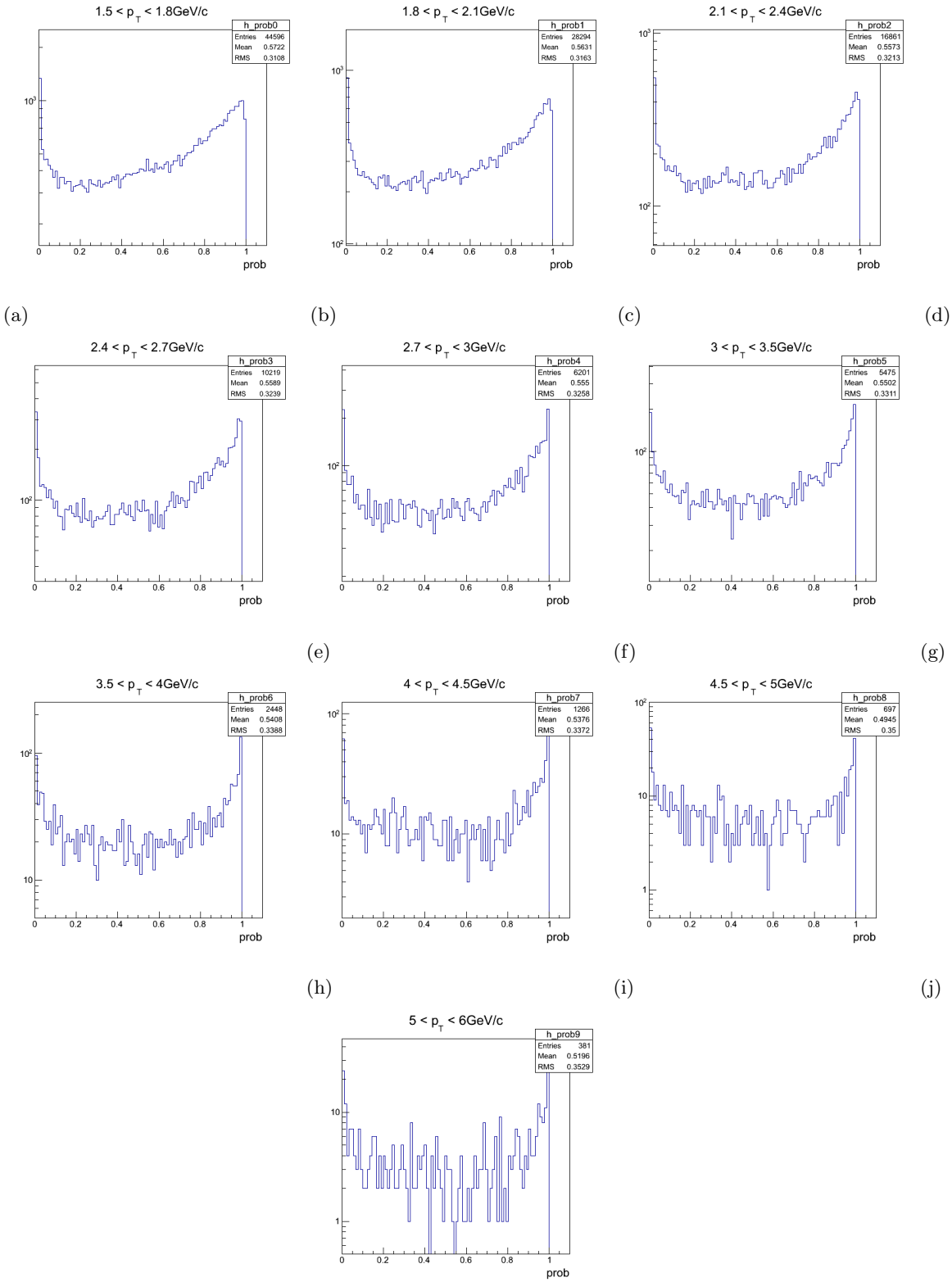

Figure 5.7: Distribution of prob (probability of EM-calorimeter shower being electromagnetic), for tracks which pass all other analysis and EID cuts

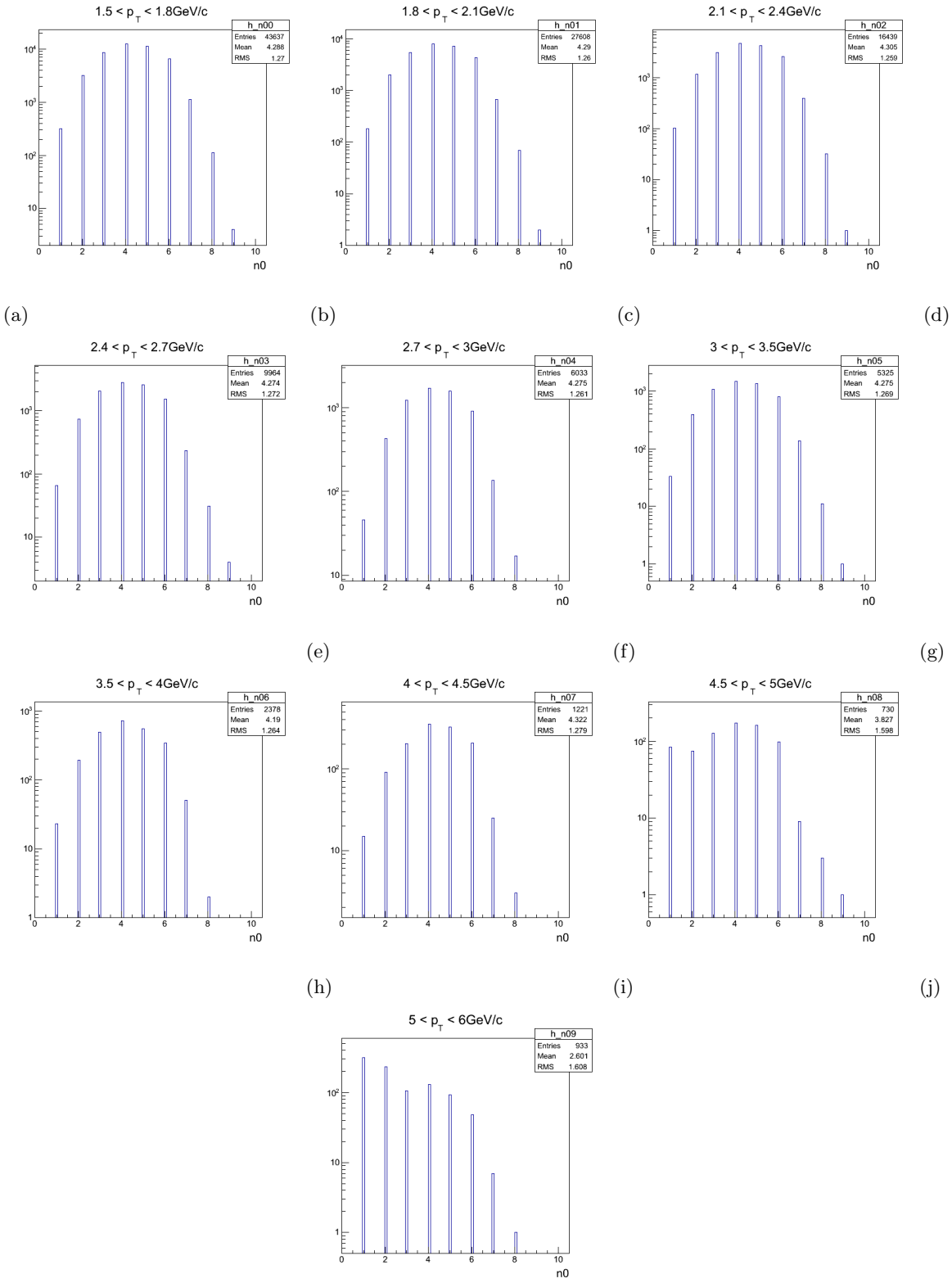

Figure 5.8: Distribution of n0, for tracks which pass all other analysis and EID cuts, with an additional $n0 > 0$ requirement to exclude the dominant hadron peak

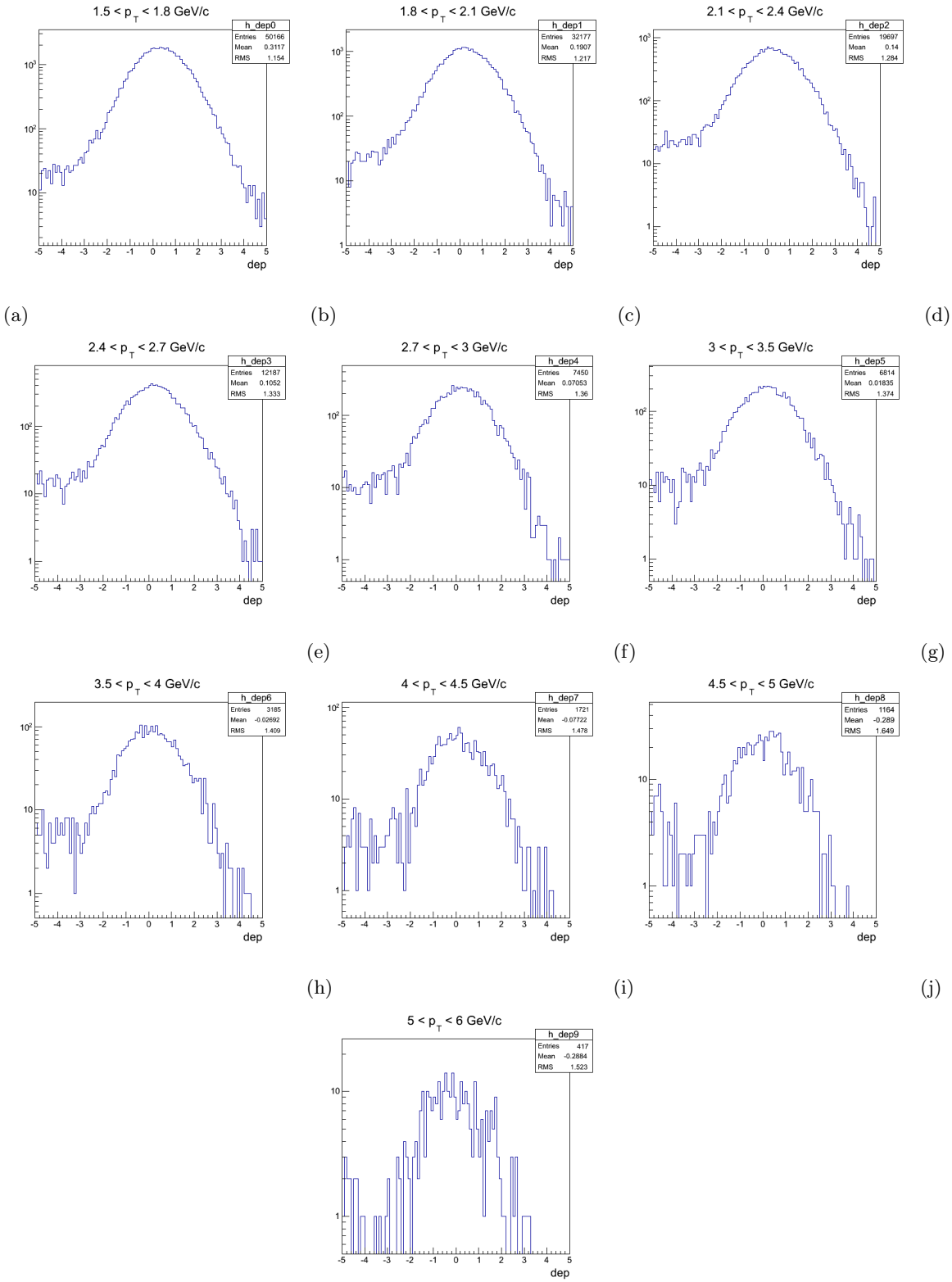

Figure 5.9: Distribution of normalized E/p (dep), for tracks which pass all other analysis and EID cuts

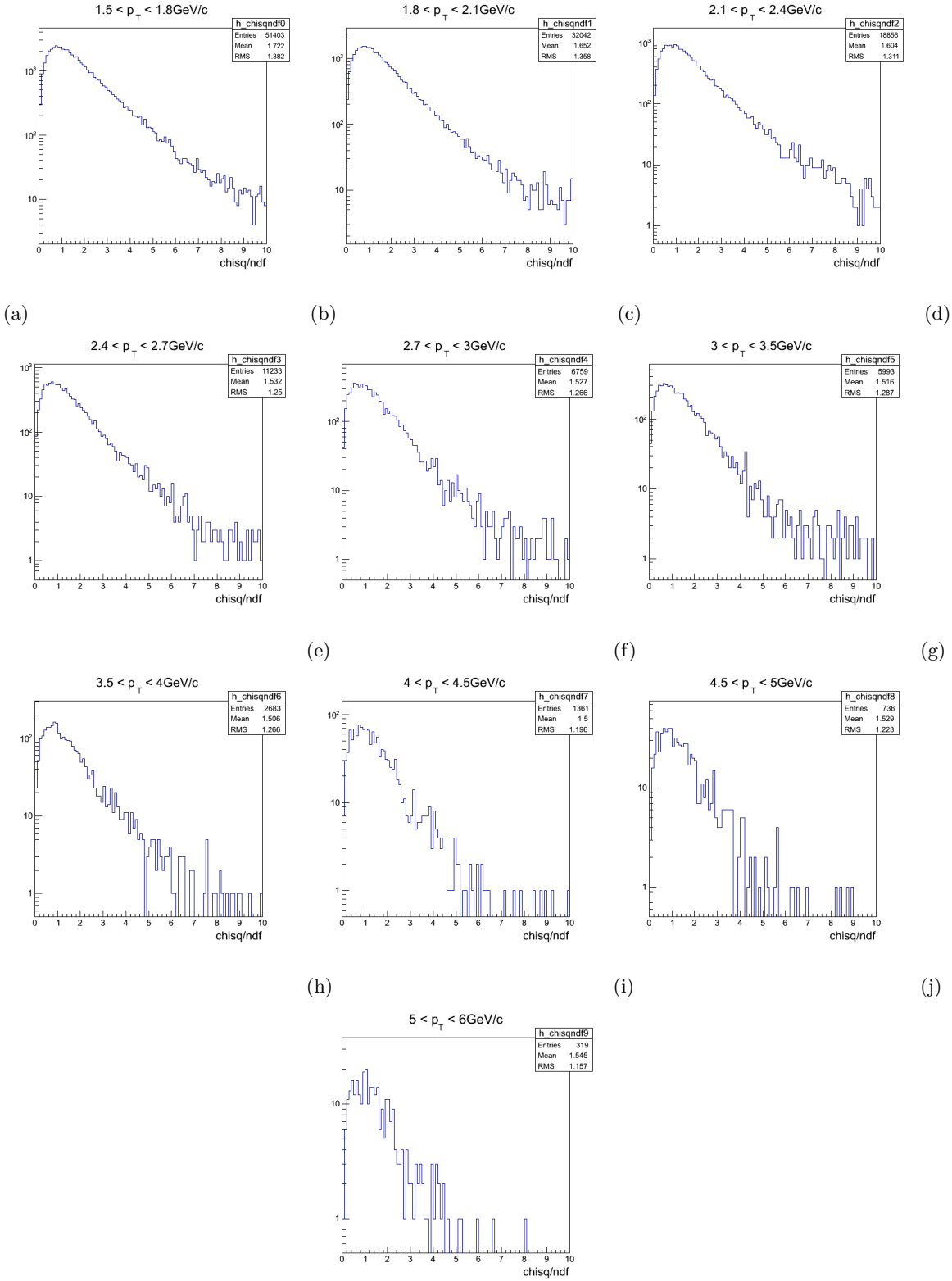

Figure 5.10: Distribution of chisq/ndf, for tracks which pass all other analysis and EID cuts

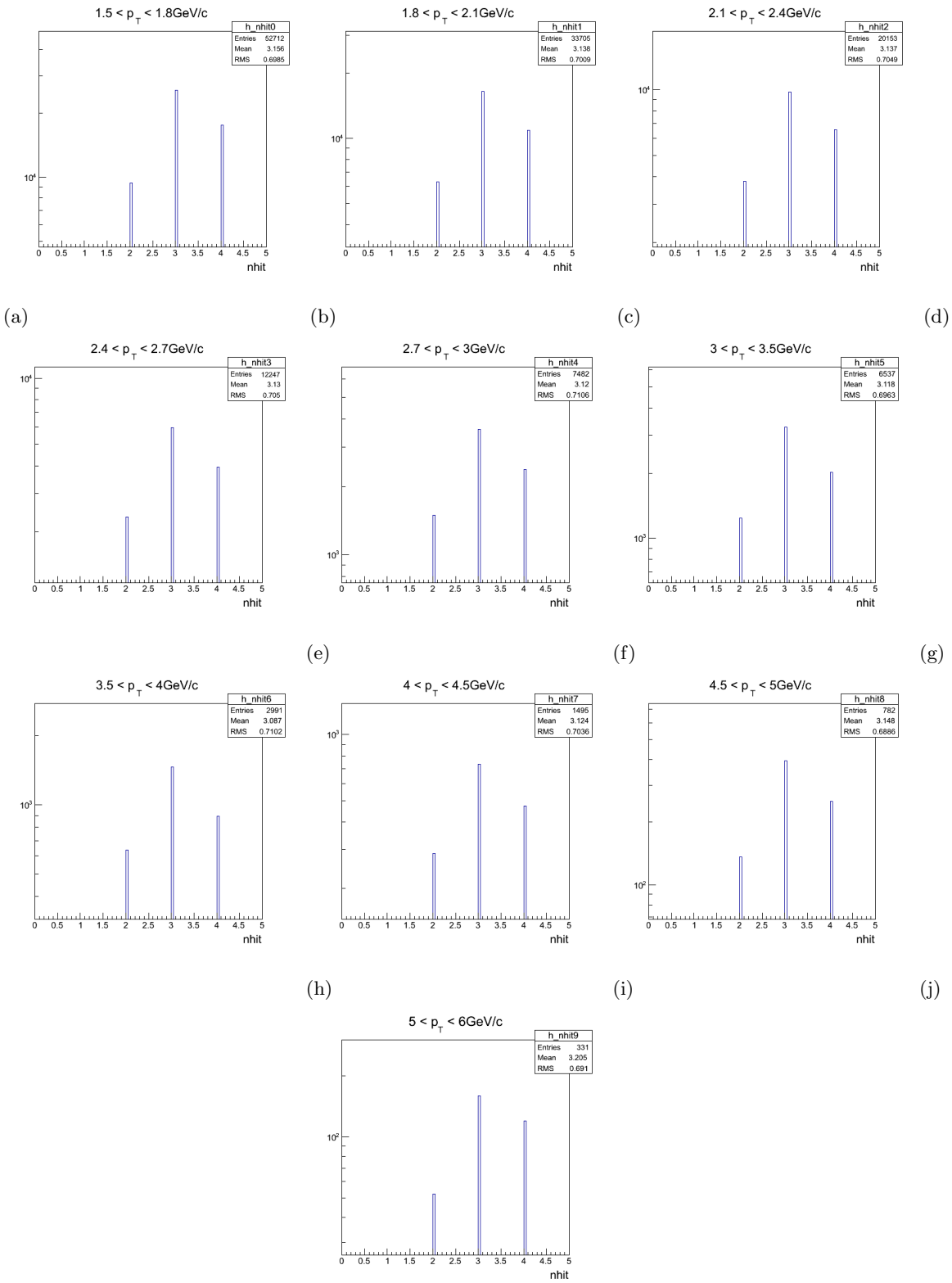

Figure 5.11: Distribution of the number of VTX layers with hits, for tracks which pass all other analysis and EID cuts

5.4 dca_T Resolution

As was previously discussed, in this analysis it is critical to understand the dca_T resolution. The unfolding technique used in this analysis uses in part template fitting to the measured electron candidate dca_T distribution, therefore it is sensitive to the accuracy of the measured dca_T resolution.

In order to extract the dca_T resolution, hadrons in data were fit using a Gaussian, similar in technique to the extraction of the dca_T template for the hadron contamination, limiting the fit region only to the Gaussian portion ($\pm$ 300 microns). This is used to extract the dca_T resolution, as the majority of hadrons come from the primary vertex with a truth dca_T of 0. Therefore the Gaussian resolution measured is determined by the dca_T distribution. It is important to note that there are tails in the hadron dca_T distribution due to long lived decays, however they do not affect the fit to the peak region. In order to provide as accurate of a representation of the electron candidate sample the hadron dca_T distribution was measured run-by-run, and weighted based on the relative contribution that a run has to the total electron candidate sample. This weighted combination is required to model the electron candidate resolution due to the fact that changes in the ERT trigger run-by-run cause the electron/hadron ratio to change. The extracted dca_T resolution as a function of p_T can be seen in Figure 5.13.

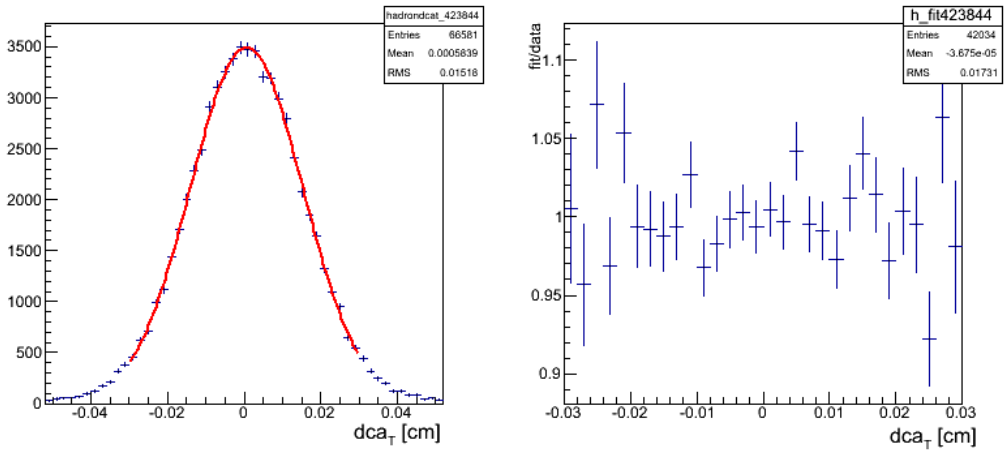

Figure 5.12: dca_T distribution of hadrons for run 423844 fit with a Gaussian for $1 < p_T < 1.5$ GeV/c, on the right panel the ratio of the fit to the data was taken, and good representation consistent with the hadron dca_T being well described by a single Gaussian in the peak region is observed.

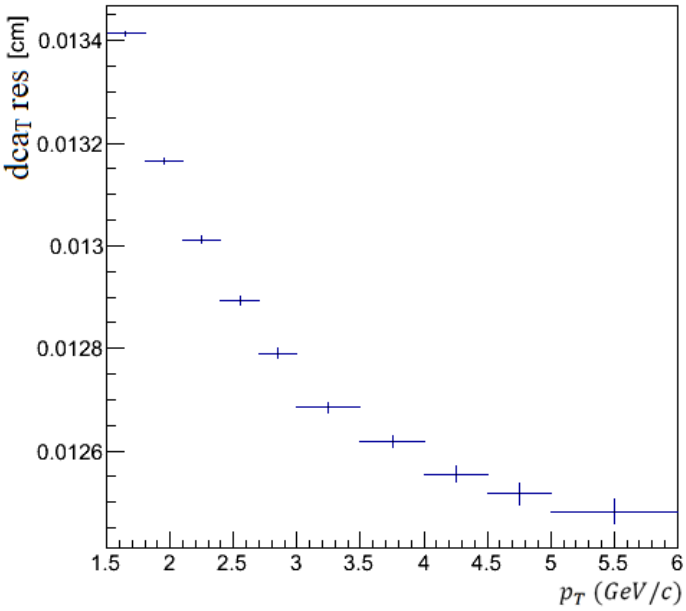

Figure 5.13: dca_{T_σ} extracted from hadrons in data as a function of p_T for the entire data taking run

Extracting the resolution of the total summed hadron dca_T distribution relies on the assumption that for a given tight p_T window the resolution for each run is a single Gaussian, and that there is a normal distribution of dca_T resolutions as a function of run number. This was looked at, by looking at a histogram of the dca_T resolution of each run as shown in Figure 5.14. Additionally the ratio of a single Gaussian fit to the hadron dca_T distribution was looked at, and it is observed that the distribution in the peak region is well described by a single Gaussian, as seen by the agreement between the red fit line and the data points in Figure 5.12.

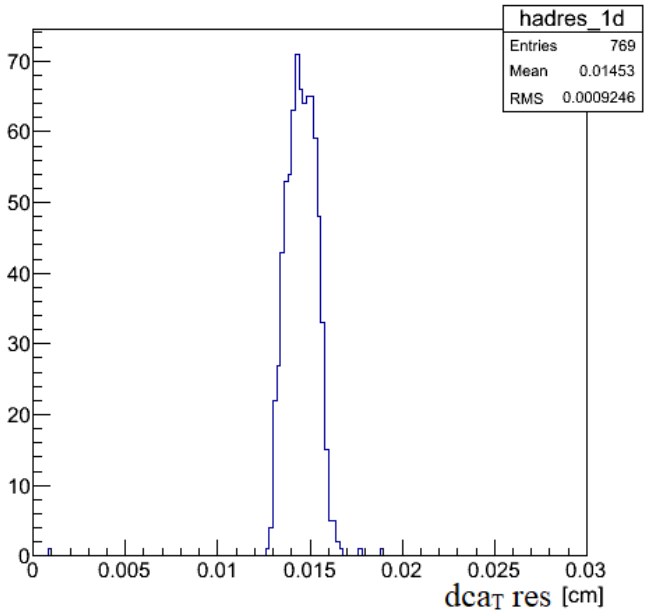

Figure 5.14: dca_{T_σ} measured run by run, for tracks with $p_T > 1.5GeV$, observe a Gaussian distribution

5.5 Understanding Background Contributions

The measured electron candidate dca_T distributions are used as input to the unfolding procedure together with the transverse momentum spectra of inclusive heavy flavor electrons. As these are direct measurements of all electron candidates it is clear and safe to assume that they are not a pure sample of electrons from heavy flavor decays. In fact there are many sources of background contaminating the heavy flavor electron candidates. In order for the unfolding analysis to work, each source of background has to be properly modeled, both in contribution and dca_T shape.

The background sources are classified into two main groups; background electrons coming from non-heavy flavor sources and hadron contamination. The way the two large groups

are estimated within the analysis are noticeably different and will be described in detail in this section.

5.5.1 Hadron Contamination

Hadrons, mistakenly identified as electrons in the central arms, constitute a critical source of background which must be accounted for in this analysis. There are two main sources of misidentified hadrons: (*i*) At low track p_T, they stem primarily from multiplicity effects. Although rare in $p+p$ collisions, a hadron track can occasionally share a hit in the RICH with another particle track. (*ii*) At high p_T, particularly $p_T > 5$ GeV/c, charged pions can fire the RICH. Using the $n0 > 3$ cut at high p_T minimizes this effect to the order of a few percent. In this analysis the hadron contamination is estimated using two methods, taking the weighted average of the two for the measured hadron contamination. One of the two methods used is a *dep* fitting method, which takes advantage of the different shape of hadrons and electrons when looking at the *dep* distribution. The second method estimates the hadron contamination by looking at the survival rate of the applied n0 cut, which allows for a shape independent estimation of the hadron contamination.

5.5.1.1 Estimation Through Dep Fitting

A valuable way to estimate the hadron contamination, is by fitting the *dep* distribution of electron candidates. This method takes advantage of the fact that hadrons (largely charged pions) have a different *dep* shape than true electrons. By construction, true electrons have a Gaussian *dep* shape, with a $\sigma \sim 1$ and mean ~ 0, while hadrons follow more of a falling exponential, as shown in Figure 5.15.

In order to extract the hadron contamination estimation, the hadron ($n0 < 0$) *dep* distribution in data was examined and fit. This fit serves as a hadron template in the fit to the electron candidate *dep* distribution, with the only free parameter being the total number of hadrons contaminating the electron sample. The electron candidate *dep* distribution was

then fit with a summation of the hadron *dep* template, and a Gaussian in order to extract both the electron and hadron contribution. The hadron contamination is determined by the ratio of the integral over the *dep* cut region ($|dep| < 2$). The extracted contamination fractions are quantified in Figure 5.19.

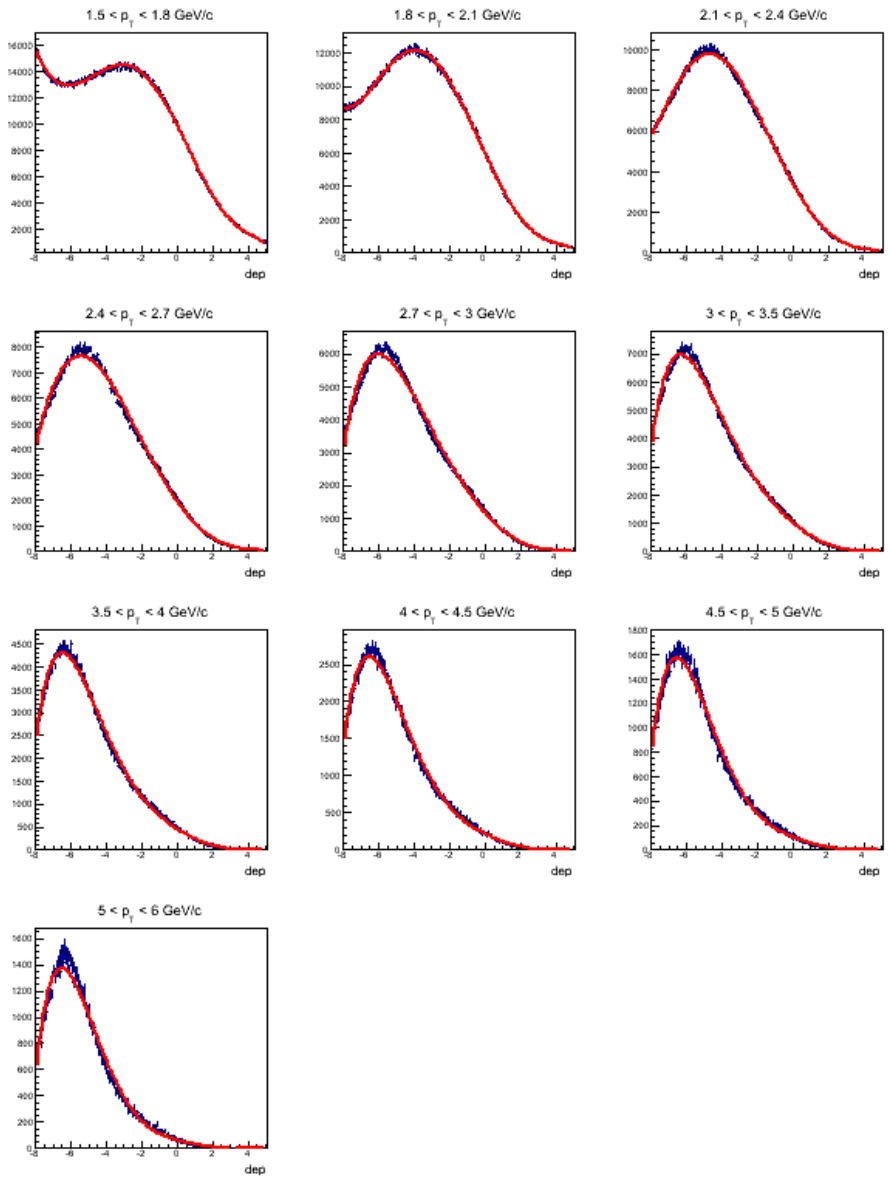

Figure 5.15: Fits to the hadron `dep` distribution to construct a template for the shape of the hadron contamination used to fit the electron candidate *dep* distribution.

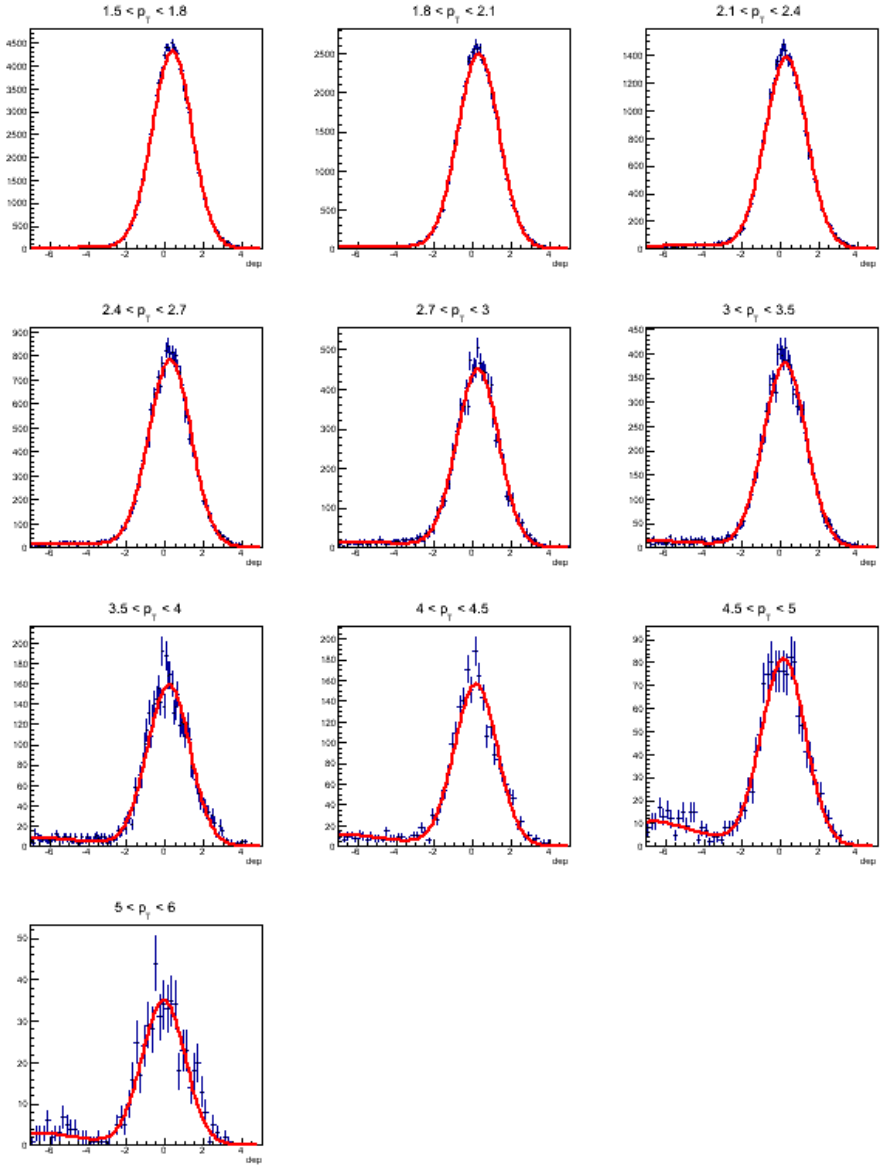

Figure 5.16: Distribution of the `dep` variable for electron candidate tracks in various p_T selections fit by a Gaussian + hadron template.

5.5.1.2 Algebraic Estimation

An alternative way to estimate the hadron contamination, independent of the *dep* shape, is to use the survival rate of the n0 cut. This method takes advantage of the fact that

electrons and hadrons (namely charged pions) appear differently in the RICH, and therefore have a different probability to pass the n0 cut applied. Therefore, by measuring the number of electron candidates both with and without the n0 cut applied (n_{n0} and n_{non0} respectively), and estimating the survival rates for electrons from simulations and charged pions by looking at tracks in data with a $dep <$ -6 (where the dep distribution is purely hadrons) it is possible to estimate the hadron contamination.

$$n_{non0} = n_e + n_h \tag{5.1}$$

$$n_{n0} = \epsilon_e n_e + \epsilon_h n_h \tag{5.2}$$

$$n_{h_{n0}} = \epsilon_h \frac{n_{n0} - \epsilon_e n_{non0}}{\epsilon_h - \epsilon_e} \tag{5.3}$$

Where n_e and n_h are the number of hadrons and number of electrons in the data set, with no n0 cut applied, and ϵ_e and ϵ_h are the probability of an electron or hadron to pass the n0 cut. ϵ_e is determined from single particle electron simulations, while ϵ_h is determined by looking at hadrons in data with a $dep < -6$. These values, for both $n0 > 1$ (used at $p_T < 5$) and $n0 > 3$ ($p_T > 5$) are shown in Figure 5.17.

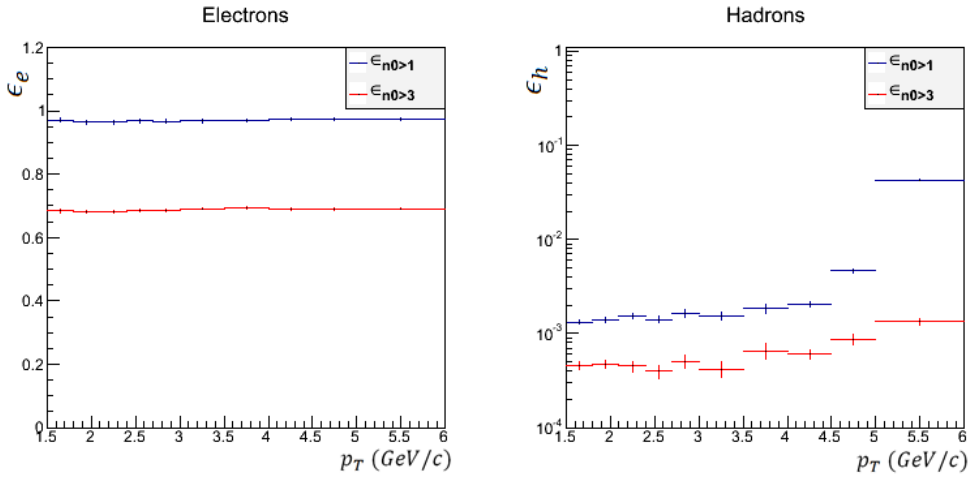

Figure 5.17: The survival rates of the n0 cut for both single electron simulations, and hadrons in data

As an additional check that the simulated single electrons act as a reasonable approximation for the electrons in data, the ratio of tracks with at least four photo tubes in the RICH to those with at least 2 ($\frac{n0>3}{n0>1}$) was looked at. Comparing the single electron simulations and to the data electron candidates with tight electron identification cuts, this was looked at for electrons between 1.5 and 4 GeV. The results are consistent within the large statistical uncertainty in the data measurement, as seen in Figure 5.18.

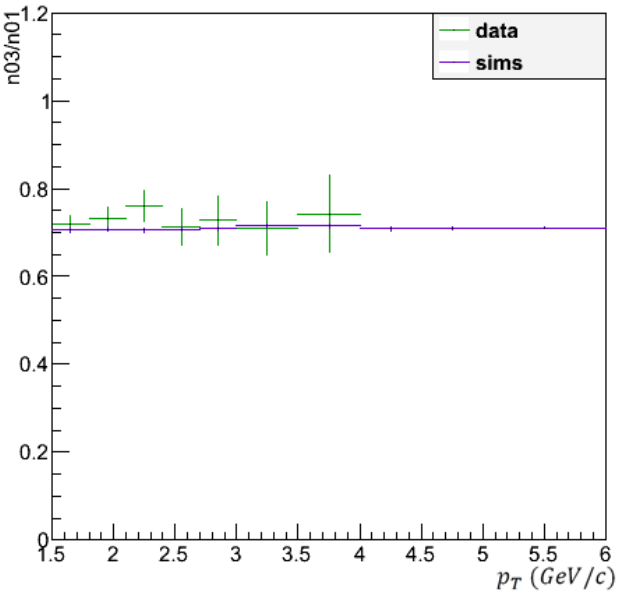

Figure 5.18: The ratio of electrons with $n0 > 3$ to $n0 > 1$ was compared between data and simulations. In data electrons were identified using a $|dep| < 1$ cut

5.5.1.3 Measured Hadron Contamination

For each method the fraction of electron candidates which are actually hadrons was estimated. As these two methods provide independent measurements of the hadron contamination, the weighted average of the two results was taken, using as weight the inverse of the statistical uncertainties. The difference between each method and the nominal value is taken as the systematic uncertainty on the hadron contamination. These results can be

seen summarized in Figure 5.19. One observes an increase in the hadron contamination in the 4.5-5 GeV bin. This is due to the fact that pions start firing the RICH above 4.5 GeV. A reduction in the contamination when progressing to the 5-6 GeV bin is observed, due to the fact that for this p_T region the RICH cut (n0) has been tightened from n0 $>$ 1 to n0 $>$ 3, reducing the hadron contamination at high p_T to just a few percent.

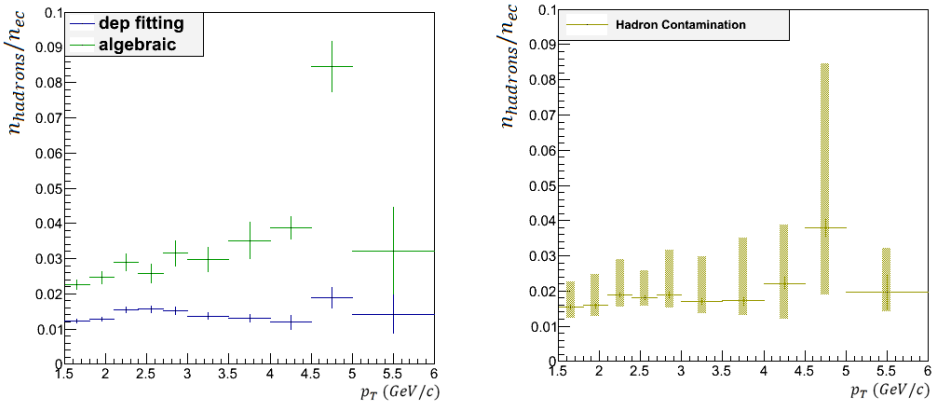

(a) (b)

Figure 5.19: Hadron contamination extracted using two independent methods. The nominal hadron contamination is the weighted average of the two results shown in the left panel.

5.5.2 Electron Background

Nearly all of the background contributions in the electron candidate dca_T distribution are actual electrons resulting from the decay of hadrons or electrons from photon conversion, where the photons originate from hadron decays or produced directly in the collision (referred to as direct photons). These electrons are broken into two classes; photonic and non-photonic electrons. For the purposes of this analysis, photonic electrons are defined to comprise electrons from the Dalitz decay of light pseudoscalar mesons π^0 and η (i.e., $\pi^0 \to e^+ + e^- + \gamma$; $\eta \to e^+ + e^- + \gamma$), and pair production from photons interacting with detector material (i.e., $\gamma \to e^+ + e^-$), henceforth known as conversion electrons. On the other

hand, non-photonic electrons are defined to be those originating from the decays of J/ψ mesons; the three-body decay of kaons (K^+, K^-, and K^0_s) to electrons, known collectively as $Ke3$ electrons; and the semileptonic decay electrons of the D and B meson family. Electrons from the decay of light vector mesons (e.g., ρ, ω, ϕ) are deemed to provide a negligible contribution to the electron dca_T distribution and therefore not included. This is largely due to the small probability of producing high p_T electrons, as used in this analysis, and the relatively small electron producing branching fractions resulting in their contribution to be approximately 10% of J/ψ electrons.

5.5.2.1 Minimizing Photonic Background

Within the PHENIX experiment photonic electrons, largely stemming from conversions in the VTX, are the primary source of electrons. Using the VTX there are many ways to identify and reduce the number of conversion electrons. One of the most effective ways to reject conversions actually comes from the requirement of a hit in layer B0 of the VTX, this results in a significant reduction of conversions as it requires that the photon converts in either the beam pipe or the first layer of the VTX removing conversions from the majority of the VTX material.

The other way the VTX can be used to reduce the photonic background using the VTX is to require electrons to be "isolated". Since conversion and Dalitz decays produce electron pairs from the same origin, the separation distance between the electron-positron pair at the various layers of the VTX is not particularly large. In order to reduce the photonic background, a set of p_T dependent isolation cut windows were developed for each layer of the VTX, these window sizes are shown in Figure 5.20. Any track accompanied by an additional hit within these windows is flagged as not "isolated" and therefore a potential *conversion* and excluded from the electron signal.

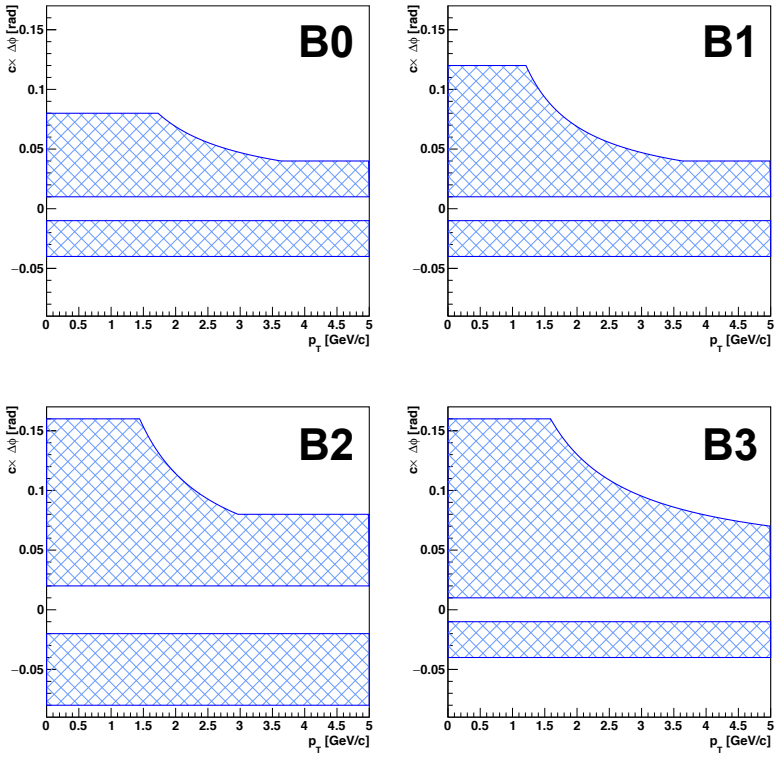

Figure 5.20: The isolation cut window size in $charge \times \Delta\phi$ as a function of p_T for each layer in the VTX. This shape was selected to account for the decreasing opening angles of conversion electrons as the p_T increases.

In order to tune and then judge the effectiveness of the isolation cut to reject photonic electrons single particle simulations generated with PHParticleGen in combination with TPythiaDecayer6 were used. Simulations were generated for π^0, η, and direct γ, run through PISA and PisaToDST using a realistic p_T weighting based on the parent hadron p_T. The details of how these simulations were generated and weighted will be discussed in the subsection on the electron cocktail.

The success of the isolation cut in reducing the photonic background contributions stems from two metrics. First is to minimize the survival rate of the isolation cut for photonic

electrons (ϵ_c) using simulations as seen in Figure 5.21. The survival rate of the isolation cut is defined by equation 5.4:

$$\epsilon = \frac{n_{withIso}}{n} \tag{5.4}$$

Where $n_{withIso}$ is the number of tracks with the isolation cut applied and n is the total number of tracks. The second metric used is maximizing the survival rate of hadrons in data shown (ϵ_{uc}) in Figure 5.22. Hadrons in data provide a measurement of the random association probability, and model how the isolation cut is expected to affect all tracks including heavy flavor electrons.

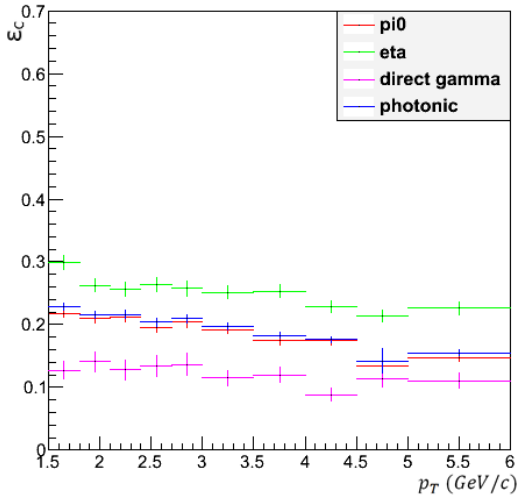

Figure 5.21: The survival rate of photonic electrons of the isolation cut due to correlated effects as determined using simulations

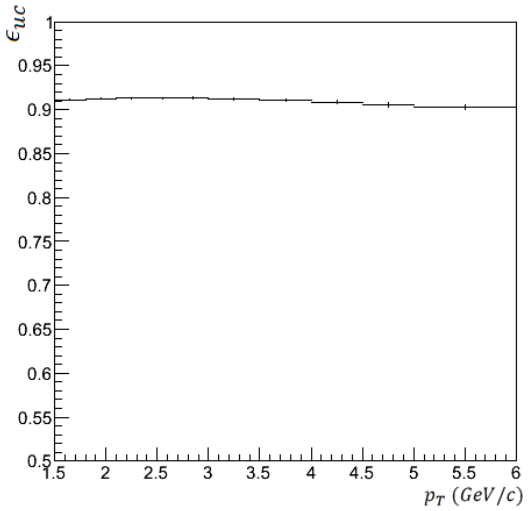

Figure 5.22: The survival rate of the isolation cut of hadrons in data, used to determine the effect of random association on the isolation cut.

The survival rate of photonic electrons, shown in Figure 5.21, was calculated using single particle simulations and does not take into account the affects of random association (similar to what is seen in data hadrons). The actual survival rate of electrons from photonic sources is in fact a combination of the two. For non-photonic electrons, such as those from Ke3, J/ψ or heavy flavor decays, the survival rate is explained by simply uncorrelated effects ϵ_{uc}.

5.5.2.2 Electron Cocktail

In order to properly model and understand the various sources of electrons to the background in the measured dca_T distribution, an electron cocktail was created. This cocktail used full GEANT simulations of single particles from $\pi^0, \eta, J/\psi, K^{\pm}, K^0_s$ and direct photons. The simulations were generated flat in hadron p_T, and for everything but J/ψ flat in rapidity between ± 0.5. J/ψ on the other hand, due to its large mass, was simulated with a Gaussian rapidity distribution of $\sigma = 1.8$ and $|y| < 2$ in order to cover the full central arm acceptance for single electrons from J/ψ. The generated hadrons were then forced

to decay to the relevant decay modes as listen in table 5.2. The resulting electrons were propagated through GEANT detector and digitization simulations (PISA and pisaToDST) with all analysis cuts applied.

Primary Particle	Simulated Decay Modes	Branching Ratios
π^0	$\pi^0 \to \gamma\gamma$	0.988
	$\pi^0 \to \gamma e^+ e^-$	0.012
η	$\eta \to \gamma\gamma$	0.3923
	$\eta \to \pi^0\gamma\gamma$	0.0007
	$\eta \to \gamma e^+ e^-$	0.0049
	$\eta \to \gamma\pi^+\pi^-$	0.0478
	$\eta \to \pi^+\pi^- e^+ e^-$	0.0013
J/ψ	$J/\psi \to e^+ e^-$	0.0602
$K^\pm$	$K^\pm \to e^\pm \nu_e \pi^0$	0.0482
K_s^0	$K_s^0 \to \pi^0\pi^0$	0.3139

Table 5.2: Simulated decay modes for each primary particle species in the electron cocktail. Branching Ratios (B.R.) extracted from PYTHIA decay table

In order to turn these simulations into a properly normalized electron cocktail, the simulated electrons were weighted based on the primary hadron (or direct photon) p_T and normalized based on published differential cross section measurements done by PHENIX Adare et al. (2007) Adare et al. (2011a) Adare et al. (2012) Adare et al. (2011c) Adare et al. (2011d). In order to extrapolate beyond the measured hadron transverse momentum range, the published differential cross-sections were fit using a modified Hagedorn function (eqn. 5.5) for the light mesons and a power law fit (eqn. 5.6) for the J/ψ. A sample fit can be seen in Figure 5.23.

$$\frac{1}{2\pi p_T}\frac{d^2\sigma}{dp_T dy} = \frac{1}{p_T}\frac{p_0}{[\exp(-p_1 p_T - p_2 p_T^2) + p_T/p_3]^{p_4}}. \tag{5.5}$$

For J/ψ a power law fit was used:

$$\frac{1}{2\pi p_T}\frac{d^2\sigma}{dp_T dy} = \frac{1}{2\pi p_T} p_0 \times (1 + \frac{x^2}{p_1^2})^{-p_2}. \tag{5.6}$$

Where the quantities p_0, p_1, p_2, p_3, p_4 are the parameters used in the fit.

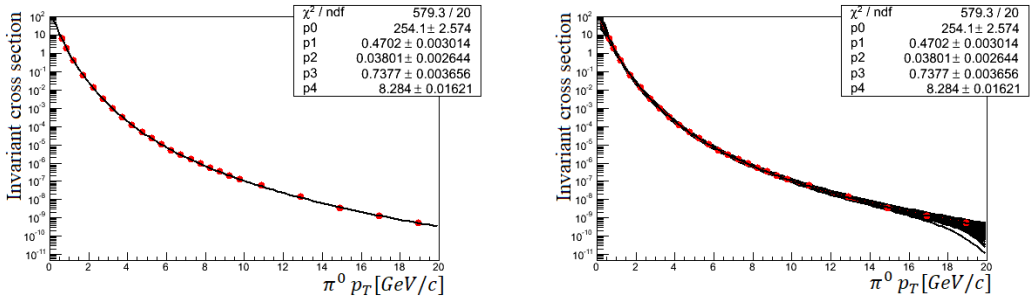

(a) (b)

Figure 5.23: Modified Hagedorn fit to the published pi0 cross section from Adare et al. (2007). Left is the nominal fit, and on the right are 1000 variations used to extract systematic uncertainty

Using the resulting fits to re-weight the electron distributions based on their parent hadron p_T defines an electron cocktail of reconstructed electron tracks with proper relative normalization between each source of electrons 5.24. By varying the individual points based on their statistical and systematic uncertainty and repeating the fitting procedure 1000 times and taking the RMS of the resulting distribution provides us with the systematic uncertainty which is taken into account in the background normalization factors.

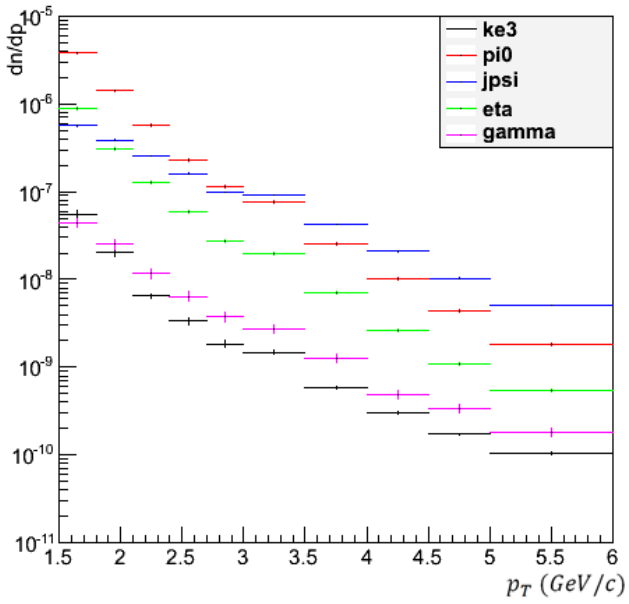

Figure 5.24: Shown is the electron cocktail determined using the hadron weight functions applied to the electron simulations

5.5.2.3 Fraction of Photonic Electrons

In order to provide a constraint to the electron backgrounds, the fraction of photonic electrons (F_p) is calculated. This is done through the calculation of the fraction of non-photonic electrons (F_{np}) from data by exploiting the fact that the isolation cut affects photonic and non-photonic electrons differently, as shown previously. Namely, the sample of non-photonic electrons is reduced by the random association inefficiency (ϵ_{uc}), while photonic electrons are reduced by both the random association inefficiency and the photonic correlated inefficiency ($\epsilon_{uc} \times \epsilon_p$). Thus, one can write the following system of equations for the candidate electron sample with and without the isolation cut:

$$\begin{aligned} n_e &= n_{np} + n_p + n_{hc} \\ \tilde{n}_e &= \tilde{n}_{np} + \tilde{n}_p + \tilde{n}_{hc} \quad = \epsilon_{uc} n_{np} + \epsilon_{uc}\epsilon_p n_p + \tilde{n}_{hc}, \end{aligned} \tag{5.7}$$

where ϵ_{uc} and ϵ_p are the survival rates for non-photonic and photonic electrons, respectively; n_e, n_p, n_{np}, n_{hc} are, respectively, yields of inclusive electron candidates measured in data, photonic electrons, non-photonic electrons, and hadron contamination without requiring the conversion veto cut. The tilde represents electron yields after the isolation cut has been applied. The only unknowns in the system are n_p and n_{np}. Thus, one solves the system and write down F_{np} as:

$$F_{np} = \frac{n_{np}}{n_{np} + n_p}, \tag{5.8}$$

Expressing the F_{np} in terms of measured quantities when the isolation cut is applied equation 5.9 is extracted.

$$F_{np} = \frac{\epsilon_{uc}\epsilon_p n_e - \tilde{n}_e - \epsilon_{uc}\epsilon_p n_{hc} + \tilde{n}_{hc}}{(\epsilon_p - 1)(\tilde{n}_e - \tilde{n}_{hc})}. \tag{5.9}$$

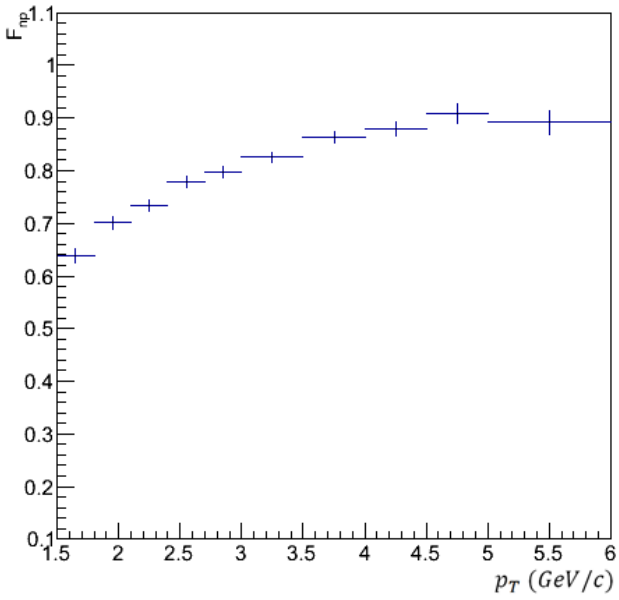

Figure 5.25: F_{np} calculated using the isolation cuts over the analysis region using Equation 5.9

As an alternative way to look at this quantity, the fraction of photonic electrons F_p ($F_p = 1 - F_{np}$) was calculated.

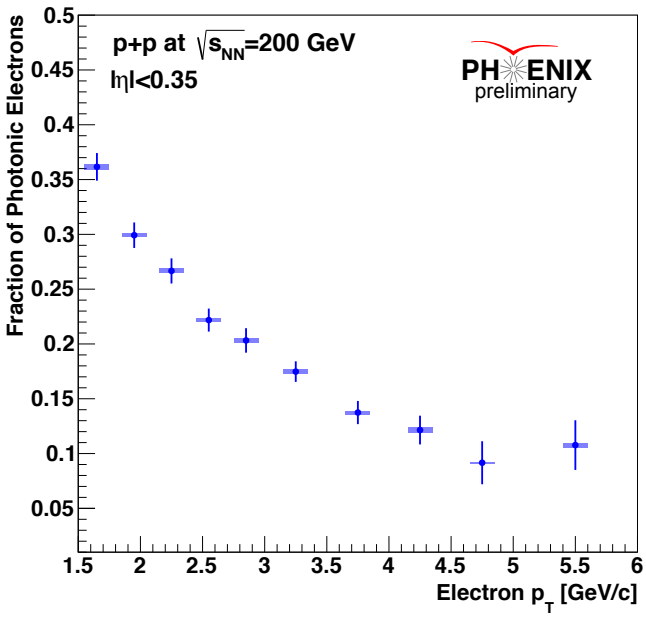

Figure 5.26: F_p calculated using the isolation cuts over the analysis region.

5.5.2.4 Normalizing Electron Background

The electron cocktail provides information on the relative contribution of each type of primary particle to the total sample of background electrons. However, using F_p, as calculated in the previous sections, it is possible to normalize those contributions relative to the *total number of measured electron candidates* in data, effectively determining how many come from each source.

For photonic electrons, it is possible to calculate the fraction of the total number of electron candidates coming from the $i = \pi^0, \eta, \gamma$ source using

$$f_i^{\text{norm}} = (1 - \tilde{f}_{hc})(F_p)\frac{\tilde{n}_i}{\tilde{n}_{\pi^0} + \tilde{n}_\eta + \tilde{n}_\gamma} \tag{5.10}$$

where $\tilde{f}_{hc} = \frac{\tilde{n}_{hc}}{\tilde{n}_e}$ is determined by following the method outlined in the hadron contamination section, shown in Figure 5.19; and n_i is the yield of cocktail electrons from the i^{th} source that pass the conversion veto cut.

We cannot construct a similar formula as above for non-photonic electrons, since heavy flavor electrons are not included in the cocktail. Therefore, they are normalized relative to the simulated π^0 electron yield. For non-photonic sources $i = J/\psi, Ke3$, the fraction of electron candidates relative to the total is given by

$$f_i^{\text{norm}} = f_{\pi^0}^{\text{norm}} \frac{n_i}{n_{\pi_0}}, \tag{5.11}$$

where the ratio n_i/n_{π^0} is shown in Fig. 5.27. The resulting normalization factors for all background sources are shown in Fig. 5.28.

Systematic uncertainties on the background normalization factors were calculated by modifying the hadron weight functions by the uncertainty factors extracted from the fits, as described earlier. The full background normalization calculation was done for 1000 samplings of the hadron weighting, for each sampling calculating a new photonic survival rate to be used in calculating a new F_{np} and normalization factors following equation 5.10. The RMS of the resulting distribution was selected as the systematic uncertainty.

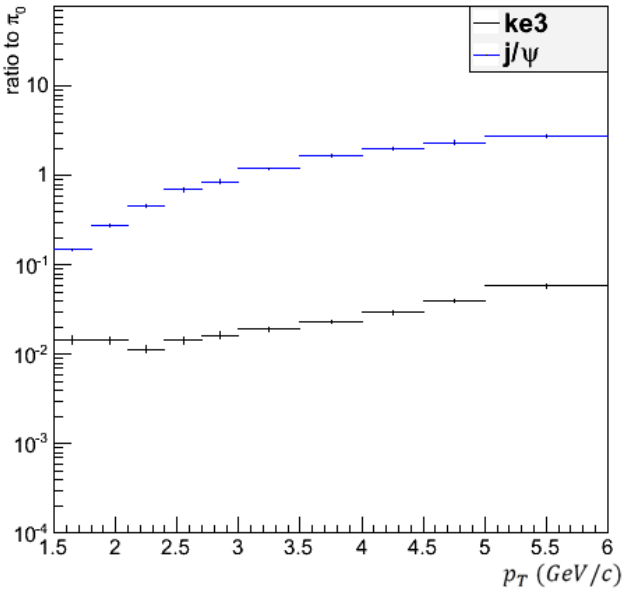

Figure 5.27: The fraction of decay electrons from non-photonic sources to electrons from π^0 decays in the electron cocktail.

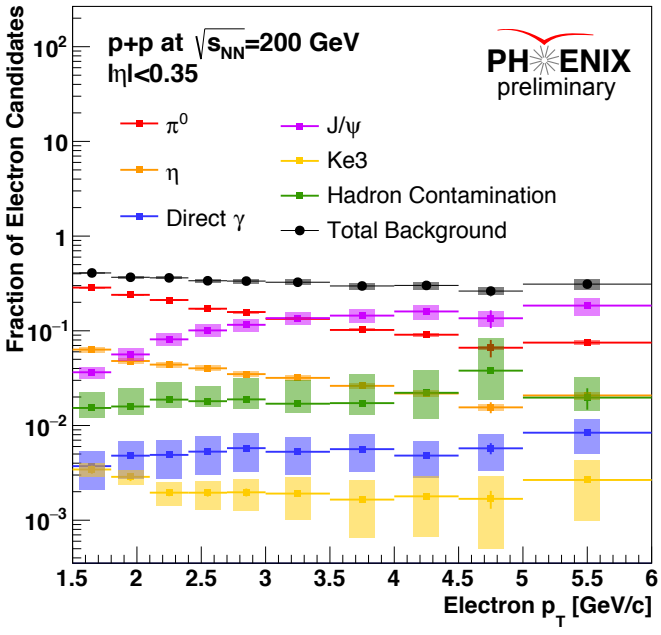

Figure 5.28: Fraction of measured electron candidates attributed to each background source, as calculated using the electron cocktail and F_{np}.

5.5.3 dca_T Templates

To account for the background electrons in the dca_T distributions, one needs to model the dca_T shape for each source of background. For the hadron contamination, this is a particularly simple process, as the hadron tracks can be represented simply with the hadron dca_T shape from data. For electrons on the other hand, the dca_T shape potentially changes due to differences in decay kinematics for each source and therefore has to be determined from simulations. Using the same set of simulations that were generated to produce the electron cocktail, dca_T distributions were extracted for each source. Although the simulations were generated in such a way to mimic the real data and detector response, it is very important to account for any difference in the dca_T resolution between the simulations and data.

Since the dca_T is calculated with respect to the beamcenter the dca_T resolution is directly tied to the beam spot size which varies significantly for each injected store in the accelerator. The simulations were generated using the measured beam spot size from a specific run, 423844. Additionally the simulations are generated with a completely accurate detector alignment, namely the alignment of the VTX ladders used in the reconstruction is the exact same as was used in the PISA simulations. In order to account for small misalignment effects and variations in the beam spot size in data, charged pions in both data and simulations were looked at (identified in data using an $n0 < 0$ cut), and a Gaussian smearing factor was extracted to correct the resolution.

$$\sigma_{smear} = \sqrt{\sigma^2_{data} - \sigma^2_{sims}} \tag{5.12}$$

By comparing the dca_T resolution both before and after this smearing factor has been applied, it was observed that this factor brings the resolution in simulations in line with that of data, as seen in Figure 5.29. This factor is then applied to all of the simulated electron background dca_T distributions, in order to correct for the resolution difference.

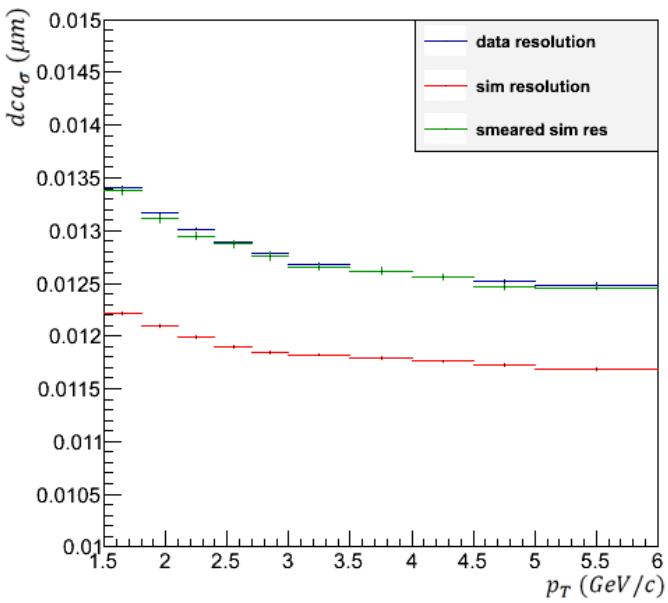

Figure 5.29: dca_T resolution comparison between data hadrons (predominately charged pions), simulated pions and simulated pions with a smearing factor to correct for the resolution difference between data and simulations.

5.5.4 Normalized dca_T Templates

As inputs the unfolding requires measured electron dca_T distributions, as well as absolutely normalized background dca_T distributions. Combining the extracted background normalizations, seen in Figure 5.28, with the dca_T shapes for each background source fully normalized background dca_T distributions were generated. The absolutely normalized distributions can be seen in Figure 5.30, and are one of the major inputs to the unfolding.

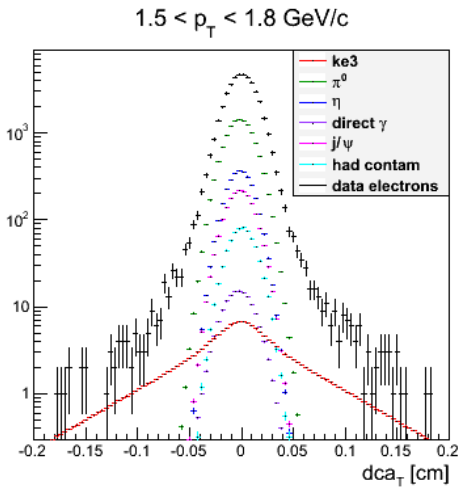
1.5 < p_T < 1.8 GeV/c
ke3
π0
η
direct γ
j/ψ
had contam
data electrons
dca_T [cm]

(a)

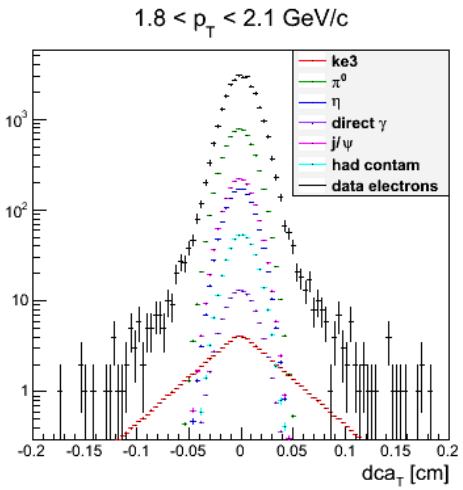
1.8 < p_T < 2.1 GeV/c
ke3
π0
η
direct γ
j/ψ
had contam
data electrons
dca_T [cm]

(b)

(c)

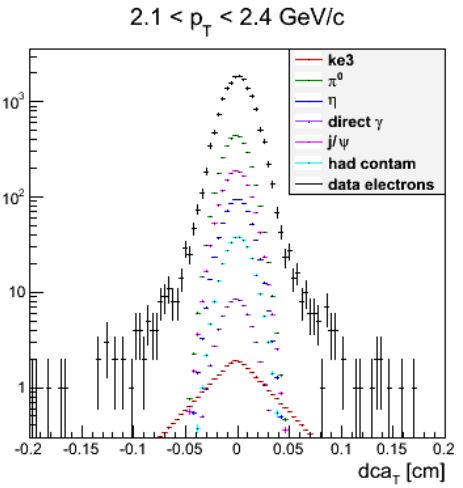
2.1 < p_T < 2.4 GeV/c
ke3
π0
η
direct γ
j/ψ
had contam
data electrons
dca_T [cm]

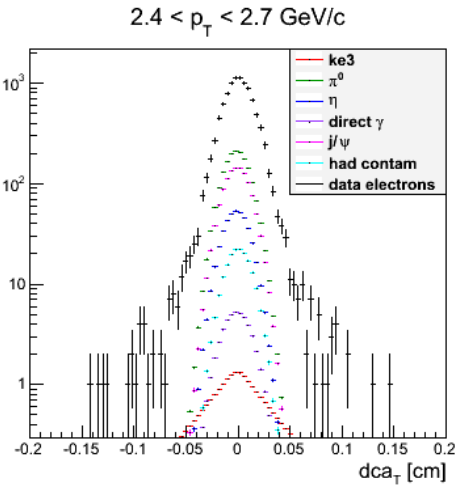
2.4 < p_T < 2.7 GeV/c
ke3
π0
η
direct γ
j/ψ
had contam
data electrons
dca_T [cm]

(d)

(e)

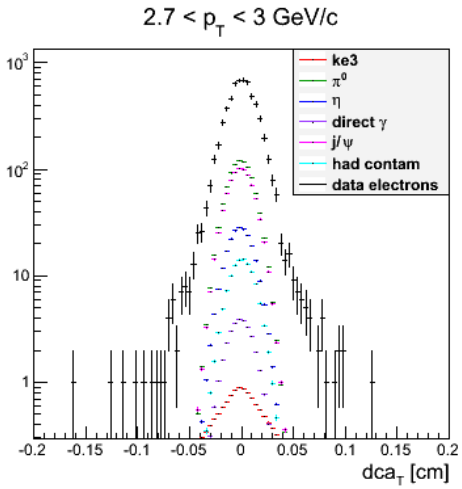
2.7 < p_T < 3 GeV/c
ke3
π0
η
direct γ
j/ψ
had contam
data electrons
dca_T [cm]

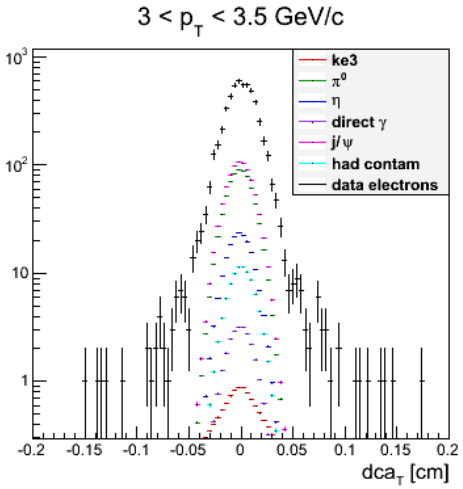
3 < p_T < 3.5 GeV/c
ke3
π0
η
direct γ
j/ψ
had contam
data electrons
dca_T [cm]

(f)

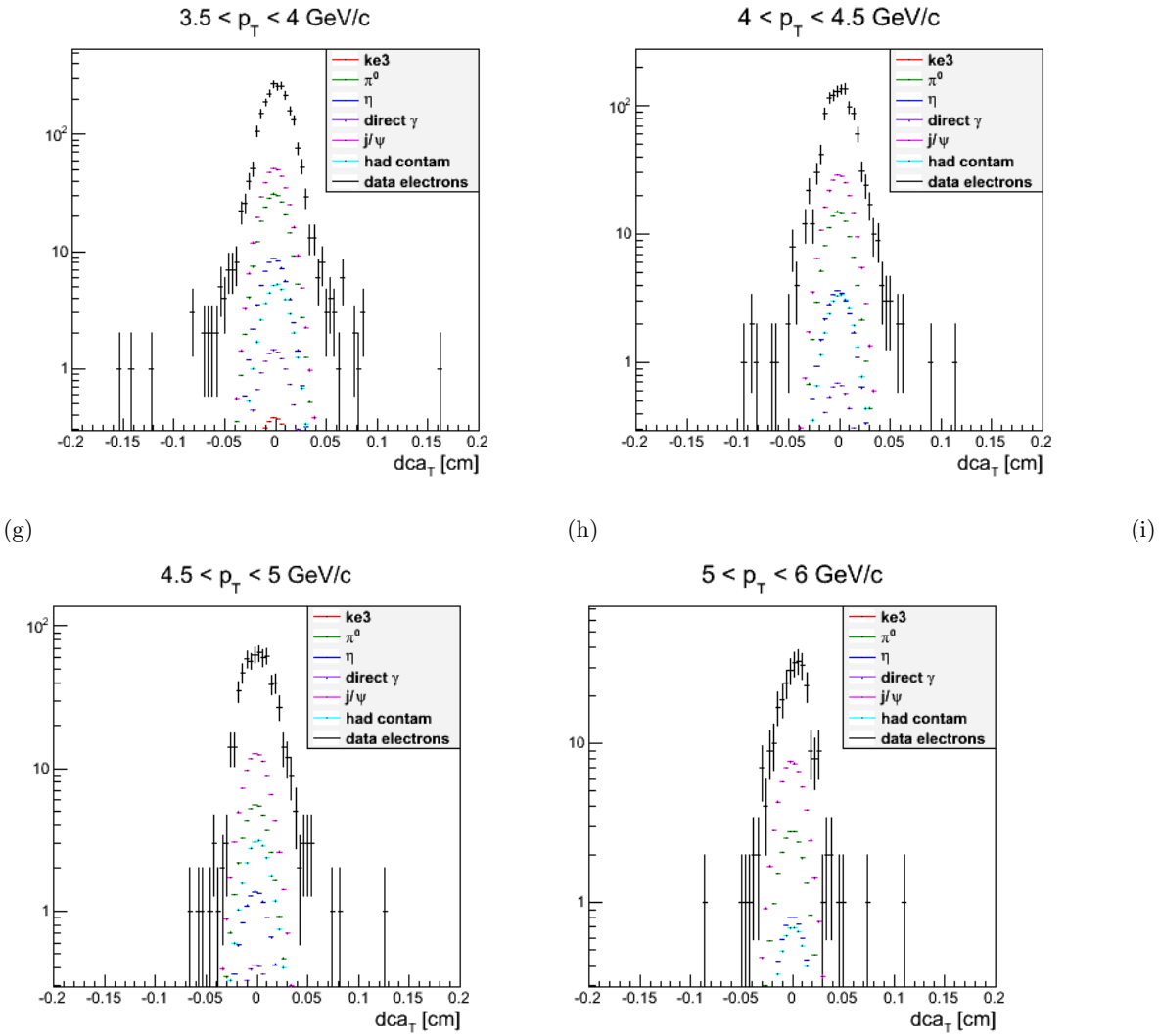

Figure 5.30: dca_T distribution of electron candidates in data (black), as well as normalized templates for each source of background electrons, for each p_T bin.

5.6 Inclusive Heavy Flavor Differential Cross-section

The other main input to the unfolding procedure is the inclusive heavy flavor electron invariant yield. Due to the large run-by-run changes in detector performance as seen in Fig-

ure 5.4 it was decided not to calculate an invariant yield using the 2015 p+p data set. This change in detector performance is a point of issue because in order to measure the invariant yield acceptance and efficiency corrections would need to applied, and these quantities change run-by-run. Given the large correction to be applied, the expected systematic errors on the invariant yields from this dataset would be larger than that of the previously measured yields. Therefore in this analysis previously published inclusive heavy flavor electron invariant yields measured in PHENIX from Adare et al. (2011b) are used.

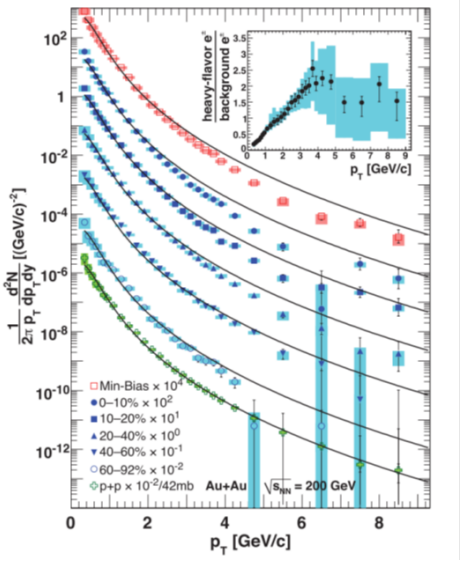

Figure 5.31: Inclusive electron differential cross-section measurement for various centralities of Au+Au (red and blue points) as well as p+p (green) which is used in the unfolding from Adare et al. (2011b).

5.7 Unfolding Measurement

In order to extract parent bottom and charm hadron yields the unfolding procedure is used, as described in section 4.3. As inputs to the unfolding the measured electron dca_T distributions for 10 p_T bins between 1.5 and 6 GeV/c, absolutely normalized dca_T distributions for the background sources, and the previously published inclusive heavy flavor

electron invariant yields described in this chapter are used. Using this information the unfolding is able to extract bottom and charm hadron yields, as well as separated bottom and charm electron yields. This section will describe the tuning of the regularization parameter, the unfolding QA, as well as the extracted unfolding results.

5.7.1 Regularization Parameter

The regularization parameter α is tuned through the maximization of the Log Likelihood. The unfolding procedure was run for α between 0.35 and 2.0 as seen in Figure 5.32, based on this study the nominal value for the regularization was determined to be 1.0, with the upper and lower 1 σ systematic uncertainty to be 0.711 and 1.55 respectively.

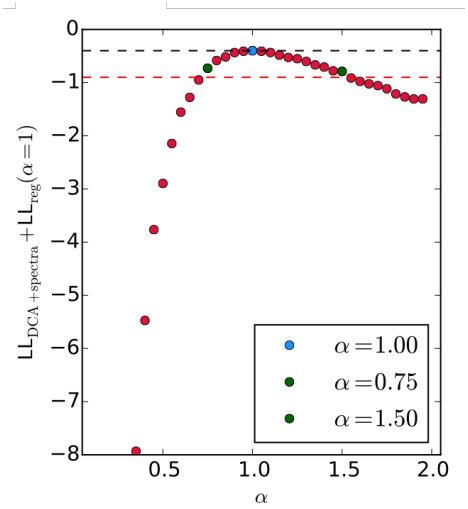

Figure 5.32: Shown is the Log Likelihood as a function of the regularization parameter α, with the red dashed line representing a 1/2 drop in LL.

5.7.2 Evaluating the Unfolding

Before looking at the results of the unfolding procedure there are several important checks to be performed. The first thing that needs to be checked is if the unfolding has converged. The unfolding runs for 3 iterations with each iteration including 1000 not recorded (burn in) and 1000 recorded steps. For each recorded step the Log-Likelihood is calculated,

for the third iteration, after which the unfolding result is extracted, it is expected that no long range trends can be seen in the distribution, as shown in Figure 5.33.

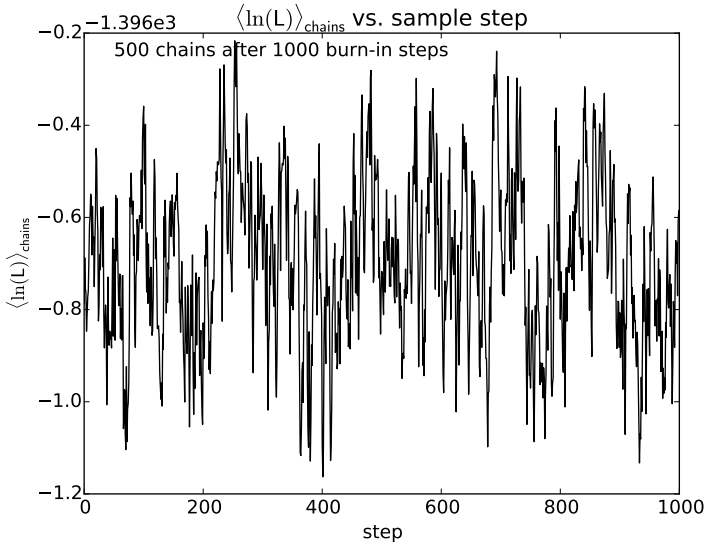

Figure 5.33: Shown is the $Ln(L)$ versus step number in the 3rd iteration of the unfolding. There are no observable long range trends, consistent with the unfolding having converged.

A fundamental check to understand the quality of the unfolding procedure is known as the *refold*, where the decay model is applied to the unfolded solution so it can be directly compared to measured quantities. If the solution is properly converged, one should expect to recover the input distributions, namely the inclusive heavy flavor electron spectra and dca_T distributions. Fig. 5.34 shows, for every p_T bin, the measured electron dca_T (black) and the refolded distribution (red). The unfolded contributions from charm (green) and bottom (blue) electrons, as well as background (brown) are also shown. In every case, a very good description of the measured data within the region over which the log-likelihood fit is carried out is observed, as indicated by the gray shaded area. The refolded electron spectrum, compared to the corresponding input, is shown in Fig. 5.35, where the ratio plot indicates excellent agreement.

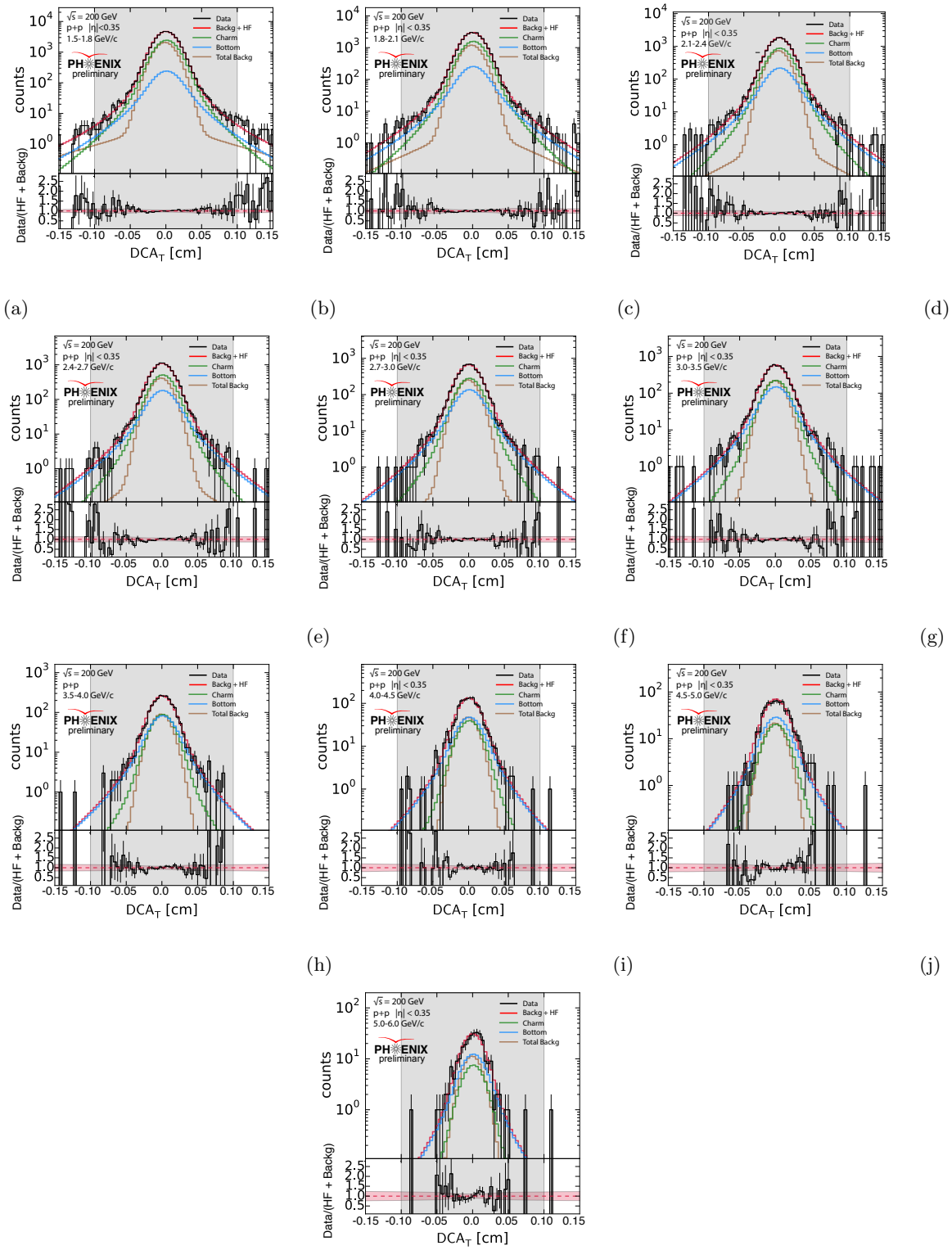

Figure 5.34: Refold of the DCA_T distribution for each p_T bin in which the unfolding uses DCA_T constraints. The various curves on the plots refer to the unfolded $c \rightarrow e$, $b \rightarrow e$, background, refold, and measured electrons.

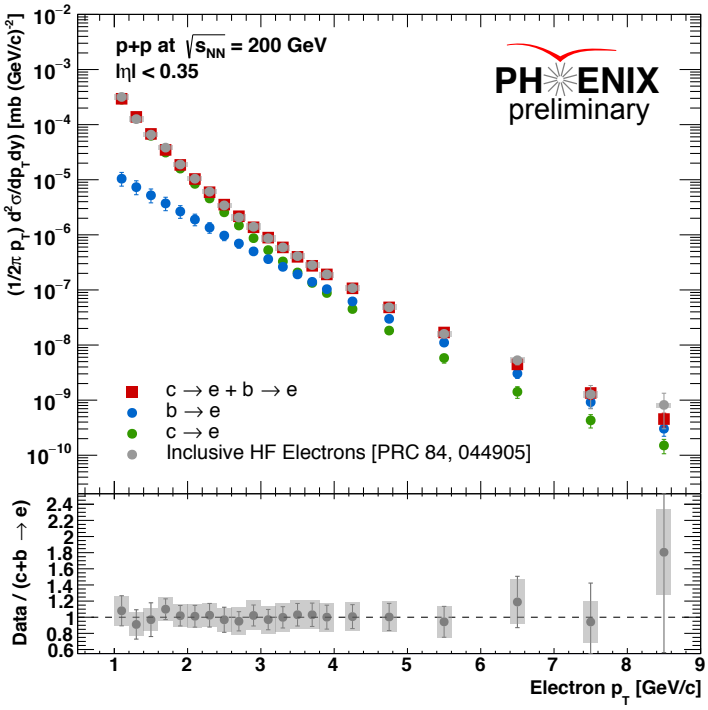

Figure 5.35: Top: Refolded inclusive heavy flavor electron differential cross section compared to the previously published inclusive yield, which is one of the inputs to the unfolding procedure. Also shown are the unfolded contributions from charm and bottom decays separately. Uncertainties are purely statistical. Bottom: Ratio of the previously published inclusive yield to the re-summed unfolding output.

Lastly, the distribution of total log-likelihood associated with the unfolding procedure is examined. As stated earlier in this section, unlike the χ^2 distribution, the LL has no associated probability distribution to assess the goodness of fit. Therefore, such distribution has to be generated with Monte Carlo methods, and is shown in Fig. 5.36. The dashed line indicates the mean of the distribution, and the red line shows the value of total log-likelihood obtained from the unfolding. Excellent agreement is observed, at the level of 0.98σ.

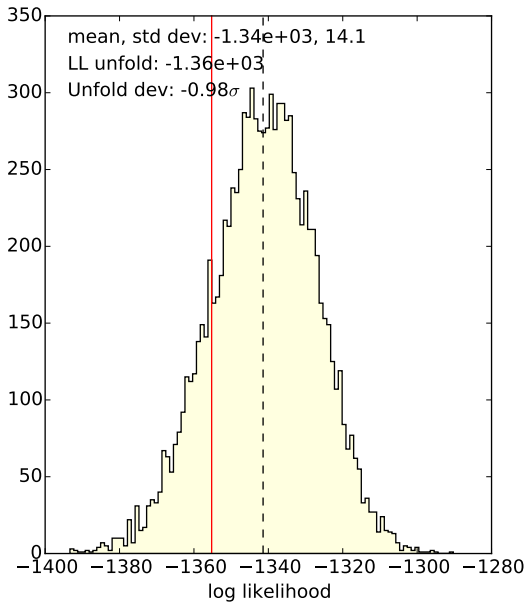

Figure 5.36: The red line represents the total LL of the unfolding result, with the yellow distribution representing a statistical sampling.

5.7.3 Unfolding results

The main unfolding result is the p_T binned hadron yields for the full kinematic range and yield correlations between various hadron p_T bins. This can be rather elegantly visualized in the triangle plot of Figure 5.37. Although it is difficult to directly interpret this figure, there are a few behaviors worth highlighting, the first of which is tight correlation that is seen when comparing neighboring charm and bottom hadron p_T bins, these correlations are seen on the off diagonal panels. Additionally if one looks at the orange panels, one can see the correlation between bottom and charm in the same hadron p_T bin. If one looks carefully at the mid p_T region, there is evidence of anti correlation between the two, I.E. if charm goes up bottom goes down and vice versa.

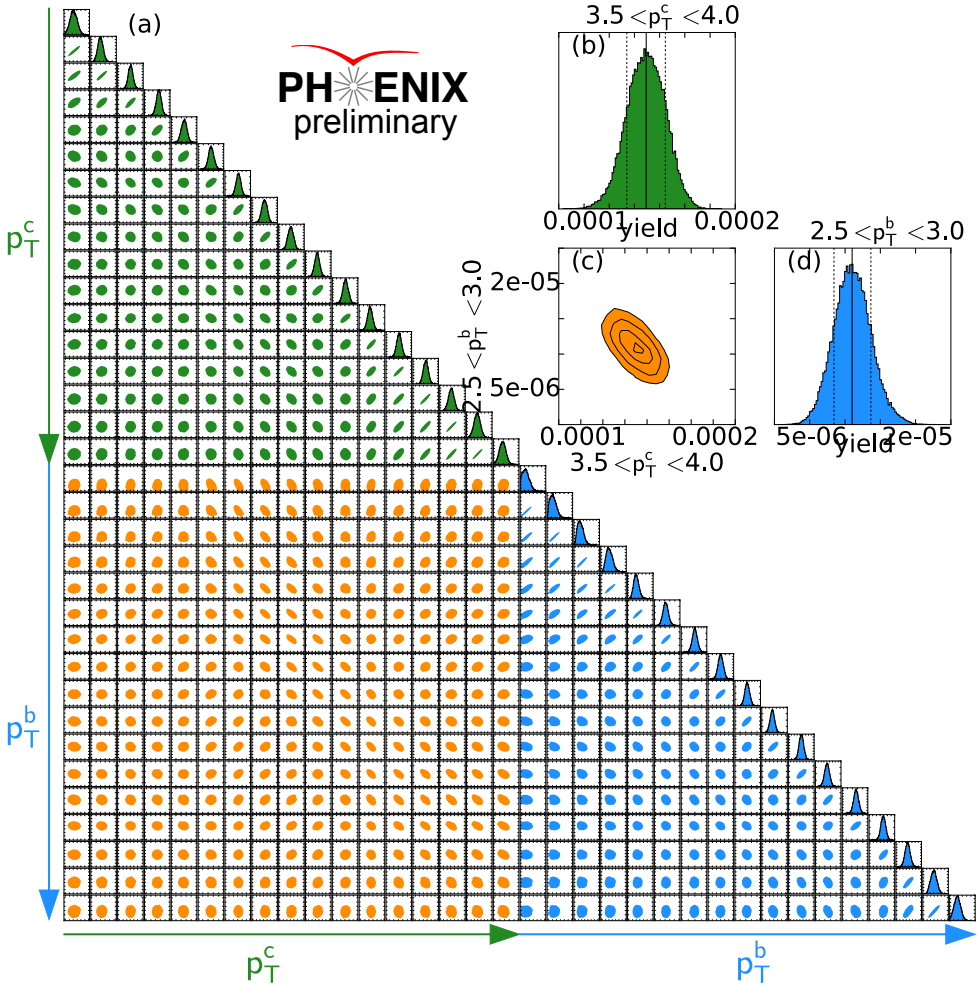

Figure 5.37: Diagonal elements of panel (a) contain information on the bottom and charm hadron yields, a blow up of the yield distributions can be seen in (b) and (d) which includes the 1σ unfold uncertainty. The off diagonal elements contain the correlation information between various hadron p_T bins, a sample distribution can be seen in panel (c)

From this triangle Figure the charm and bottom hadron yields with 1 σ intrinsic unfold uncertainty are extracted, as visualized in panels (b) and (d) in Figure 5.37. Using the extracted charm and bottom hadron yields in each p_T bin the p_T dependent yields were calculated, as seen in Figure 5.38.

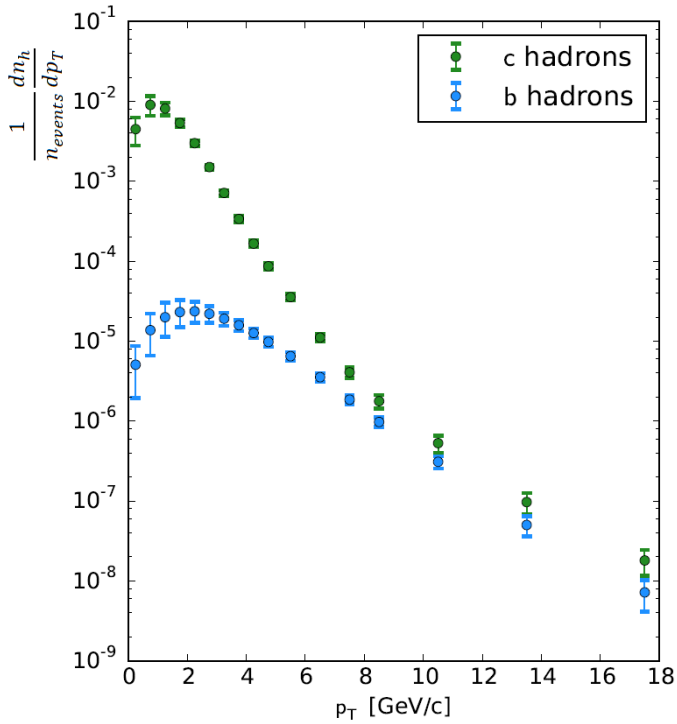

Figure 5.38: Unfolded hadrons yields as a function of transverse momentum for separated bottom and charm hadrons integrated over all rapidity.

Then using this as input to the decay matrix one can extract results for electrons from charm and bottom decays. As has already been shown in Figure 5.35 is is possible to extract the differential cross-section of separated heavy flavor electrons. By comparing the yields of electrons from charm and bottom the b-fraction, defined as the fraction of heavy flavor electrons from bottom decays, was extracted. This can be seen with the intrinsic unfold uncertainty in Figure 5.39, the implications and conclusions from it will be discussed after the addition of systematic uncertainties.

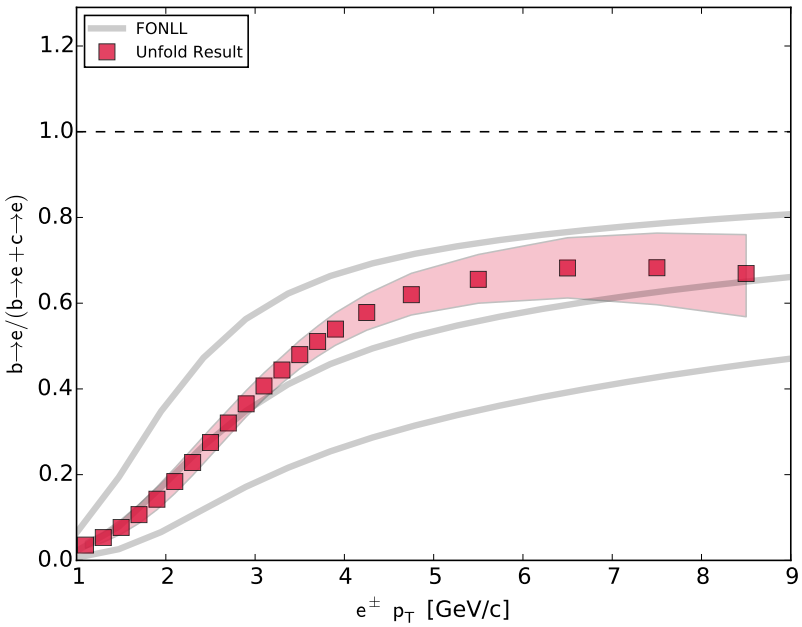

Figure 5.39: Unfolded fraction of electrons from bottom decays to inclusive heavy flavor electrons, as a function of p_T. The uncertainties shown are statistical only from the unfolding procedure. The three gray curves represent the central, upper, and lower FONLL predictions.

5.8 Systematic Uncertainties

In this analysis 5 sources of uncertainty on the unfolding result are considered, all of which are treated as uncorrelated systematic uncertainties. These sources are: the intrinsic unfolding uncertainty, uncertainty due to the inclusive HF yield, uncertainty due to the prior, uncertainty in the background normalization, and uncertainty due to the regularization parameter.

The intrinsic unfold uncertainty is kind of a weird combination between a statistical and systematic uncertainty. Namely it takes into account the statistical uncertainty from the inclusive heavy flavor yield and from the measured electron dca_T distributions through the

unfolding procedure. As these uncertainties are understood through the unfolding procedure they can not be treated as a purely statistical uncertainty and therefore taken as part of the systematic uncertainties.

For the systematic uncertainty due to the inclusive heavy flavor electron invariant yield, the distribution was tilted and kinked based on the systematic uncertainty on the measurement. The largest deviation from the nominal unfolding result as a function of p_T was taken as the systematic uncertainty contribution.

The remaining 2 sources of systematic uncertainty will be discussed in some detail in this section.

5.8.1 Background Normalization Uncertainty

We have previously discussed the sources of systematic uncertainty in the electron cocktail and hadron contamination, and its propagation to the background normalization as shown in Figure 5.28. In order to observe the effect of this uncertainty on the final unfolding result the unfolding was run with every possible combination of $nominal, \pm 1\sigma$ fluctuations. Where the σ was calculated by adding the statistical and systematic uncertainty of each source in quadrature, of the background normalizations. This results in 729 iterations of the unfolding being run to account for every possible combination, the resulting b-fraction distributions can be seen in Figure 5.40. To extract a 1σ uncertainty band due to the background normalization uncertainties the RMS of the distribution of difference to the nominal unfolding result for the 729 variations was taken, as seen in Figure 5.41. Note: for the rest of this section "f" refers to the b-fraction, this is used when describing uncertainties.

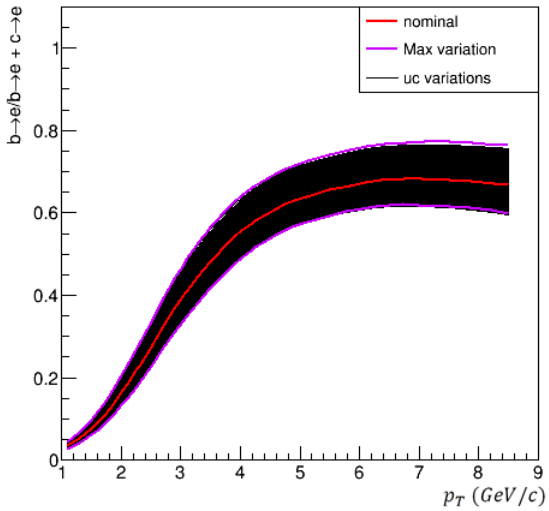

Figure 5.40: Unfolding results for 729 variations of the background normalization factors based on systematic uncertainties.

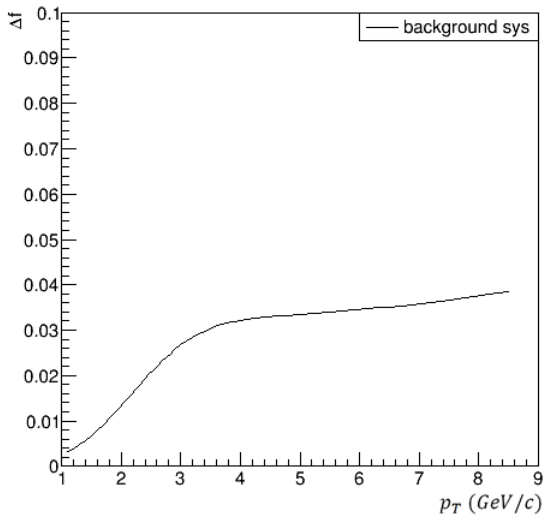

Figure 5.41: The RMS of the difference between the nominal unfold b-fraction result and the variations in the background normalizations. This is taken as the 1σ uncertainty on the b-fraction result due to the background normalizations.

To try to better understand the effect changes in individual components can have on the unfolding result, the b-fraction result was looked at for the situations where all but one source was held nominal and the remaining source was fluctuated high as seen in Figure 5.42. For $p_T > 2$ GeV, the dominant source of this uncertainty comes from the J/ψ, followed by the hadron contamination.

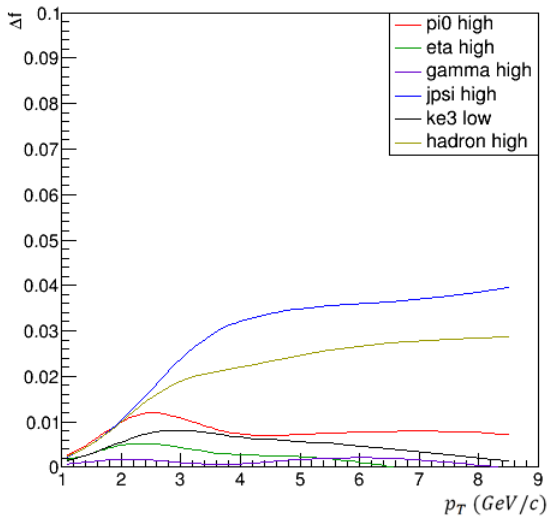

Figure 5.42: Deviation from the nominal unfolding result when individual sources are fluctuated, while preserving all others as nominal.

5.8.2 Systematic Uncertainty From Regularization

Taking the upper and lower uncertainty values from the tuning of the regularization, as seen in Figure 5.32 ($\alpha = 0.711, \alpha = 1.553$) and propagating these forward to the unfolding allows for the extraction of the upper and lower 1σ systematic uncertainties as shown in Figure 5.43.

5.8.2.1 Systematic Uncertainty From Inclusive Heavy Flavor Yield

The 1σ contribution to the systematic uncertainty from the inclusive heavy flavor differential cross-section was calculated by tilting and kinking the published spectra around two

points at 2.8 GeV/c and 5 GeV/c by $\pm 1\sigma$ of the systematic uncertainty around 2 points. This methodology resulted in 8 variations of the inclusive heavy flavor differential cross-section to be used. Of which the largest deviation from the nominal b-fraction was taken to be the 1σ systematic uncertainty.

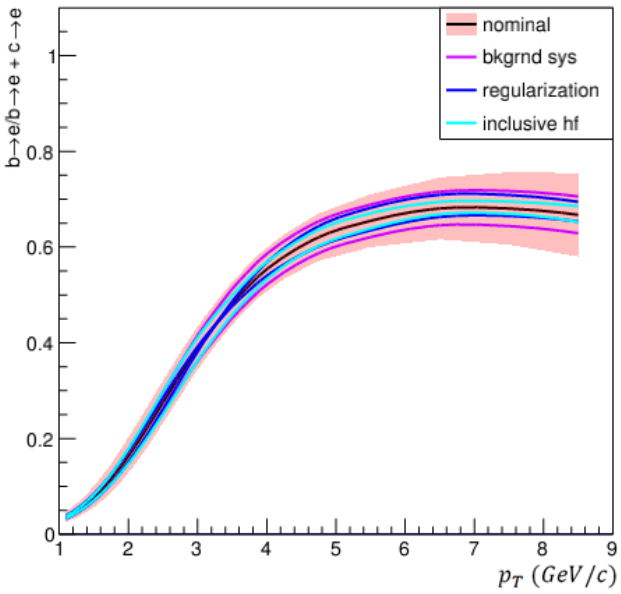

Figure 5.43: Shown are the 1σ systematic uncertainty band to the b-fraction result from background normalization, regularization, as well as the inclusive HF yield.

5.8.3 Total Uncertainty

In this analysis each source of uncertainty is taken to be independent. This means they can simply be combined in quadrature without needing to account for correlations between the various sources. The numerical contribution for each background source can be seen in Figure 5.44, and the uncertainty as a fraction of the b-fraction result can be seen in Figure 5.45. In this result the dominant contribution to the uncertainty is the intrinsic unfold uncertainty which at low p_T is about a 30% contribution, dropping to a 10% effect at high p_T. All other sources of uncertainty contribute between $0 - 10\%$ of the b-fraction

value depending on the p_T. Combining all sources of uncertainty in quadrature a low p_T uncertainty of 35% and a high p_T of $10 - 15\%$ is observed.

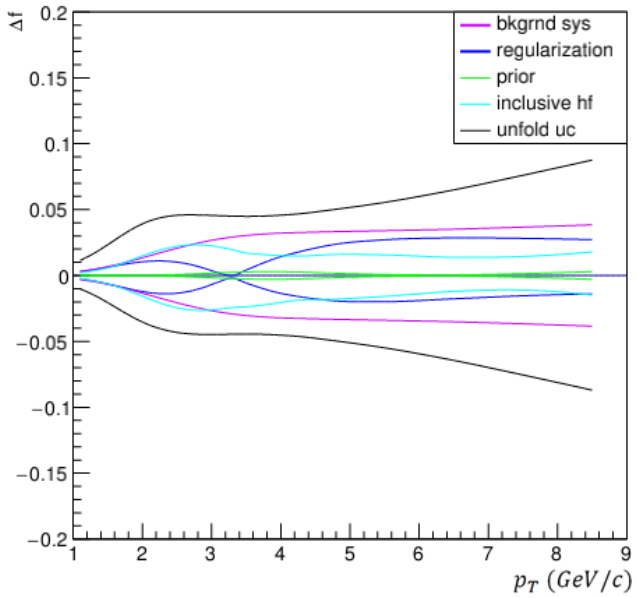

Figure 5.44: Shown are the numerical 1σ uncertainties due to each source of considered backgrounds.

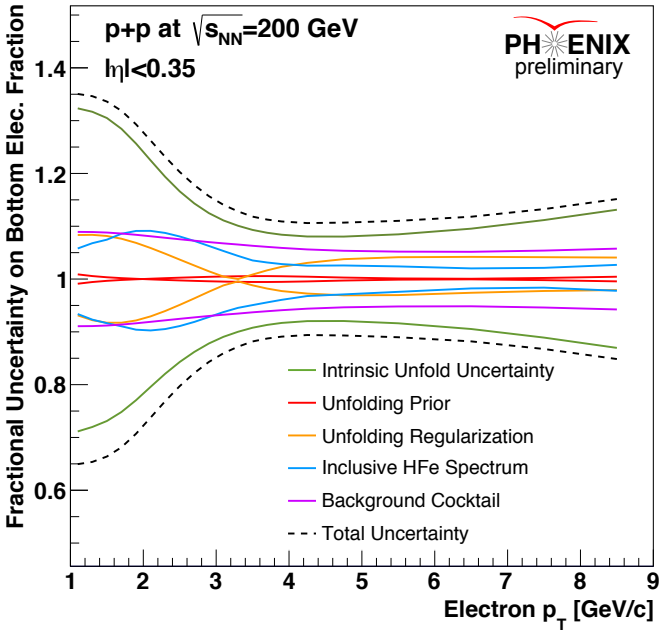

Figure 5.45: Shown are the fractional 1 σ uncertainty contributions to the b-fraction for each source.

CHAPTER 6. RESULTS AND DISCUSSION

6.1 Hadron Yields

The direct result of the unfolding procedure are hadron yields as a function of p_T. Using these measurements and correcting for the known p+p cross-section of 42 mb we are able to make a hadron differential cross section measurement integrated over rapidity as shown in Figure 6.1 with the full uncertainty band. Charm hadrons dominate the low p_T production, while above 10 GeV/c, the contributions of charm and bottom are comparable when accounting for the uncertainties. It is important to note that this result is model dependent, as it relies on PYTHIA's modeling of the rapidity distribution hadron production as well as PYTHIA modeling of the decay kinematics.

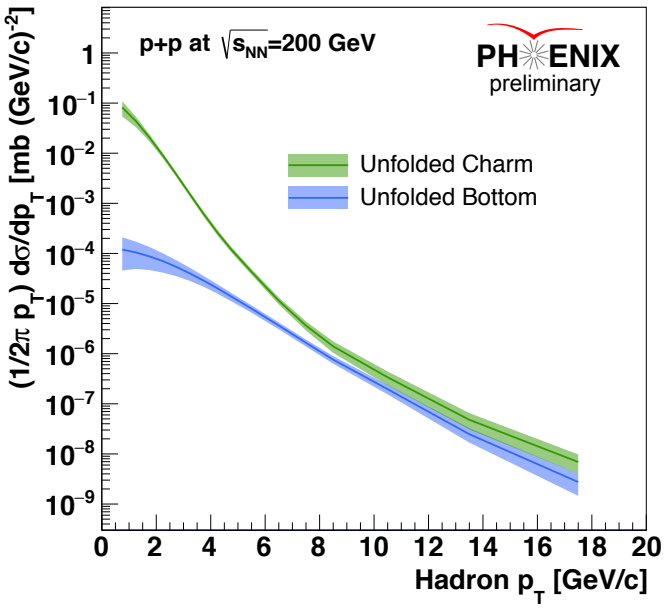

Figure 6.1: Shown are the rapidity integrated hadron differential cross-sections for p_T between 1 and 20 GeV/c

By using a PYTHIA description of the hadron production kinematics it was possible to extract a D^0 differential cross-section measurement at mid rapidity from the unfolding result. This is done by scaling the charm differential cross-section result by the fraction of charm hadrons which are D^0 with $|\eta| < 1$ as calculated by PYTHIA. This allows for a comparison to the measured D^0 differential cross-section done by STAR, as seen in Figure 6.2. A modified Hagedorn function fit was applied to the unfolded PHENIX measurement and the ratio of both the STAR and unfolded points were taken to the fit. The ratio plot allows for an accurate comparison between the STAR and PHENIX points even though they have different transverse momentum bins. It is very clear through this comparison, seen in panel b, that the STAR measurement is in good agreement with the unfolded D^0 differential cross-section across the full momentum range.

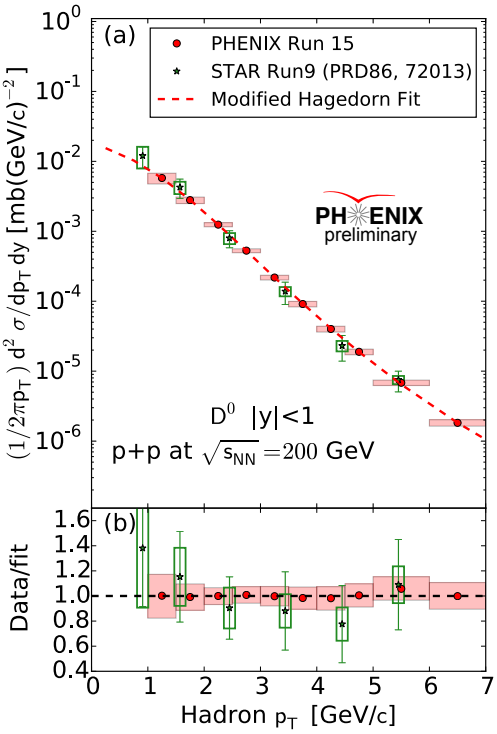

Figure 6.2: Shown is a comparison of the unfolded D^0 differential cross-section to that measured by the STAR experiment at mid rapidity. The ratio of a fit to the unfolded results is seen in panel b.

6.2 b-fraction

The hadron yields can be used as inputs to the decay matrix in order to study quantities for electrons from bottom and charm decays. The electron spectra have the advantage of significantly reducing the model dependency of the result. As it will no longer be dependent on the PYTHIA model for the rapidity distribution of heavy flavor hadrons, as well as decreases the dependency on the PYTHIA modeling of the decay kinematics. This has been shown earlier in the electron yield results seen in Figure 5.35, however can also be

used to look at the fraction of heavy flavor electrons which come from b decays (called b-fraction).

The b-fraction result for the 2015 p+p data set, with full uncertainty bands can be seen in Figure 6.3. As one would expect given the hadron cross-section and mass difference between bottom and charm hadrons, electrons from charm decays dominate the low p_T regime. While at high p_T, above 4 GeV/c electrons from bottom contribute to approximately 60% of the heavy flavor electron sample. This measurement is a significant improvement in terms of reduction of uncertainties and is in very good agreement when compared to the previous PHENIX measurement Adare et al. (2009) which was done using electron-hadron correlations. It is also possible to compare the results with measurements done by STAR through both electron hadron and electron D^0 correlations. The b-fraction results from STAR are systematically below the unfolding result for p+p, however when taking into account the statistical and systematic uncertainties on the STAR measurements the two results are consistent.

There are theoretical calculations made with perturbative QCD for the b-fraction using Fixed Order Next to Leading Log (FONLL). At low p_T the central FONLL prediction is in very good agreement with this measurement, while at high p_T the result is in-between the central and upper prediction. This makes the argument that perturbative QCD does a good job at predicting the relative production of charm and bottom electrons.

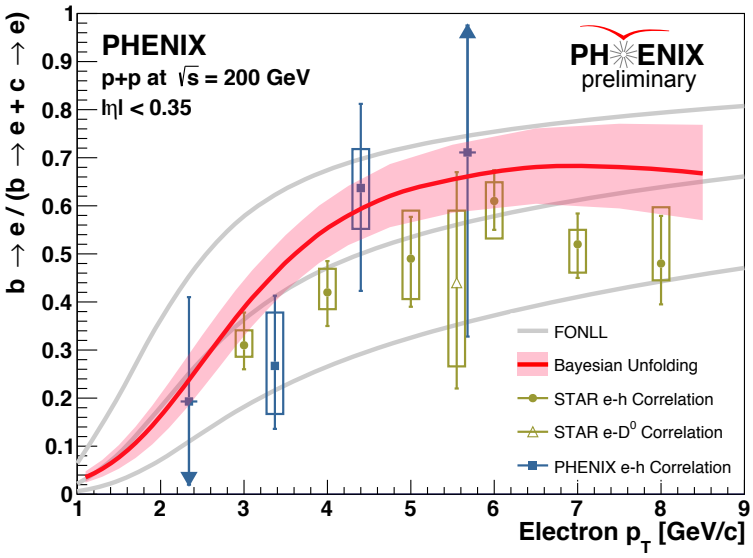

Figure 6.3: Shown is an overlay of the unfolded b-fraction result with previously published PHENIX and STAR measurements, as well as PQCD predictions from FONLL.

Early on in my graduate student career I got involved with the effort to measure separated bottom and charm electrons in the 2011 Au+Au data set. My contribution to that measurement was the understanding the effects from the underlying event. Due to my contributions to the analysis I was included in the Paper Preparation Committee. The measured separated heavy flavor electron yields in Au+Au were combined with the STAR electron-hadron correlation measurements, since at the time PHENIX did not have a p+p measurement, and measured the nuclear modification factor for minimum bias Au+Au collisions Adare et al. (2016).

This measurement has the potential to provide insight into the energy loss experienced by heavy flavor quarks. In particular provide insight into the mass dependence of the energy loss due to interactions in the QGP. It was observed in this measurement that for minimum bias Au+Au at $\sqrt{s_{NN}} = 200GeV$ electrons from bottom decays observe less suppression than those from charm decays at 3 GeV/c, as seen in Figure 6.4. However, the significance

of this difference is low given the large uncertainties in the measurements. Above 3 GeV/c in p_T there is no discernible difference in the suppression of electrons from bottom and charm. The point at 3 GeV/c provides indication that there could be a mass dependence to the energy loss, however until a new measurement of the R_{AA} can be done with improved uncertainties in both the Au+Au and p+p baseline more cannot be said at this point.

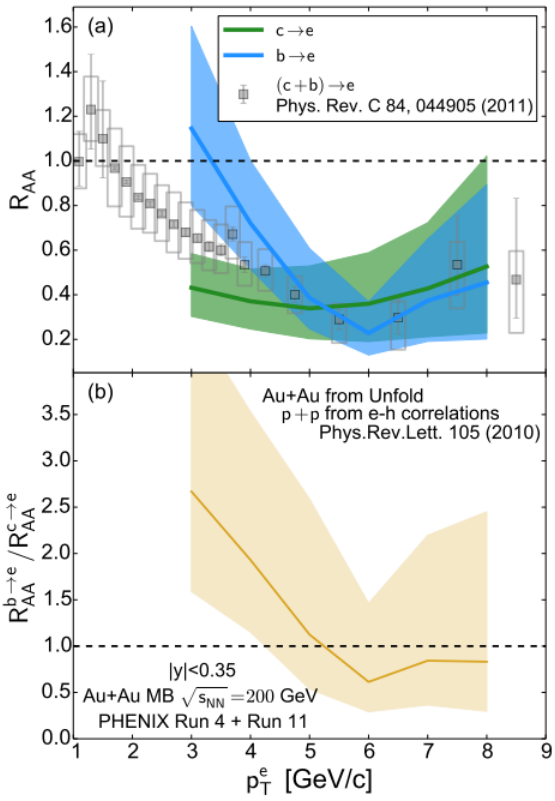

Figure 6.4: Shown is the R_{AA} calculated using the 2011 Au+Au in combination with a p+p baseline measurement from STAR, using electron-hadron correlations. Adare et al. (2016)

6.3 Conclusions and Outlook

This dissertation has presented results for the measurement of charm and bottom quark production in p+p collisions at $\sqrt{s_{NN}} = 200\,GeV$. Additionally it has shown measurements of the differential cross-section of both charm and bottom hadrons as well as electrons from charm and bottom decays. The D^0 differential cross-section measurement at mid-rapidity has been shown to be consistent with previous measurements made by the STAR collaboration. The measured b-fraction results were consistent with previous measurements by both PHENIX and STAR while having reduced uncertainties and covering a larger momentum range. Additionally PQCD predictions done using FONLL are in good agreement with this measurement, implying that perturbative QCD provides good explanation of the relative production of bottom and charm electrons.

This dissertation also provided looks at the first separated bottom and charm R_{AA} measurement from PHENIX at mid rapidity. This measurement has large uncertainties and a limited p_T reach, however it suggests that electrons from charm observe more suppression at p_T of 3 GeV/c. With the new p+p differential cross-sections shown in this dissertation it will be possible to update the R_{AA} measurement to have further reach in p_T as well as reduced uncertainties at mid p_T. This will allow for insight to be gained on the mass dependence of energy loss due to the QGP. There is a parallel effort by other collaborators in PHENIX to analyze a significantly larger Au+Au data set which will be combined with the p+p results shown here to present a much improved R_{AA} measurement in a future publication.

REFERENCES

Cern accelerating science document server. http://cds.cern.ch/.

Adare, A. et al. (2007). Inclusive cross section and double helicity asymmetry for π^0 production in $p+p$ collisions at $\sqrt{s} = 200$ GeV: Implications for the polarized gluon distribution in the proton. *Phys. Rev. D*, 76:051106.

Adare, A. et al. (2009). Measurement of Bottom versus Charm as a Function of Transverse Momentum with Electron-Hadron Correlations in p^+p Collisions at $\sqrt{s} = 200$ GeV. *Phys. Rev. Lett.*, 103:082002.

Adare, A. et al. (2011a). Cross section and double helicity asymmetry for η mesons and their comparison to π^0 production in $p + p$ collisions at $\sqrt{s} = 200$ GeV. *Phys. Rev. D*, 83:032001.

Adare, A. et al. (2011b). Heavy-quark production in p + p and energy loss and flow of heavy quarks in au + au collisions at $\sqrt{s_{NN}} = 200$ gev. *Phys. Rev. C*, 84:044905.

Adare, A. et al. (2011c). Identified charged hadron production in $p+p$ collisions at $\sqrt{s} = 200$ and 62.4 gev. *Phys. Rev. C*, 83:064903.

Adare, A. et al. (2011d). Measurement of neutral mesons in $p+p$ collisions at $\sqrt{s} = 200$ GeV and scaling properties of hadron production. *Phys. Rev. D*, 83:052004.

Adare, A. et al. (2012). Ground and excited state charmonium production in $p+p$ collisions at $\sqrt{s} = 200$ GeV. *Phys. Rev. D*, 85:092004.

Adare, A. et al. (2016). Single electron yields from semileptonic charm and bottom hadron decays in Au + Au collisions at $\sqrt{s_{NN}} = 200$ gev. *Phys. Rev. C*, 93:034904.

Adare, A. M., McCumber, M. P., Nagle, J. L., and Romatschke, P. (2014). Examination whether heavy quarks carry information on the early-time coupling of the quark-gluon plasma. *Phys. Rev.*, C90(2):024911.

Adcox, K. et al. (2003a). PHENIX central arm tracking detectors. *Nucl. Instrum. Meth.*, A499:489–507.

Adcox, K. et al. (2003b). PHENIX detector overview. *Nucl. Instrum. Meth.*, A499:469–479.

Aizawa, M. et al. (2003). PHENIX central arm particle ID detectors. *Nucl. Instrum. Meth.*, A499:508–520.

Allen, M. et al. (2003). PHENIX inner detectors. *Nucl. Instrum. Meth.*, A499:549–559.

Aphecetche, L. et al. (2003). PHENIX calorimeter. *Nucl. Instrum. Meth.*, A499:521–536.

Arnold, P., Lenaghan, J., Moore, G. D., and Yaffe, L. G. (2005). Apparent thermalization due to plasma instabilities in the quark-gluon plasma. *Phys. Rev. Lett.*, 94:072302.

Baier, R., Mueller, A., Schiff, D., and Son, D. (2001). Bottom-up thermalization in heavy ion collisions. *Physics Letters B*, 502(1):51 – 58.

Bazavov, A. et al. (2014). Equation of state in $(2 + 1)$-flavor qcd. *Phys. Rev. D*, 90:094503.

Brun, R., Bruyant, F., Maire, M., McPherson, A. C., and Zanarini, P. (1987). GEANT3.

Cacciari, M., Greco, M., and Nason, P. (1998). The P(T) spectrum in heavy flavor hadroproduction. *JHEP*, 05:007.

Choudalakis, G. (2012). Fully Bayesian Unfolding. https://arxiv.org/abs/1201.4612.

Fries, R. J., Muller, B., Nonaka, C., and Bass, S. A. (2003). Hadron production in heavy ion collisions: Fragmentation and recombination from a dense parton phase. *Phys. Rev.*, C68:044902.

Fritzsch, H., Gell-Mann, M., and Leutwyler, H. (1973). Advantages of the Color Octet Gluon Picture. *Phys. Lett.*, 47B:365–368.

Gell-Mann, M. (1964). A Schematic Model of Baryons and Mesons. *Phys. Lett.*, 8:214–215.

Goodman, J. and Weare, J. (2010). Ensemble samplers with affine invariance. *Communications in Applied Mathematics and Computational Science, Vol. 5, No. 1, p. 65-80, 2010*, 5:65–80.

Griffiths, D. (2008). *Introduction to Elementary Particles*. Physics textbook. Wiley.

Harrison, M., Ludlam, T., and Ozaki, S. (2003). RHIC project overview. *Nucl. Instrum. Meth.*, A499:235–244.

Karsch, F. (2002). *Lattice QCD at High Temperature and Density*, pages 209–249. Springer Berlin Heidelberg, Berlin, Heidelberg.

Kurosawa, M. (2013). Higher harmonics flow measurement of charged hadrons and electrons in wide kinematic range with PHENIX VTX tracker. *Nucl.Phys.*, A904-905:397c–400c.

Miller, M. L., Reygers, K., Sanders, S. J., and Steinberg, P. (2007). Glauber modeling in high-energy nuclear collisions. *Annual Review of Nuclear and Particle Science*, 57(1):205–243.

Nason, P., Dawson, S., and Ellis, R. K. (1989). The One Particle Inclusive Differential Cross-Section for Heavy Quark Production in Hadronic Collisions. *Nucl. Phys.*, B327:49–92. [Erratum: Nucl. Phys.B335,260(1990)].

Nouicer, R. (2013). Probing Hot and Dense Matter with Charm and Bottom Measurements with PHENIX VTX Tracker. *Nucl.Phys.*, A904-905:647c–652c.

Nouicer, R. et al. (2009). Status and Performance of New Silicon Stripixel Detector for the PHENIX Experiment at RHIC: Beta Source, Cosmic-rays and Proton Beam at 120 GeV. *Journal of Instrumentation*, 4:P04011. and references therein.

Patrignani, C. et al. (2016). Review of Particle Physics. *Chin. Phys.*, C40(10):100001.

Shuryak, E. V. (1978). Quark-Gluon Plasma and Hadronic Production of Leptons, Photons and Psions. *Phys. Lett.*, 78B:150. [Yad. Fiz.28,796(1978)].

Sjostrand, T., Mrenna, S., and Skands, P. Z. (2006). PYTHIA 6.4 Physics and Manual. *JHEP*, 05:026.

Wilson, K. G. (1974). Confinement of quarks. *Phys. Rev. D*, 10:2445–2459.